WESTERN SYDNEY
UNIVERSITY

Computer Vision in Target Pursuit Using a UAV

Feng (Teddy) Su

A thesis submitted in partial fulfilment of requirements
for the degree of
Doctor of Philosophy

Supervisors
A/Prof. Gu Fang
Dr. Ju Jia (Jeffrey) Zou

School of Computing, Engineering and Mathematics
Western Sydney University
July 2018

Statement of Authentication

I hereby declare that this submission is my own work and that this report contains no material that has been accepted for the award of any other degree or diploma, and to the best of my knowledge and belief, this report contains no material previously published or written by another person, except where due reference is made in the text of the report.

Signed

07/01/19

Date

Abstract

Research in target pursuit using Unmanned Aerial Vehicle (UAV) has gained attention in recent years, this is primarily due to decrease in cost and increase in demand of small UAVs in many sectors. In computer vision, target pursuit is a complex problem as it involves the solving of many sub-problems which are typically concerned with the detection, tracking and following of the object of interest. At present, the majority of related existing methods are developed using computer simulation with the assumption of ideal environmental factors, while the remaining few practical methods are mainly developed to track and follow simple objects that contain monochromatic colours with very little texture variances. Current research in this topic is lacking of practical vision based approaches. Thus the aim of this research is to fill the gap by developing a real-time algorithm capable of following a person continuously given only a photo input.

As this research considers the whole procedure as an autonomous system, therefore the drone is activated automatically upon receiving a photo of a person through Wi-Fi. This means that the whole system can be triggered by simply emailing a single photo from any device anywhere. This is done by first implementing image fetching to automatically connect to WIFI, download the image and decode it. Then, human detection is performed to extract the template from the upper body of the person, the intended target is acquired using both human detection and template matching. Finally, target pursuit is achieved by tracking the template continuously while sending the motion commands to the drone.

In the target pursuit system, the detection is mainly accomplished using a proposed human detection method that is capable of detecting, extracting and segmenting the human body figure robustly from the background without prior training. This involves detecting face, head and shoulder separately, mainly using gradient maps. While the tracking is mainly accomplished using a proposed generic and non-learning template matching method, this involves combining intensity template matching with colour histogram model and employing a three-tier system for template management. A flight controller is also developed, it supports three types of

controls: keyboard, mouse and text messages. Furthermore, the drone is programmed with three different modes: standby, sentry and search.

To improve the detection and tracking of colour objects, this research has also proposed several colour related methods. One of them is a colour model for colour detection which consists of three colour components: hue, purity and brightness. Hue represents the colour angle, purity represents the colourfulness and brightness represents intensity. It can be represented in three different geometric shapes: sphere, hemisphere and cylinder, each of these shapes also contains two variations.

Experimental results have shown that the target pursuit algorithm is capable of identifying and following the target person robustly given only a photo input. This can be evidenced by the live tracking and mapping of the intended targets with different clothing in both indoor and outdoor environments. Additionally, the various methods developed in this research could enhance the performance of practical vision based applications especially in detecting and tracking of objects.

Acknowledgements

I would like to express my gratitude to my supervisor panel: principal supervisor A/Prof. Gu Fang and co-supervisor Dr. Ju Jia (Jeffrey) Zou for their support, especially Gu for his constant encouragement and guidance throughout the research which enabled me to develop a better understanding of the subjects involved.

I am also grateful and honoured to the scholarship committee for providing financial support by selecting me for the Australian Postgraduate Award and WSU Top-Up Award, the latter is only offered to the highest ranked applicant.

I would like to thank the Western Sydney University especially the School of Computing, Engineering and Mathematics for providing me the opportunity and resources to undergo research and conduct experiments in this field.

Finally, I would like to thank my parents for their encouragement and patience throughout the journey of my study.

Table of Contents

List of Figures

List of Tables

List of Abbreviations

2D Two-Dimensional

3D Three-Dimensional

AMT Adaptive Multi-channel Thresholding

ANN Artificial Neural Network

AT Attention

CCD Charge Coupled Device

CCE Chroma based Colour Enhancement

CMOS Complementary Metal Oxide Semiconductor

CNN Convolutional Neural Network

CPU Central Processing Unit

FRG Fragment based Tracking

GHD Gradient based Human Detection

GMM Gaussian Mixture Model

GPS Global Positioning System

GPU Graphics Processing Unit

HCL Hue-Chroma-Lightness

HCV Hue-Chroma-Value

HOG Histogram of Oriented Gradients

HPB Hue-Purity-Brightness

HSL Hue-Saturation-Lightness

HSV Hue-Saturation-Value

IGMM Improved Gaussian Mixture Model

INS Inertial Navigation System

KNL Kernel based Tracking

LGN Lateral Geniculate Nucleus

LOG Laplacian of Gaussian

LSH Locality Sensitive Histogram based Tracking

LSK Local Sparse Appearance Model and K-selection based Tracking

NBP Normalised Back Projection

NCC Normalised Cross Correlation

NETSH Network Shell

OAB Online AdaBoost Tracking

POP Post Office Protocol

RGB Red-Green-Blue

ROI Region of Interest

SIFT Scale-Invariant Feature Transform

SVM Support Vector Machine

TCE Traditional Contrast Enhancement

TLD Tracking-Learning-Detection

TPU Tensor Processing Unit

TTT Tiered Template based Tracking

UAV Unmanned Aerial Vehicle

Chapter 1 Introduction

1.1 Statement of the Problem

Mobile robotics has always been an attractive field of research that combines many different ideas and approaches to build mechatronic systems, an example is the Unmanned Aerial Vehicle (UAV). A UAV can be defined as a generic aircraft designed to operate with no human pilot onboard. Although, the motivation of the development of early UAV was primarily due to military needs, nowadays, UAV has become a popular platform for many different applications due to its low cost and high flexibility. They are mainly used for tasks that are usually labour intensive, dull, time consuming or dangerous for humans to operate, such tasks can include surveillance, mapping, inspection, rescue and target pursuit, some examples of UAVs and their applications are shown in Fig. 1.

Among the applications, target pursuit using UAV is an innovative but problematic area of research [1–10]. Target pursuit can be defined as the task of following an object of interest continuously and autonomously. This is done through data fusion based on the sensors of the UAV, typical sensors include but are not limited to: Inertial Navigation System (INS), Global Positioning System (GPS), rangefinders and cameras. INS and GPS tend to be used together for localisation and navigation, INS provides higher accuracy at the local level but suffers from integration drift, while GPS is reliable at global level but suffers from signal inconsistency, the two systems collaborate with each other to eliminate drift and signal errors [11]. Rangefinders such as radar and sonar sensors are typically used to avoid obstacles and locate objects from afar. And, vision sensors such as traditional and thermal imaging cameras are mainly used to locate objects at close range through image processing. This research focuses on the task of target pursuit using primarily monocular vision.

(a) MQ-9 Reaper for military operation

(b) Amazon Prime Air for commercial delivery*

(c) Little Ripper Lifesaver for ocean rescue†

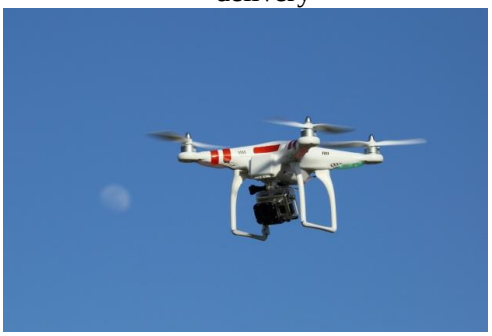

(d) DJI Phantom with GoPro camera for recreational use‡

(e) Nano Hummingbird for surveillance and reconnaissance

(f) The Parrot AR Drone for this research

Figure 1 Some examples of UAVs and their applications

https://www.flickr.com/photos/135518748@N08/37078925214

†*https://www.engadget.com/2018/01/18/little-ripper-lifeguard-drone-rescue*

‡*https://commons.wikimedia.org/wiki/File:Drone_with_GoPro_digital_camera_mounted_underneath_-_22_April_2013.jpg*

In computer vision, target pursuit is a complex problem as it involves the solving of many sub-problems which are typically concerned with the detection, tracking and following of the object of interest. Moreover, issues such as localisation, path planning, obstacle avoidance and multi-robot cooperation can also be included. Despite these hurdles, interest of target pursuit using UAV is rising. Many methods have been proposed through the years, but the majority of them are developed using computer simulation with the assumption of ideal environmental factors [1–5]. Despite a thorough search of the relevant literature, only a few practical vision based methods that focused on target pursuit (such as human following) can be found [6–10], but these methods tend to be designed for tracking and following simple objects. Current research in this topic is clearly lacking of reliable practical vision based approaches.

Furthermore, to the best of author's knowledge, all existing methods require manual selection of the object of interest, this is typically done through the use of pre-defined Region of Interest (ROI). This means that at the beginning of each tracking sequence, the user needs to setup a target ROI which is usually represented by a bounding box of the object. In this research, the object of interest is considered to be unknown at the start, the only input required is a photo of the object, the actual ROI of the object in the image is acquired automatically.

1.2 Aims and Objectives

At present, the majority of related existing methods are developed using computer simulation with the assumption of ideal environmental factors, while the remaining few practical methods are mainly developed to track and follow simple objects that contain monochromatic colours with very little texture variances. Current research in this topic is lacking of practical vision based approaches. Thus, the aim of this research is to fill the gap by developing a real-time algorithm capable of following a person continuously given only a photo input. As this research considers the whole procedure as an autonomous system, the drone should activate automatically upon receiving a photo of a person through Wi-Fi, this means that whole system can be triggered by simply emailing a single photo from any device anywhere. For example,

taking a photo of a person and emailing to the drone 30 kilometres away should activate it and it should start searching for that person. Additionally, this research is aimed to contribute in practical applications using computer vision especially in detecting and tracking of objects.

To achieve the aims, the major objectives of this research have been set out as follows:

- To improve the detection and tracking of objects by studying existing colour models.
- To develop human detection methods capable of extracting the human figure from a given image.
- To develop object tracking methods capable of tracking the target object continuously.

1.3 Summary of Contributions

Given the stated aims and objectives, the contributions of this thesis include:

- A colour enhancement method for improved colour segmentation which focused on boosting the saliency level of the critical regions in the image by maximising chroma while preserving the hue angle.
- A colour identification method for improved colour extraction which relied on a colour space selection scheme to find the most suitable hue based colour space, the required colour is then identified through a multi-channel filtering process.
- A colour model for improved colour detection which consists of three colour components: hue, purity and brightness. It can be represented in three different geometric shapes: sphere, hemisphere and cylinder, each of these shapes also contains two variations.
- A human detection method to identify a person from a photo, then extract and segment the human figure into three key parts: head, upper body and

lower body. The proposed method works by detecting face, head and shoulder separately, mainly using gradient maps.

- An object tracking method to track an object continuously and robustly in real time. The key strategies of the proposed method are: combining intensity template matching with colour histogram model to increase tracking robustness, employing a three-tier system to store templates, applying update and tracking policies for template management.

1.4 List of Publications (Resulting from this Research)

The publications consist of five conference papers and one journal article, the list is shown below from latest to earliest:

- F. Su, G. Fang, and J. J. Zou, "Robust real-time object tracking using tiered templates," The 13th World Congress on Intelligent Control and Automation, Changsha, China, July 2018 (to appear).
- F. Su, G. Fang, and J. J. Zou, "A novel colour model for colour detection," Journal of Modern Optics, vol. 64, no. 8, pp. 819–829, November 2016.
- F. Su, G. Fang, and J. J. Zou, "Human detection using a combination of face, head and shoulder detectors," IEEE Region 10 Conference (TENCON), Singapore, pp. 842–845, November 2016.
- F. Su, and G. Fang, "Chroma based colour enhancement for improved colour segmentation," The 9th International Conference on Sensing Technology, Auckland, New Zealand, pp. 162–167, December 2015.
- F. Su, and G. Fang, "Colour identification using an adaptive colour model," The 6th International conference on Automation, Robotics and Applications, Queenstown, New Zealand, pp. 466–471, February 2015.
- F. Su, and G. Fang, "Human detection using gradient maps and golden ratio," The 31st International Symposium on Automation and Robotics in Construction and Mining, Sydney, Australia, pp. 890–896, July 2014.

1.5 Outline of the Thesis

After the introduction, the rest of the thesis is organised as follows:

- **Chapter 2** reviews the existing research in the related literature which include computer vision, feature detection, colour models, machine learning, human detection, object tracking, target pursuit using UAV and motion control of quadrotor.
- **Chapter 3** details the proposed methods in colour based feature detection which include a colour enhancement method for colour segmentation, a colour identification method and a colour model for improved colour detection.
- **Chapter 4** presents the proposed methods in object detection and tracking, in which a human detection method using gradient maps and an object tracking method using tiered templates are introduced.
- **Chapter 5** provides the results of the target pursuit experiment with three different modes: standby, sentry and search. Other related topics including depth estimation and trajectory mapping are also explained.
- **Chapter 6** discusses the effectiveness of the proposed methods and concludes the completed work with suggestions for potential future work.

Chapter 2 Literature Review

This chapter provides a detailed analysis of related literature in computer vision. Section 2.1 presents an overview of computer vision. Sections 2.2, 2.3 and 2.4 examine three main types of features: edge based, colour based and motion based, respectively. Section 2.5 analyses the currently known colour models. Section 2.6 details the concept of machine learning. Sections 2.7 and 2.8 review existing human detection and object tracking methods, respectively. Section 2.9 provides the background information about UAV and its usage in vision based target pursuit and Section 2.10 explains the motion control of quadrotor.

2.1 Computer Vision

A picture is worth a thousand words, this can be true for humans as we are able to convey the meaning or essence very effectively by identifying or at least guessing the objects, events and locations within an image. However, this can be a complex problem for a computer to solve, for example, given the photo in Fig. 2, if the question is "What is happening in the photo?", this will be a very simple and straightforward question for a human to answer. On the other hand, in order for a computer to truly answer this question, it needs to identify the deer and the tiger, recognise they are both running in the wildness and the tiger is chasing the deer, or perhaps even detect the mood of the deer as desperate and scared, therefore concludes the meaning of the photo as tiger hunting deer in wildness or simply as hunting.

Since a digital image is really a large Two-Dimensional (2D) matrix captured of a Three-Dimensional (3D) scene, so the actual problem for the computer to solve is to describe a 3D scene by extracting meaningful elements from a 2D matrix, this can be done through image processing and pattern recognition which are the two most common procedures in computer vision. Image processing is the study of techniques that involves transforming, improving and analysing digital images to obtain specific meaningful information [12]. While pattern recognition is a branch that is concerned

with the classification of data based either on a prior knowledge or statistical information extracted from patterns [13].

Figure 2 Example problem in computer vision: tiger + deer + wilderness + chasing = hunting ?[*]

In human vision, light is converted into electrochemical signals in the retina and then transmitted to the brain. This is done through the rods and cones located in the photoreceptor layer of the retina which also separate the light into red, green and blue, as shown in Fig. 3. The projection from the retina is sent to a part of the thalamus at the centre of the brain via optic nerve, that part of the thalamus is called Lateral Geniculate Nucleus (LGN). LGN separates the retina inputs into parallel streams which consists mainly of colour, edge and motion.

Compared to converting light into electrochemical signals in human vision, computer vision relies on image sensor to convert light into electrons. The input of computer vision is digital images which are obtained from digital cameras, the images are captured using an electronic image sensor, typically a Charge Coupled Device (CCD) or a Complementary Metal Oxide Semiconductor (CMOS). Both of these two sensors are designed to convert light into electrons, CCD contains more pixels and

[*] *https://commons.wikimedia.org/wiki/File:Tiger_chasing_a_deer_cropped.jpg*

the image quality tends to be higher, while CMOS consumes less power and the cost of manufacturing tends to be lower. In order to capture colours, a colour separation mechanism is needed, the most common method is the Bayer filter which is a Red-Green-Blue (RGB) colour filter array that separates the incoming light into red, green and blue similar to the mechanism of rods and cones in the retina [14], as shown in Fig. 4.

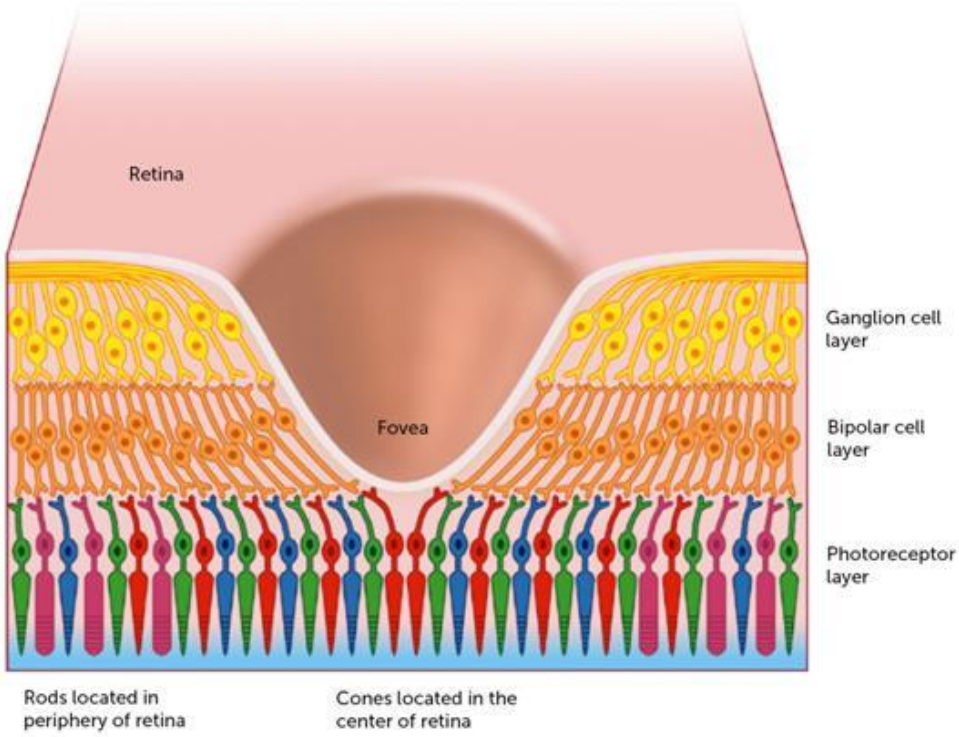

Figure 3 Photoreceptor layer in human vision*

*https://www.brainhq.com/sites/default/files/images/vision-works-01.png

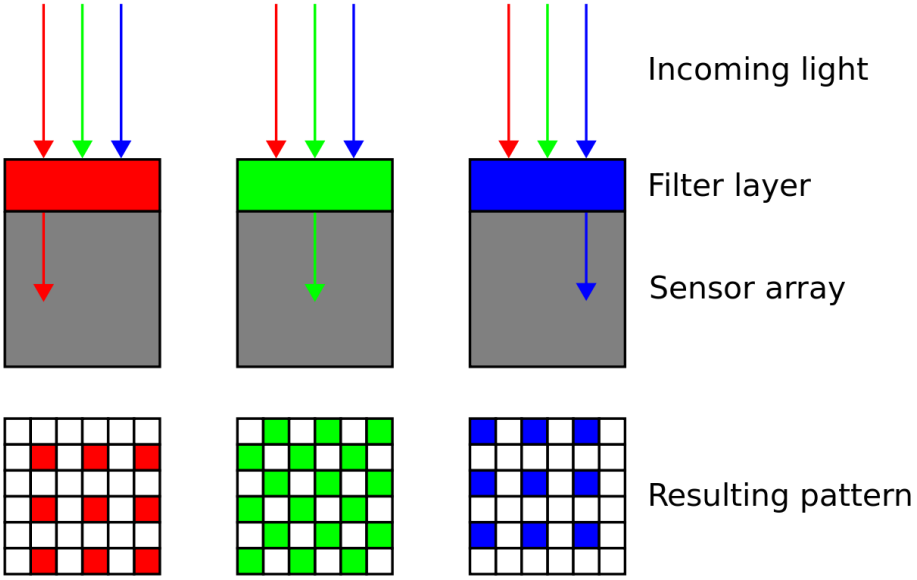

Figure 4 Bayer filter in computer vision*

Computer vision is also the core component of artificial intelligence, it can be described as the visual perception component of an ambitious agenda to mimic human intelligence and to endow robots with intelligent behaviour [15]. It is a relatively young field of study that started out in the early 1970s, a timeline of some of the most active research topics in computer vision is shown in Fig. 5. The output of computer vision is a structure of quantitative measurements that describes the scene. Computer vision can therefore be defined as the construction of explicit and meaningful descriptions of physical objects from images [16]. The applications of computer vision can include surveillance such as traffic monitoring [17] and hazard detection [18], navigation such as mapping [19] and autonomous driving [20], object recognitions such as face [21] and gesture [22].

The most crucial part in computer vision is the feature detection. No vision based system can work until good features can be identified and tracked [23]. A feature is typically a small and salient part of an image which can be included as an identifier and descriptor of an object, event or location. When deciding the type of features to

*https://commons.wikimedia.org/wiki/File:Bayer_pattern_on_sensor_profile.svg

utilise, factors such as distinctiveness, quantity, locality and complexity are considered. Over the decades, many types of features have been proposed along with their feature detection methods, the most common types of features are: edge based, colour based and motion based, it is interesting to note that these are the key types of features extracted by LGN in human vision discussed earlier.

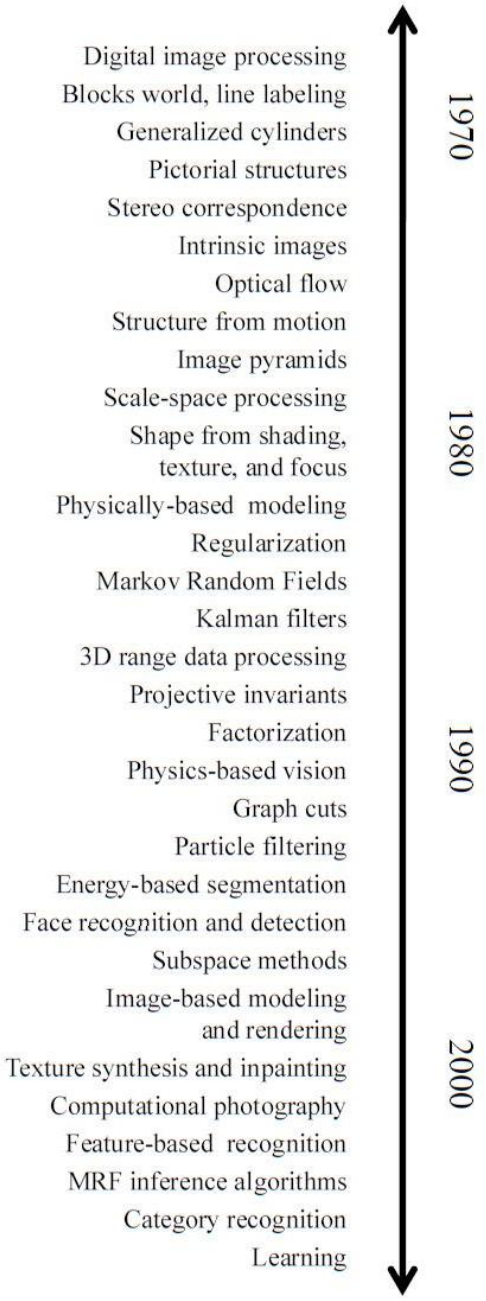

Figure 5 Timeline of computer vision [12]

2.2 Edge Features

Edges can be defined as significant local changes of intensity [24]. In computer vision, they usually occur on the boundary between two different regions in an image due to discontinuities. These discontinuities are the products created by different objects, surfaces, reflections and shadows. Edge detection is the process of finding meaningful transitions caused by local intensity differences in an image, because of this, the majority of edge detectors are gradient based, that is measuring the intensity gradients pixel by pixel, as given in Fig. 6. The origin is proposed to be the top left corner of the image with positive directions of *x* and *y* axes to the right and the bottom, respectively. There is a great deal of diversity in the applications of edge detection, these can include barcode scanner [25], text detection [26], defect detection [27], face recognition [28], autonomous driving [29] and 3D modelling [30].

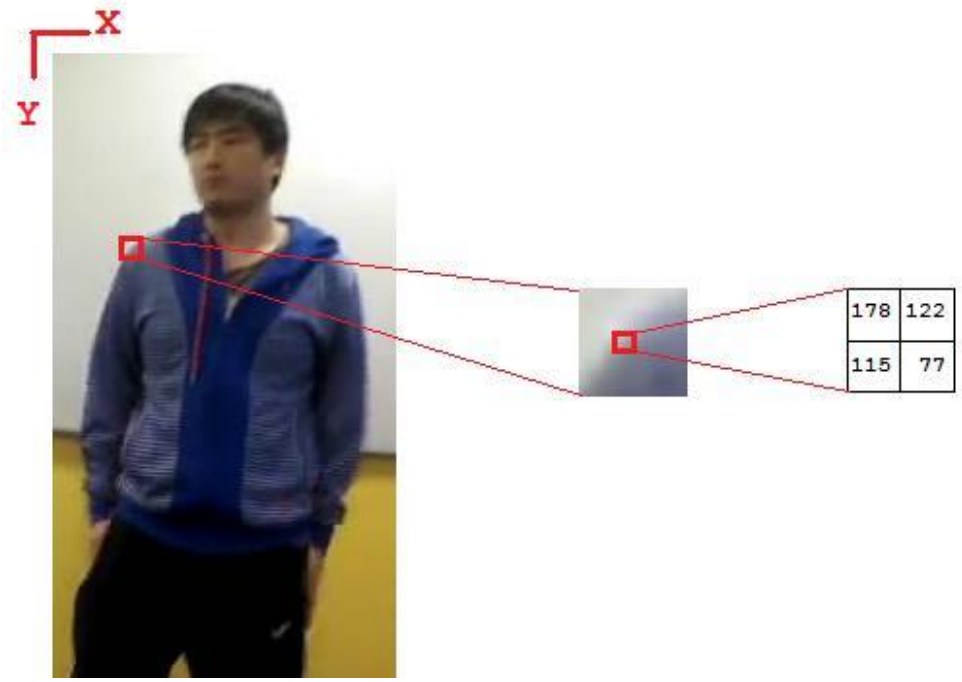

Figure 6 Gradient based edge features

2.2.1 Roberts

A basic method in edge detection is the Roberts edge detector [31]. This method calculates the intensity difference between adjacent pixels by using two operator masks or kernels, as given in (1) and (2).

$$G_a = \begin{bmatrix} -1 & 0 \\ 0 & 1 \end{bmatrix} \quad (1)$$

$$G_b = \begin{bmatrix} 0 & -1 \\ 1 & 0 \end{bmatrix} \quad (2)$$

where G_a and G_b are the gradient filters along the diagonal axes *a* and *b*, respectively.

Roberts edge detector is perhaps the simplest filter to use for finding edges, it is known to preserve the position of the edge, but can be prone to noises.

2.2.2 Prewitt

Another method is the Prewitt edge detector [32]. Compared to the Roberts detection, instead of finding the diagonal intensity difference, this method relies on finding the central difference by comparing neighbouring pixels horizontally and vertically, the Prewitt operator masks are given in (3) and (4).

$$G_x = \begin{bmatrix} -1 & 0 & 1 \\ -1 & 0 & 1 \\ -1 & 0 & 1 \end{bmatrix} \quad (3)$$

$$G_y = \begin{bmatrix} -1 & -1 & -1 \\ 0 & 0 & 0 \\ 1 & 1 & 1 \end{bmatrix} \quad (4)$$

where G_x and G_y are the gradient filters along *x* and *y* axes, respectively.

Prewitt edge detector obtains mono-directional gradients along *x* and *y* axes, it tends to have a fair degree of noise resistance.

2.2.3 Sobel

Another method is the Sobel edge detector [33]. Sobel is similar to the Prewitt, the only difference is Sobel emphasises more on the importance of the central pixels by assigning more weight, the Sobel operator masks are given in (5) and (6).

$$G_x = \begin{bmatrix} -1 & 0 & 1 \\ -2 & 0 & 2 \\ -1 & 0 & 1 \end{bmatrix} \tag{5}$$

$$G_y = \begin{bmatrix} -1 & -2 & -1 \\ 0 & 0 & 0 \\ 1 & 2 & 1 \end{bmatrix} \tag{6}$$

where G_x and G_y are the gradient filters along x and y axes, respectively.

Since the distribution of weight is less at the corners, Sobel is thought to possess slightly better noise suppression when compared to Prewitt, but it may produce more edge discontinuities.

2.2.4 LOG

The methods described so far are all first order derivative based, but it is not the only tool to extract gradient based edge features. Second order derivatives can also be used, an example is the Laplacian of Gaussian (LOG) edge detector [34]. Gaussian filter is first implemented to reduce the noise level by smoothing the image, this is the same procedure employed in Canny. Laplacian is then applied to obtain edge features by finding zero crossings of the second order derivative. Only one Laplacian operator mask is required, the most commonly used kernel is given in (7).

$$L = \begin{bmatrix} -1 & -1 & -1 \\ -1 & 8 & -1 \\ -1 & -1 & -1 \end{bmatrix} \tag{7}$$

where L is the Laplacian filter.

Because of the second order derivative nature of the LOG edge detector, it tends to yield better results with clustered objects when compared to the first order approaches. However, LOG is known to be relatively prone to background noise and it has an inclination to generate closed contours which do not always represent actual edges.

2.2.5 Canny

A more advanced and well known method is the Canny edge detector [35]. Canny implements a multi-staged algorithm to detect a wide range of edges in images, it is aimed to achieve minimum detection error while maintaining good edge localisation.

The first step of the Canny method involves filtering out noise using a Gaussian filter, as given in (8).

$$g(x,y) = ae^{-\frac{x^2+y^2}{2\sigma^2}} \tag{8}$$

where x and y are the distances from the specific pixel of consideration in the horizontal and vertical axes, respectively, a is the scale factor with overall magnitude equal to 1 and σ is the standard deviation of the Gaussian distribution.

Commonly, a Gaussian kernel with a dimension of 5 ×5 and σ = 1.4 is used, as given in (9).

$$g = \frac{1}{159}\begin{bmatrix} 2 & 4 & 5 & 4 & 2 \\ 4 & 9 & 12 & 9 & 4 \\ 5 & 12 & 15 & 12 & 5 \\ 4 & 9 & 12 & 9 & 4 \\ 2 & 4 & 5 & 4 & 2 \end{bmatrix} \tag{9}$$

where g is the Gaussian filter.

The second step involves finding the gradient magnitude and orientation, gradient can be computed with any of the previously mentioned masks, Sobel is commonly

selected due to its resemblances to a Gaussian kernel. The equations for calculating the magnitude and orientation are given in (10) and (11).

$$G = \sqrt{G_x^2 + G_y^2} \tag{10}$$

$$\theta = \tan^{-1}(\frac{G_y}{G_x}) \tag{11}$$

where G_x and G_y are the gradient components along x and y axes, respectively. θ is rounded to one of four main directions: horizontal (0 °or 180 °), vertical (90 °or 270 °) and two diagonals (45 °or 225, and 135 °or 315 °).

The third step is a non-maximum suppression procedure, in which any pixel along the direction of the gradient of a ridge with non-peak value is removed. This results in an edge thinning effect by removing pixels that are not considered to be part of an edge.

The final step is a hysteresis thresholding procedure, in which two values (upper and lower) are used for thresholding. If the gradient of a pixel is higher than the upper threshold, the pixel is accepted as an edge. If the value is below the lower threshold, then the pixel is removed. If the value is in between the two thresholds, then it is accepted only if the pixel itself is connected to another pixel that is above the upper threshold. It is commonly recommended to select the two thresholds with an upper to lower ratio between 2 and 3.

Due to its low computational cost and high robustness, Canny edge detector is widely used for many different applications. However it has some limitations [36]: firstly, because of its dual-threshold nature, the optimal window of the upper and lower thresholds is difficult to adjust. Secondly, corner pixels tend to search in the wrong directions of their neighbours, which frequently causing open ended edges. Furthermore, positions of the edges are usually shifted due to the blurring effect of the Gaussian filter.

Examples of results using different edge detectors are illustrated in Fig. 7. The results are generated by computing gradient magnitude maps based on the kernels described earlier, they are also normalised for visualisation and comparison purposes. For first order derivative based methods that compute gradients along both x and y axes, the overall magnitudes are obtained using (10). For Canny, rather than choose the upper and lower thresholds manually, they are obtained based on the mean magnitude of Sobel. This automatic threshold selection approach proves to be effective for most images, the mean value is linked to the lower threshold and the upper threshold is simply two times the mean.

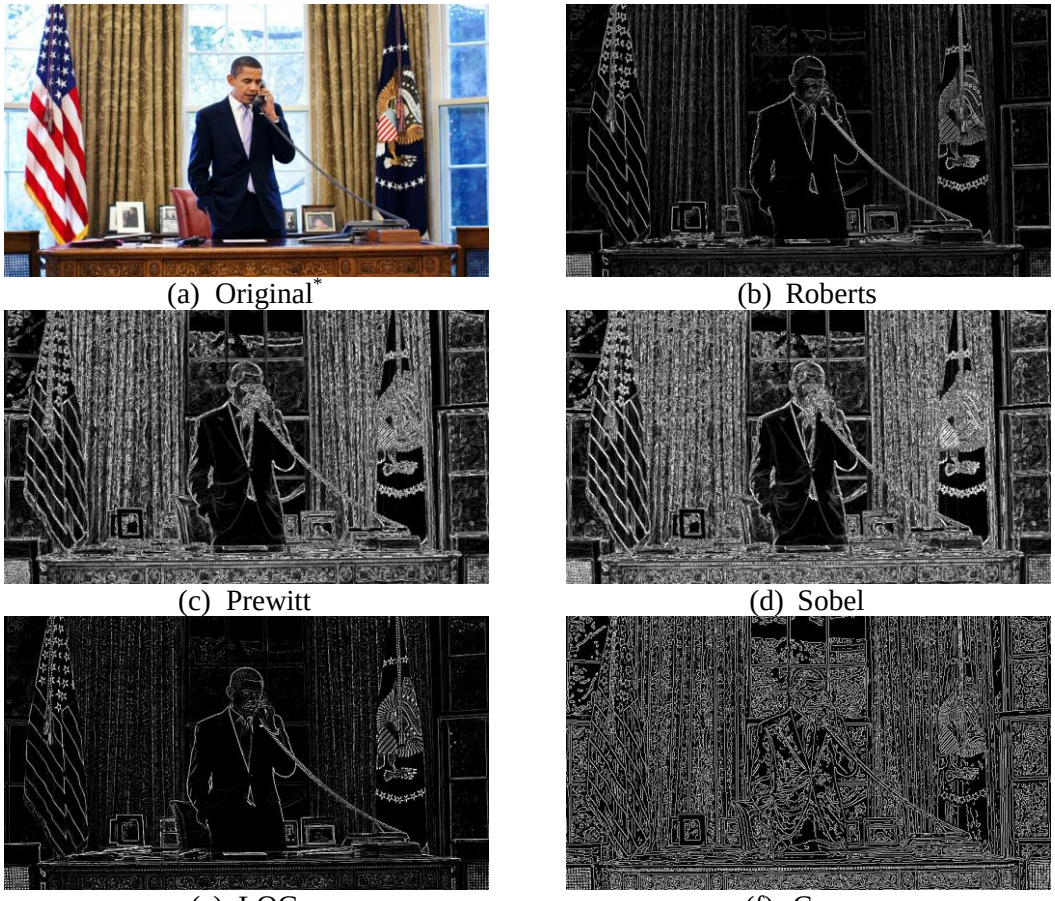

(a) Original* (b) Roberts

(c) Prewitt (d) Sobel

(e) LOG (f) Canny

Figure 7 Example results of edge detection

*https://peopledotcom.files.wordpress.com/2017/10/obama-oval-office.jpg

2.3 Colour Features

Colour is an important feature in both human vision and computer vision, it can be defined as the perceptual sensation of the spectral distribution of visible light [37]. Visible light is basically electromagnetic radiation with typical wavelength ranging from 400 to 700 nanometres, as shown in Fig. 8. Therefore it can be said that the colour of an object depends on the wavelength of the light leaving its surface.

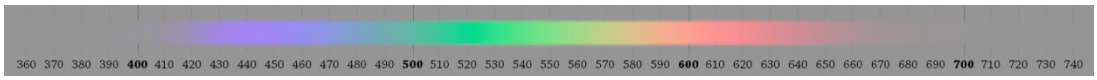

Figure 8 Colours in visible spectrum based on wavelength (nanometres)*

In computer vision, colour segmentation is the process of partitioning an image into meaningful regions based on colour properties. Because each person perceives the boundaries of colours differently, this means that the ground truth of colour regions varies depending on the observer. Furthermore, environment factors such as lighting, shadow and viewing angle can also greatly influence the perception of colours, thus colour segmentation can be a challenging task. It can be commonly found in applications that rely on the detection and tracking of various colours, these can include remote sensing [38], object tracking [39], skin segmentation [40], tumour detection [41], road lane detection [42] and 3D modelling [43].

Colour features can be defined subject to particular colour spaces [44], a number of colour spaces have been proposed in the literature and are to be discussed in detail in Section 2.5. For simplicity, only the RGB colour space is considered for colour segmentation methods discussed in this section.

2.3.1 Simple Thresholding

A simple method to separate the colours is thresholding based on Euclidean distance [45]. An example approach is to divide the RGB colour space into 8 colours then

*https://en.wikipedia.org/wiki/File:Rendered_Spectrum.png

classify the pixels based on minimum squared Euclidean distance to the absolute values of these colours, as listed in Table I. For a typical 8-bit colour image, RGB values are in range of 0 to 255.

TABLE I SIMPLE 8 COLOURS CLASSIFICATION

Colours	Red	Green	Blue
Red	255	0	0
Green	0	255	0
Blue	0	0	255
Yellow	255	255	0
Cyan	0	255	255
Magenta	255	0	255
Black	0	0	0
White	255	255	255

The squared Euclidean distance of individual pixels to the absolute colours (defined as 8 vertices of the RGB cube) is computed using (12).

$$d_i{}^2 = (R_a - R_i)^2 + (G_a - G_i)^2 + (B_a - B_i)^2 \quad (12)$$

where *d* is the distance, *a* and *i* are the absolute and pixel colours, respectively, *R*, *G* and *B* are the RGB positions or pixel values, respectively.

Thresholding based methods are built based on the principle that different regions of the image can be separated by identifying important characteristics such as local maxima and minima, they are simple to implement but can be sensitive to noise.

2.3.2 Histogram Binning

A common feature in colour segmentation is colour histogram which is basically a representation of colour distributions in an image. In the RGB colour space, a colour histogram represents the count of number of pixels in an image belonging to a particular RGB bin, these histogram bins are used to quantise the pixels into different

regions. For example, an image can be segmented using 4-bin 64 colours classification, the range of pixel values is listed in Table II.

TABLE II 4-BIN 64 COLOURS CLASSIFICATION

Colour Channels	Bin 1	Bin 2	Bin 3	Bin 4
Red	0-63	64-127	128-191	192-255
Green	0-63	64-127	128-191	192-255
Blue	0-63	64-127	128-191	192-255

2.3.3 Otsu

Since the range and boundaries of the bins are fixed, this can be a problem for certain images with the majority of pixels lie in between the boundaries. A more reliable approach is the Otsu's method [46], this method can be applied to adaptively determine the optimum threshold of an image. This is done by searching for the threshold that minimises the intra-class variance or the with-in class variance. This is the same as maximising the inter-class variance or the between-class variance, as given in (13).

$$\sigma^2 = \omega_1(\mu_1 - \mu_I)^2 + \omega_2(\mu_2 - \mu_I)^2 \tag{13}$$

where σ^2 is the inter-class variance, ω_1 and ω_2 are the probabilities of the first and second class, respectively, μ_1, μ_2 and μ_I are the weighted means of the first class, second class and the entire image, respectively.

The probabilities ω_1 and ω_2 of class occurrence are determined using (14) and (15).

$$\omega_1 = \sum_{i=0}^{t} \frac{f_i}{A} \tag{14}$$

$$\omega_2 = \sum_{i=t}^{B-1} \frac{f_i}{A} \tag{15}$$

where f_i is the frequency of bin i, B is the total number of bins, A is the area or the total number of pixels and t is the threshold.

The weighted means of the probability distributions are obtained using (16) to (18).

$$\mu_1 = \sum_{i=0}^{t} \frac{if_i}{\omega_1 A} \tag{16}$$

$$\mu_2 = \sum_{i=t}^{B-1} \frac{if_i}{\omega_2 A} \tag{17}$$

$$\mu_I = \sum_{i=0}^{B-1} \frac{if_i}{A} \tag{18}$$

Otsu's method is essentially a binarisation procedure that separates the pixels into two classes, it can be very effective at finding the optimal threshold if the histogram of the image possesses bimodal distribution. However, for histograms with multimodal distributions that contain multiple modes, it becomes unreliable.

To adapt the method for classification of more than two groups with multiple thresholds, (13) can be modified into (19).

$$\sigma^2 = \sum_{c=1}^{C} \omega_c(\mu_c - \mu_I)^2 \tag{19}$$

where σ^2 is the inter-class variance, ω_c is the probabilities of class c, C is the total number of classes, μ_c and μ_I are the weighted means of class c and the entire image, respectively.

For example, an image can be segmented into 4 classes in each of the RGB channels using the modified equation above. This classifies the pixels into 64 colours similar to the 4-bin histogram approach listed earlier in Table II, except the range and boundaries are now determined adaptively to the histogram distribution instead of fixed.

For a given image, histogram based methods exhibit relatively good performance if the variance of the foreground is small and the mean difference compared to the background is high. However, it has limited usage against images that contain no obvious valley and peak regions.

2.3.4 K-means

Another popular approach in colour segmentation is clustering such as the K-means [47] and mean shift [48]. K-means clustering based methods [47] assume that the image contains at least two unique clusters and they can be separated by associating every observation with the nearest cluster centre. The cluster centres are typically initialised randomly first, then followed by two key steps: assignment and update. Assignment step is implemented to assign each observation to the cluster based on minimum squared Euclidean distance to the cluster centres, similar to (13). The update step is responsible for updating the cluster centres by calculating the new means for each cluster, as given in (20). These two steps repeat until convergence is achieved.

$$[R_c \quad G_c \quad B_c] = \frac{1}{N}\sum_{n=1}^{N}[R_n \quad G_n \quad B_n] \tag{20}$$

where *R*, *G* and *B* are the red, green and blue pixel intensities, respectively, *c* and *n* represent the cluster centre and individual pixel belonging to the cluster, respectively, *N* is the maximum number of pixel belonging to the cluster.

2.3.5 Mean Shift

Mean shift clustering based methods [48] assume that the image contain some unknown density function that can be approximated by smoothing each observation in the region around it and by locating the local maxima of the density function. Firstly, a random observation is initialised as the mean. Secondly, for each observation, the squared Euclidean distance to the mean is calculated, similar to (13).

Thirdly, a vote is added to the observation if it is deemed close to the mean, this is determined if the distance to the mean is smaller than a radius threshold. Finally, the mean is updated based on all the observations close to the mean, this is basically a gradient descent process which shifts the mean towards a local minimum, similar to (20). These steps repeat until convergence is achieved. The cluster and its votes are merged into another cluster if it is found within half of the radius threshold of any existing clusters, else it is regarded as a new cluster. For the merging case, the combined mean of the two clusters is determined based on the maximum of the cluster votes, as given in (21) and (22). An unvisited observation is then initialised as the new mean and whole procedure repeats until all observations have been visited.

$$\alpha = \frac{\max(V_i)}{\max(V_i) + \max(V_m)} \tag{21}$$

$$\mu_m = \alpha\mu_i + (1 - \alpha)\mu_m \tag{22}$$

where V and μ are the votes (of the pixels) and means belonging to the clusters, respectively, i and m are the current and merging clusters, respectively.

Both K-means and mean shift require only a single input, but the inputs for both methods are difficult to set. They are typically determined empirically depending on the applications. For K-means the input is the total number of clusters, while for mean shift, the input is the radius of the Region of Interest (ROI). K-means is usually computationally inexpensive, but can be sensitive to outliers and requires pre-knowledge of the number of segmentations needed. On the other hand, mean shift automatically determines the number of segmentations based on the radius input. However, it does not scale well with more than one dimension of feature space as it is computationally expensive.

Examples of results using different colour segmentation methods described earlier are illustrated in Fig. 9. The results are normalised for visualisation and comparison purposes. Two cases have been considered: 8 segments and 27 segments. For histogram, 8 and 27 segments are the results of quantisation using 2-bin and 3-bin in each channel of the RGB colour space, respectively. For Otsu's method, 8 and 27

segments are the results of thresholding by finding one and two optimal thresholds per RGB channel, respectively. For mean shift, the specific numbers of segments are generated through trial and error since mean shift does not guarantee number of segments in the outcome.

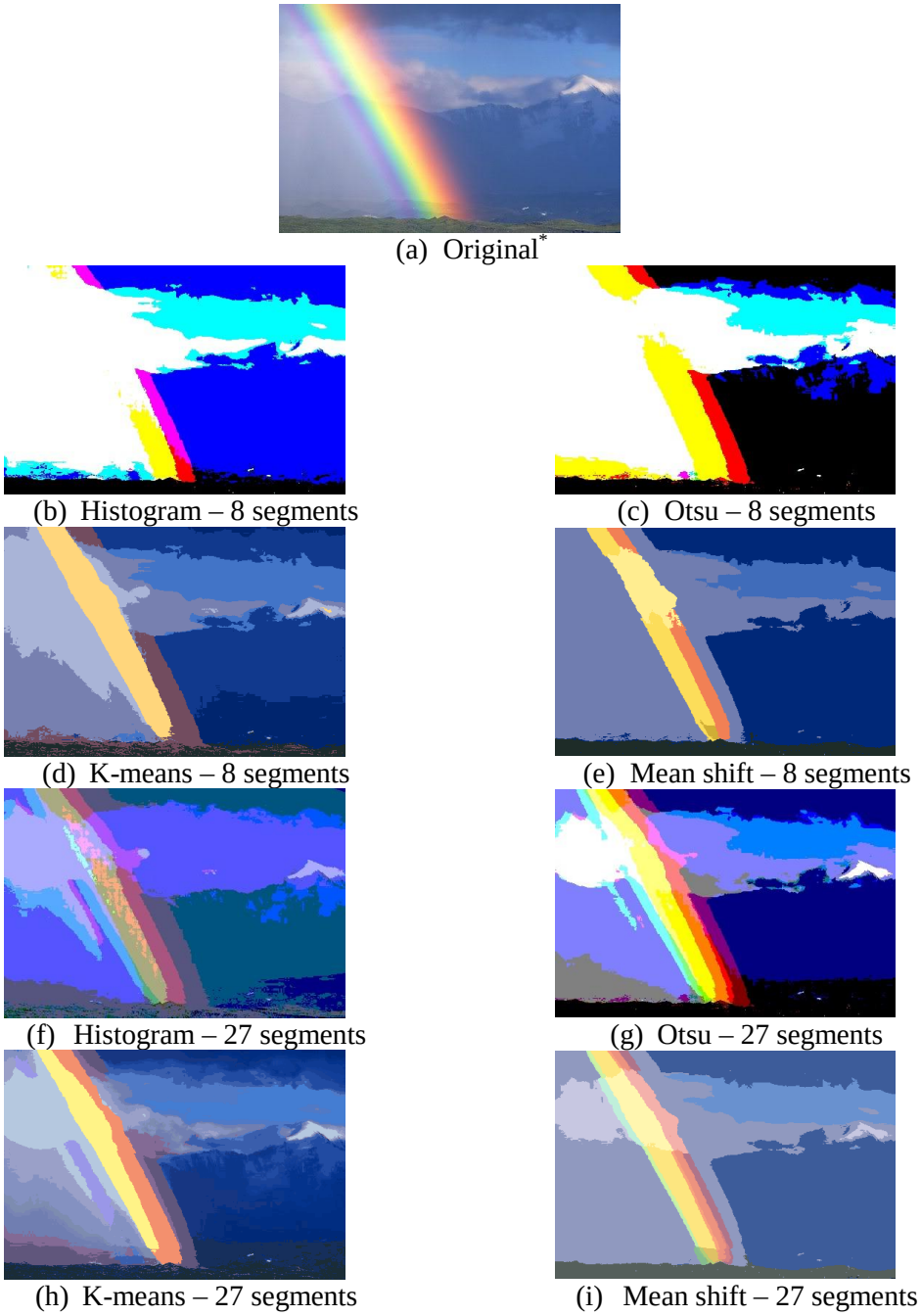

(a) Original*

(b) Histogram – 8 segments

(c) Otsu – 8 segments

(d) K-means – 8 segments

(e) Mean shift – 8 segments

(f) Histogram – 27 segments

(g) Otsu – 27 segments

(h) K-means – 27 segments

(i) Mean shift – 27 segments

Figure 9 Example results of colour segmentation

*http://www.maxtheknife.com/marshax3/marsha36.jpg

2.4 Motion Features

In physics, motion is defined as the change in position of an object over time relative to a frame of reference. In computer vision, motion is detected by comparing two consecutive image frames in a sequence. Motion features are extracted to analyse the objects for advanced purposes or simply to detect and track the objects in the first place. Basic analysis can be performed to obtain important characteristics about the objects, these can include shape, posture, centre of mass, velocity and trajectory. Further advanced analysis can lead to action recognition [49], behaviour recognition [50], object recognition [51] and object reconstruction [52]. There are two well known motion detection methods that have been used extensively throughout the years: background subtraction [53] and optical flow [54].

2.4.1 Background Subtraction

Background subtraction [53] is typically used to separate moving foreground objects from static background. The fundamental assumption of the algorithm is that the background remains relatively stable when compared to foreground objects. When objects move in a set of video frames, the regions that differ significantly from the background model can be considered to be the foreground. In other words, when assuming a statistical model of the scene, an intruding object can be detected by spotting the parts of the image that don't belong to the model.

A vast amount of research has been conducted with many algorithms proposed. The simplest way of achieving background subtraction is the frame difference method, in which the background is estimated from the previous frame according to an intensity difference threshold, as given in (23).

$$|I_t - I_{t-1}| > \Delta \tag{23}$$

where I_t is the intensity of frame t, Δ is the intensity difference threshold.

This basic method only relies on a single threshold which controls the sensitivity of the separation between the foreground and background, this threshold is linked to the speed of the moment so that a high threshold is required for fast movement. This method is only suited for a particular moment in the scene and is very sensitive to noise.

A more refined and renowned method is the Gaussian Mixture Model (GMM) [55]. GMM models each background pixel by a mixture of Gaussian distributions (a small number usually from 3 to 5). The probability of observing the current pixel value is given in (24).

$$P(X_t) = \sum_{i=1}^{K} \omega_i \eta(X_t, \mu_i, \Sigma_i) \tag{24}$$

where $P(X_t)$ is the probability of observing pixel value X at time t, K is the number of Gaussians in the model, ω_i is the weight parameter of Gaussian i, $\eta(X_t,\mu_i,\Sigma_i)$ is the normal distribution of Gaussian i with mean μ_i and covariance Σ_i.

Gaussians are employed to indicate different colours. The weight parameter is used to represent the time that those colours stay in the scene and is updated at every new frame. The mean value and covariance matrix are needed to compute Gaussian probability density function.

To find the foreground, background pixels can be assumed to have high weight values and low variance values because they remain longer and are more static when compared to the foreground objects. A fitness value is introduced to measure the formation of the clusters, in which static single colour objects tend to form tight clusters, while moving ones tend to form wide clusters caused by reflections from different surfaces due to the movement. During the update, every new pixel is checked against existing model for fitness measure and is updated according to a specific learning rate.

An enhanced version of GMM is the Improved Gaussian Mixture Model (IGMM) [56]. IGMM argues that the original GMM takes too many frames for components to be included as part of the background especially in busy environments. The proposed solution is to remove the likelihood factor because it causes slow adaptations in the means and the covariance matrices which can result in failure of the tracker. Another improvement is the inclusion of an online expectation maximization algorithm, in which an initial estimate is provided using expected sufficient statistics update equations before enough samples can be collected. This means that the model is updated differently depending on the phase, as given in (25) to (29).

$$\alpha = \frac{P(\omega_k|X_{t+1})}{\sum_{i=1}^{t+1} P(\omega_k|X_i)} \tag{25}$$

$$\beta = (X_{t+1} - \mu_{k,t})\,(X_{t+1} - \mu_{k,t})^B \tag{26}$$

$$\omega_{k,t+1} = \begin{cases} \omega_{k,t} + \dfrac{1}{t+1}\big(P(\omega_k|X_{t+1}) - \omega_{k,t}\big), & t < T \\ \omega_{k,t} + \dfrac{1}{T}\big(P(\omega_k|X_{t+1}) - \omega_{k,t}\big), & t \geq T \end{cases} \tag{27}$$

$$\mu_{k,t+1} = \begin{cases} \mu_{k,t} + \alpha\big(X_{t+1} - \mu_{k,t}\big), & t < T \\ \mu_{k,t} + \dfrac{1}{T}\left(\dfrac{P(\omega_k|X_{t+1})X_{t+1}}{\omega_{k,t+1}} - \mu_{k,t}\right), & t \geq T \end{cases} \tag{28}$$

$$\Sigma_{k,t+1} = \begin{cases} \Sigma_{k,t} + \alpha\big(\beta - \Sigma_{k,t}\big), & t < T \\ \Sigma_{k,t} + \dfrac{1}{T}\left(\dfrac{P(\omega_k|X_{t+1})\beta}{\omega_{k,t+1}} - \Sigma_{k,t}\right), & t \geq T \end{cases} \tag{29}$$

where $\omega_{k,t+1}$, $\mu_{k,t+1}$ and $\Sigma_{k,t+1}$ are the estimates of weight, mean and covariance of Gaussian k at time $t+1$, respectively, $P(\omega_k|X_{t+1})$ is the posterior probability of X_{t+1} generating from Gaussian k and is equal to 1 for the matched model and 0 for the remaining models, B is the minimum background parameter which is a percentage measure of the minimum portion of the data to be considered as background, typically a low value is chosen for unimodal distributions and a high value is chosen for multimodal distributions, T is the time or frame threshold for determining the phase.

Initially, when the number of frames is smaller than *T*, the model is updated according to the expected sufficient statistics update equations. Later, when the first *T* samples are processed, the update equations of the model are switched to the *T*-recent window version. The expected sufficient statistics update equations allow faster convergences while still providing a good overall estimation during the initial phase, while the *T*-recent window equations gives priority over recent data, this increases the adaptiveness of the model. Thus, IGMM is able to reduce the computational cost while maintaining accuracy of the model.

In general, with a stationary camera, background subtraction can be an effective tool for motion detection. However, when the camera itself starts moving, background subtraction tends to become unreliable and problematic to implement. This is because with a moving camera, the background of the image is constantly changing, this results in abnormally high variances which leads to failure of the separation as the majority of the image are highly likely to be falsely classified as foreground.

2.4.2 Optical Flow

Optical flow [54] is an alternative and well known method for motion detection. The key idea is to measure the relative motion between the objects and the viewer similar to movement awareness from human vision. This is achieved by analysing the distribution of observed velocity in brightness patterns. Optical flow can also be used to find other important characteristics of the scene, these can include the rate of change which is utilised to estimate the structures of the 3D scenes and the discontinuities which is extracted to distinguish between objects by segmenting images into different regions.

There are two key assumptions for optical flow: temporal persistence and brightness constancy. Temporal persistence assumes that the image motion of a surface path is small and any movement results consistent changes of coordinates, then the following equation can be established, as given in (30).

$$I(x_2, y_2, t_2) = I(x_1, y_1, t_1) + \frac{\partial I}{\partial x}\Delta x + \frac{\partial I}{\partial y}\Delta y + \frac{\partial I}{\partial t}\Delta t \quad (30)$$

where $I(x_i,y_i,t_i)$ is the intensity value of location (x_i,y_i) at time t_i of frame i.

While brightness constancy assumes that intensity values remain the same in a small region even if their locations may change slightly, then the following equation can also be established, as given in (31).

$$I(x_2, y_2, t_2) = I(x_1, y_1, t_1) \quad (31)$$

Based on these assumptions, the velocity equation of optical flow can be established through subtraction and conversion, as given in (32) to (34).

$$\frac{\partial I}{\partial x}\Delta x + \frac{\partial I}{\partial y}\Delta y + \frac{\partial I}{\partial t}\Delta t = 0 \quad (32)$$

$$\frac{\partial I}{\partial x}V_x + \frac{\partial I}{\partial y}V_y + \frac{\partial I}{\partial t} = 0 \quad (33)$$

$$I_x V_x + I_y V_y + I_t = 0 \quad (34)$$

where V_x and V_y are the x and y components of velocity, respectively, I_x, I_y and I_t are the derivatives of the image at (x,y,t) in the corresponding directions, respectively.

Since equation (34) contains two unknowns (V_x and V_y), additional constraint is needed to solve the equation, this is known as the aperture problem [57]. Several methods of solving this problem have been proposed, the most frequently used implementation is the Lucas-Kanade method [58]. In this method, a third key assumption is introduced: spatial coherence. Spatial coherence assumes that neighbouring points belong to the same surface and have similar motions, this means that a window can be used as the input instead of individual pixels, then the following equation can be established, as given in (35).

$$\begin{bmatrix} I_x(1) & I_y(1) \\ \vdots & \vdots \\ I_x(n) & I_y(n) \end{bmatrix} \begin{bmatrix} V_x \\ V_y \end{bmatrix} = - \begin{bmatrix} I_t(1) \\ \vdots \\ I_t(n) \end{bmatrix} \tag{35}$$

where n is the total number of pixels inside the window, V_x and V_y are the x and y components of velocity, respectively, I_x, I_y and I_t are the derivatives of the image at (x,y,t) in the corresponding directions, respectively.

Then, by using the least square approximation, the two unknowns in the optical flow equation described earlier can be solved for all the pixels in the neighbourhood, as given in (36).

$$\begin{bmatrix} V_x \\ V_y \end{bmatrix} = \begin{bmatrix} \sum {I_x}^2 & \sum I_x I_y \\ \sum I_x I_y & \sum {I_y}^2 \end{bmatrix}^{-1} \begin{bmatrix} -\sum I_x I_t \\ -\sum I_x I_t \end{bmatrix} \tag{36}$$

where V_x and V_y are the x and y components of the velocity, respectively, I_x, I_y and I_t are the derivatives of the image at (x,y,t) in the corresponding directions, respectively.

Even when the camera is moving, optical flow can be a quite powerful tool for motion detection, this is because the algorithm relies on local flow vectors rather than the entire image. However, the performance of optical flow is limited by assumptions, such as the brightness in a small region is assumed to remain the same despite changing of its location, which is not always the case. Another problem is that optical flow does not always correspond to the motion field and only the direction of the intensity gradient is measureable, the tangential component on the other hand is unmeasurable.

Examples of the results using motion detection methods described earlier are presented in Fig. 10. The input frames are produced from a video recorded by the front facing camera of a hovering quadrotor. For optical flow, the magnitude of the velocity is increased by a factor for visualisation and comparison purposes

(represented by the green vectors), this factor is equal to 5% of the maximum length (width and height) of the image.

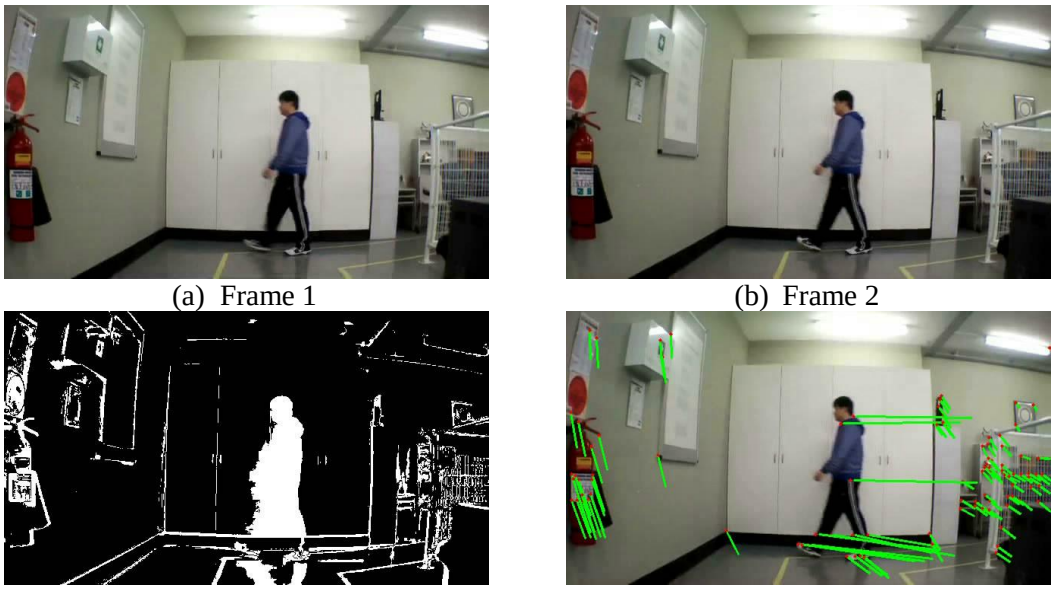

(a) Frame 1 (b) Frame 2

(c) Background subtraction (IGMM) (d) Optical flow (Lukas-Kanade)

Figure 10 Example results of motion detection

2.5 Colour Models

Colour model can be defined as a digital representation of possible contained colours [59]. Many different colour models have been proposed in the literature, each with their own strengths and weaknesses. The most commonly used colour model for capturing images is the RGB model, while hue based colour models such as Hue-Saturation-Value (HSV) are frequently chosen for colour related tasks such as the detection, segmentation and enhancement of colours. Others colour models include luminance based colour models such as YUV and the CIE colour models such as LUV. Existing literature tends to present and discuss the colour models based on 2D cross sections, this can be sometimes misleading especially for colour models with irregular gamuts, therefore in this section, complete 3D models are provided along with their conversions from RGB and vise versa.

2.5.1 RGB

RGB is the most common and fundamental colour model, in which each channel corresponds to the intensity of one of the primary colours: red, green and blue. The standard RGB colour model can be represented as a 3D Cartesian space using three mutually perpendicular axes, as shown in Fig. 11.

Due to its simplicity and its additive property, RGB colour model is very easy to store, configure and display the images [60]. However, as important colour properties, such as purity and brightness, are embedded within the RGB colour channels and any effect or change on one of the channels also affects the other channels, it can be difficult to extract specific colours and to determine their reliable working ranges [61]. Thus, modern methods typically rely on other colour models for colour related tasks.

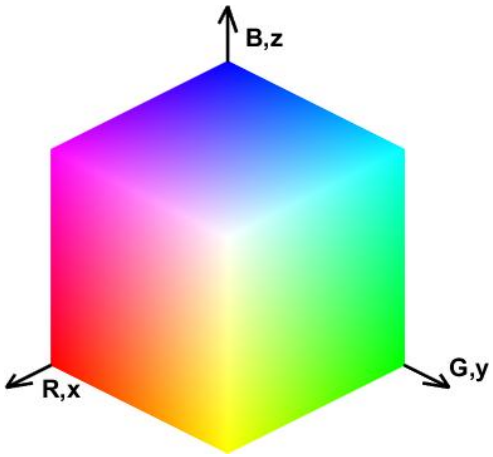

Figure 11 RGB cube

2.5.2 HCV, HCL, HSV and HSL

The most frequently used colour models for colour related applications are the hue based colour models [62]. These can include Hue-Chroma-Value (HCV), Hue-Chroma-Lightness (HCL), Hue-Saturation-Value (HSV) and Hue-Saturation-Lightness (HSL), as shown in Fig. 12 (a) to (d), respectively. In the models, hue represents colour angle, chroma or saturation represents colour purity, value or lightness represents colour brightness.

The conversions from RGB to HCV, HCL, HSV and HSL are given in (37) to (43).

$$U = \min(r, g, b) \tag{37}$$

$$V = \max(r, g, b) \tag{38}$$

$$C = V - U \tag{39}$$

$$L = \frac{V + U}{2} \tag{40}$$

$$S_V = \begin{cases} 0, & V = 0 \\ \dfrac{C}{V}, & V > 0 \end{cases} \tag{41}$$

$$S_L = \begin{cases} \dfrac{C}{2L}, & L \leq 0.5 \\ \dfrac{C}{2(1-L)}, & L > 0.5 \end{cases} \tag{42}$$

$$H = \begin{cases} \left(\dfrac{g-b}{C}\right) 60°, & V = r \\ \left(\dfrac{b-r}{C} + 2\right) 60°, & V = g \\ \left(\dfrac{r-g}{C} + 4\right) 60°, & V = b \end{cases} \tag{43}$$

where r, g, b are the red, green and blue intensities, respectively, V is value, C is chroma, L is lightness, H is hue, S_V and S_L are saturations based on value and lightness, respectively.

The inverse conversions from HCV, HCL, HSV and HSL to RGB are given in (44) to (48).

$$C = \begin{cases} VS, & \text{HSV} \\ (1 - |2L - 1|)S, & \text{HSL} \end{cases} \tag{44}$$

$$U = \begin{cases} V - C, & HCV\ and\ HSV \\ L - \dfrac{C}{2}, & \text{HCL and HSL} \end{cases} \tag{45}$$

$$V = U + C, \quad \text{HCL and HSL} \tag{46}$$

$$M = \begin{cases} U + \left(\dfrac{H \bmod 60°}{60°}\right) C, & H \bmod 120° \leq 60° \\ U + \left(1 - \dfrac{H \bmod 60°}{60°}\right) C, & H \bmod 120° > 60° \end{cases} \tag{47}$$

$$(r, g, b) = \begin{cases} (V, M, U), & 0 \leq H < 60° \\ (M, V, U), & 60 \leq H < 120° \\ (U, V, M), & 120 \leq H < 180° \\ (U, M, V), & 180 \leq H < 240° \\ (M, U, V), & 240 \leq H < 300° \\ (V, U, M), & 300 \leq H < 360° \end{cases} \tag{48}$$

where *r*, *g* and *b* are the red, green and blue intensities, respectively, *V* (value), *M* and *U* are the maximum, middle and minimum intensities among *r*, *g* and *b*, respectively, *C* is chroma, *L* is lightness, *H* is hue and *S* is saturation.

Hue based colour models tend to be the preferred choices for colour detection applications [63], this is because they separate important properties such as purity and brightness from the image and their various colour regions can be easily recognised by human perception.

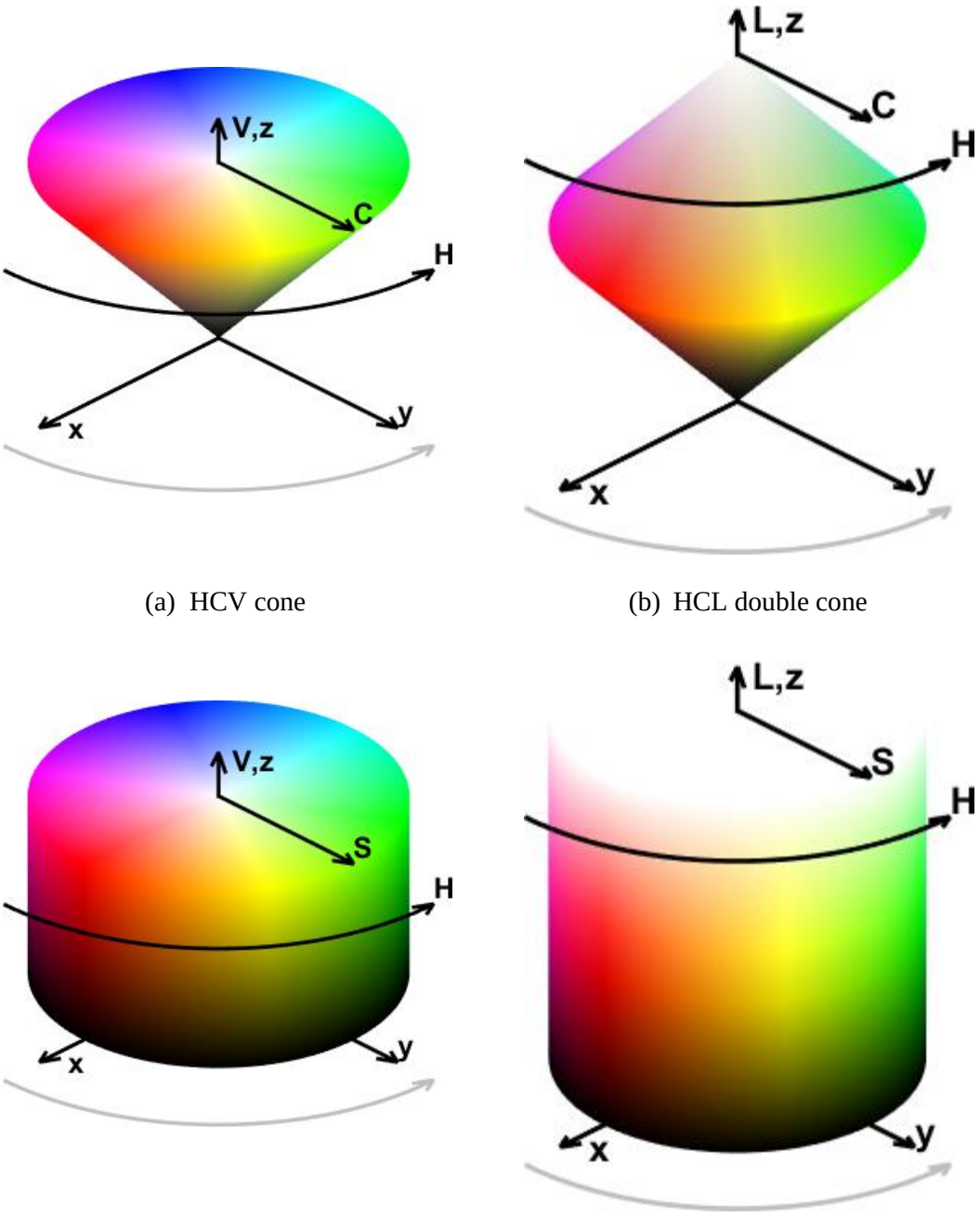

(a) HCV cone (b) HCL double cone

(c) HSV cylinder (d) HSL cylinder

Figure 12 Hue based colour models

2.5.3 YUV, YIQ, LUV and LAB

Other colour models include luminance based colour models such as YUV and YIQ [64], and the CIE colour models such as LUV and LAB [65], as shown in Fig. 13 and Fig. 14, respectively. The luminance based colour models are comprised of one luminance channel and two chrominance channels, this separates the image into greyscale and colour sets. While the CIE colour models consist of one lightness channel and two correlated chrominance channels of either cyan-red and blue-yellow (LUV) or green-red and blue-yellow (LAB).

The conversions from RGB to YUV and YIQ are given in (49) and (50), respectively.

$$\begin{bmatrix} Y \\ U \\ V \end{bmatrix} = \begin{bmatrix} 0.299 & 0.587 & 0.114 \\ -0.14713 & -0.28886 & 0.436 \\ 0.615 & -0.51499 & -0.10001 \end{bmatrix} \begin{bmatrix} r \\ g \\ b \end{bmatrix} \tag{49}$$

$$\begin{bmatrix} Y \\ I \\ Q \end{bmatrix} = \begin{bmatrix} 0.299 & 0.587 & 0.114 \\ 0.595716 & -0.274453 & -0.321263 \\ 0.211456 & -0.522591 & 0.311135 \end{bmatrix} \begin{bmatrix} r \\ g \\ b \end{bmatrix} \tag{50}$$

The inverse conversions from YUV and YUQ to RGB are given in (51) and (52), respectively.

$$\begin{bmatrix} r \\ g \\ b \end{bmatrix} = \begin{bmatrix} 1 & 0 & 1.13983 \\ 1 & -0.39465 & -0.5806 \\ 1 & 2.03211 & 0 \end{bmatrix} \begin{bmatrix} Y \\ U \\ V \end{bmatrix} \tag{51}$$

$$\begin{bmatrix} r \\ g \\ b \end{bmatrix} = \begin{bmatrix} 1 & 0.9563 & 0.621 \\ 1 & -0.2721 & -0.6474 \\ 1 & -1.107 & 1.7046 \end{bmatrix} \begin{bmatrix} Y \\ I \\ Q \end{bmatrix} \tag{52}$$

The conversions from RGB to LUV and LAB are given in (53) to (61).

$$\delta = \begin{cases} \begin{bmatrix} 1 & 0 & 0 \\ 0 & 1 & 0 \\ 0 & 0 & 1 \end{bmatrix}, & \text{LUV} \\ \begin{bmatrix} 1.052127 & 0 & 0 \\ 0 & 1 & 0 \\ 0 & 0 & 0.918481 \end{bmatrix}, & \text{LAB} \end{cases} \tag{53}$$

$$\begin{bmatrix}\alpha\\ \beta\\ \gamma\end{bmatrix} = \delta\begin{bmatrix}0.412453 & 0.35758 & 0.180423\\ 0.212671 & 0.71516 & 0.072169\\ 0.019334 & 0.119193 & 0.950227\end{bmatrix}\begin{bmatrix}R\\ G\\ B\end{bmatrix} \tag{54}$$

$$\varepsilon = \begin{cases}0, & \text{LUV}\\ 16, & \text{LAB}\end{cases} \tag{55}$$

$$L = \begin{cases}903.3\beta, & \beta \le 0.008856\\ 116\beta^{\frac{1}{3}} - \varepsilon, & \beta > 0.008856\end{cases} \tag{56}$$

$$U = 13L\left(\frac{4\alpha}{\alpha + 15\beta + 3\gamma} - 0.197939\right) \tag{57}$$

$$V = 13L\left(\frac{9\beta}{\alpha + 15\beta + 3\gamma} - 0.468311\right) \tag{58}$$

$$f(\epsilon) = \begin{cases}7.787\epsilon + 0.137931, & \epsilon \le 0.008856\\ \epsilon^{\frac{1}{3}}, & \epsilon > 0.008856\end{cases} \tag{59}$$

$$A = 500\big(f(\alpha) - f(\beta)\big) \tag{60}$$

$$B = 200\big(f(\beta) - f(\gamma)\big) \tag{61}$$

where *r*, *g* and *b* are the red, green and blue intensities, respectively, L is lightness, U, V and A, B are the two chrominance channels of LUV and LAB, respectively.

The inverse conversions from LAB and LUV to RGB are given in (62) to (67).

$$\beta = \begin{cases}\dfrac{L}{903.3}, & L \le 8\\ \left(\dfrac{L + \varepsilon}{116}\right)^3, & L > 8\end{cases} \tag{62}$$

$$F(\epsilon) = \begin{cases}\dfrac{\epsilon - 0.137931}{7.787}, & \epsilon \le 0.206893\\ \epsilon^3, & \epsilon > 0.206893\end{cases} \tag{63}$$

$$\alpha = \begin{cases}\dfrac{(9U + 23.158913L)\beta}{4V + 24.35217L}, & \text{LUV}\\ F\left(\dfrac{A}{500} + f(\beta)\right), & \text{LAB}\end{cases} \tag{64}$$

$$\gamma = \begin{cases}\dfrac{117\beta L}{3V + 18.264127L} - \dfrac{\alpha}{3} - 5\beta, & \text{LUV}\\ F\left(f(\beta) - \dfrac{B}{200}\right), & \text{LAB}\end{cases} \tag{65}$$

$$\delta = \begin{cases} \begin{bmatrix} 3.240481 & -1.537152 & -0.498536 \\ -0.969255 & 1.87599 & 0.041556 \\ 0.055647 & -0.204041 & 1.057311 \end{bmatrix}, & \text{LUV} \\ \begin{bmatrix} 3.079934 & -1.537152 & -0.542783 \\ -0.921234 & 1.87599 & 0.045244 \\ 0.05289 & -0.204041 & 1.151152 \end{bmatrix}, & \text{LAB} \end{cases} \tag{66}$$

$$\begin{bmatrix} r \\ g \\ b \end{bmatrix} = \delta \begin{bmatrix} \alpha \\ \beta \\ \gamma \end{bmatrix} \tag{67}$$

where *r*, *g* and *b* are the red, green and blue intensities, respectively, *L* is lightness, *U*, *V* and *A*, *B* are the two chrominance channels of LUV and LAB, respectively.

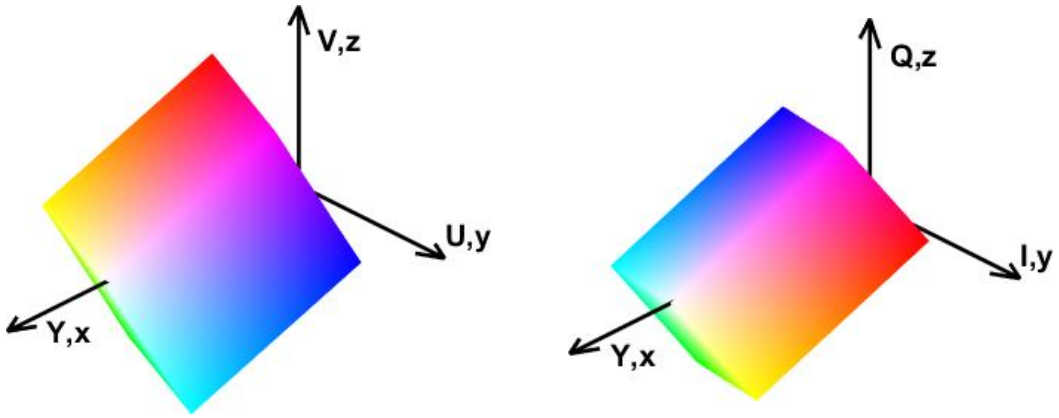

(a) YUV cuboid (b) YIQ cuboid

Figure 13 Luminance based colour models

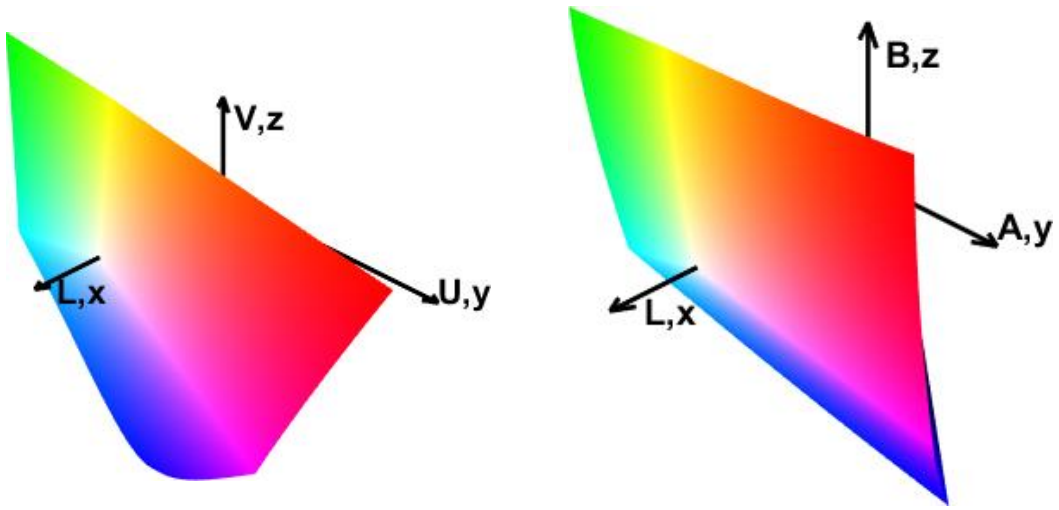

(a) LUV irregular gamut (b) Lab irregular gamut

Figure 14 CIE colour models

Luminance is regarded as the dominant channel as human perception is more sensitive to changes in overall light intensity (luminance) than differences among each colour channels (chrominance). This means that the bandwidth in the chrominance channels (U and V) can be reduced when necessary without significantly damaging the image quality, thus luminance based colour models are typically used for colour TV broadcasting.

On the other hand, the CIE colour models are designed to be perceptually uniform, they rely on a set of colour matching functions to resemble the responses of red, green and blue cones in human vision, thus CIE colour models can be regarded as the closest models to human perception. However, since the correlations are non-linear, the structure of these models is difficult to visualise and manipulate. More conversions from RGB can be found in the colour model survey paper [66].

2.6 Machine Learning

Machine learning has become a trending topic in computer science and computer vision in recent years due to its capability of solving complex tasks. Its applications can include gesture recognition [22], activity recognition [67], scene recognition [68], cancer classification [69], cyber security [70] and face recognition [71].

In general terms, the goal of machine learning is to enable a system to learn from the past or present and use that knowledge to make predictions or decisions regarding unknown future events [72]. In terms of image processing and data analysing, machine learning is about learning the related features associated with different classes without explicitly program these features. This is usually done through reinforced training with huge amount of data that contain positive and negative examples.

The concept of machine learning is not new, in fact, it has been used as early as 1950s, in which a computer has been successfully trained to play checkers competitively given only the rules of the game [73]. The revival of machine learning in recent years is primarily due to two reasons: the first major reason is the

advancements in hardware especially the Graphics Processing Unit (GPU) and the Tensor Processing Unit (TPU), while the second minor reason is due to the increased availability of many datasets that can now be accessed easily online.

GPU is originally designed for fast displaying of images, it has become the top choice for machine learning because when comparing to the Central Processing Unit (CPU), GPU is simply faster at computing multi-dimensional data such as images. This is due to the architecture differences between CPU and GPU, CPU is built with several powerful cores for sequential processing while GPU is built with thousands of tiny but efficient cores for parallel processing. TPU on the other hand is even faster than GPU, it consists of matrix multiplier unit designed specifically for matrix computations. However, currently TPU is extremely expensive to build due to its custom designed chips.

2.6.1 SVM

A well known and widely used method for analysing data through classification and regression is Support Vector Machine (SVM) [74]. SVM is a two-group classifier, the goal is to separate the training data into two classes with the largest possible difference between them. In a 2D linearly separable situation, this is equivalent of finding a line with the maximum possible margin, as given in (68).

$$f(x) = wx + b \tag{68}$$

where x is the training data, w is the normal vector, b is the bias.

Learning the SVM is then become an optimisation problem of finding the minimum value of $||w||^2$ that satisfies (69).

$$y(wx + b) \geq 1 \tag{69}$$

where x is the training data, w is the normal vector, b is the bias, y is the indicator to separate the data into two classes, in which y is equal to 1 for one class and -1 for the other class.

SVM is proven to be effective for most two-group classification problems. However, it can be unreliable when there are more than two classes, it also assumes that the inputs are linearly separable which is not always the case.

2.6.2 ANN

An advanced method is the Artificial Neural Network (ANN) [75]. ANN is inspired from the biological neural network in the brain, it typically consists of three types of layers: input, hidden and output, as shown in Fig. 15. Each layer is made of fully connected neurons, the numbers of neurons in the input and output layers are linked to the actual sizes of the input and output, respectively, while the number of layers and the number of neurons in each of the hidden layers are usually chosen arbitrarily depending on the difficulty of the task (typically 2 hidden layer with number of neurons between the sizes of input and output layers).

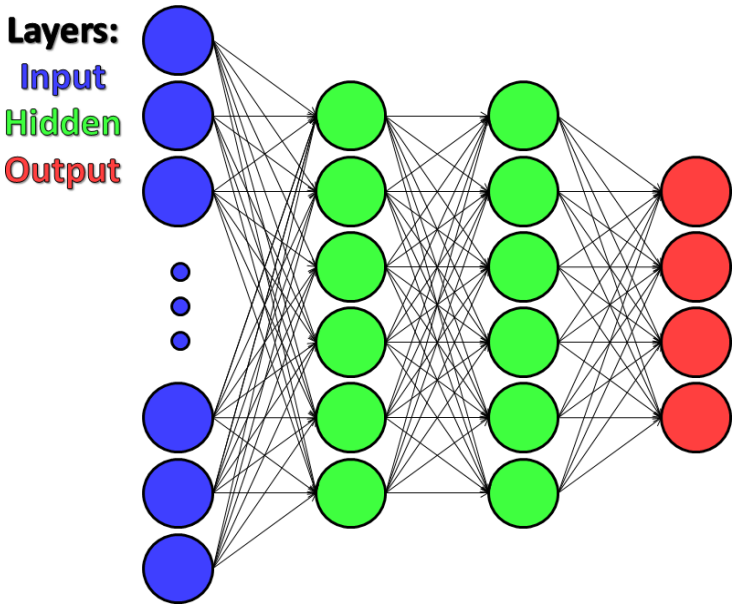

Figure 15 Example ANN setup: 1 input, 2 hidden and 1 output layers

For a typical object classification problem, the image itself can be regarded as the input layer, in which each neuron represents the intensity value of each pixel. While the results of classification can be regarded as the output layer, in which each neuron represents a separate class. For the two hidden layers, the output of the first layer can be thought of as the basic features such as edges belonging to the objects, while the output of the second layer can be thought of as the advanced features such as small parts belonging to the objects.

For each neuron, the network function can be defined as (70).

$$O = F(wI + b) \tag{70}$$

where I and O are the input and output of the neuron, respectively, w and b are the weight and bias in the neuron, respectively, F is the activation function (usually a rectifier that resets all negative outputs to zero).

For each iteration during the training of the network, the performance of the network is computed using a cost function. The most commonly used method is mean squared error, as given in (71).

$$E = \frac{1}{n}\sum_{i=1}^{n}(O_d - O_a)^2 \tag{71}$$

where O_d and O_a are the desired and actual output of the network, respectively, n is the number of training examples, E is the error (cost) of the network.

The learning or the training of the network can then be described as the process of finding the optimal weight w and bias b that minimising the error E. This is done through backpropagation via gradient descent, in which all w and b are readjusted based on the gradient of the cost function and learning rate, as given in (72).

$$\omega_{i+1} = \omega_i + \alpha\frac{dE}{d\omega_i} \tag{72}$$

where ω_i and ω_{i+1} are the original and adjusted parameters (weight or bias), respectively, α is the learning rate which controls the speed of the gradient descent, E is the error (cost) of the network.

2.6.3 CNN

An expansion of ANN is the Convolutional Neural Network (CNN) [76]. The learning process of CNN is known as deep learning because when compared to ANN, CNN employed a lot more layers and the neurons are considered as 3D blocks. Due to the added dimensions and layers, CNN tends to outperform ANN as the resolution of the image increases, but it requires even more computational power to train.

CNN typically consists of six types of layers: input, convolutional, activation, pooling, hidden and output, as shown in Fig. 16. Similar to ANN, the block size of the input layer is linked to the actual size of the input (i.e. for a 360×640 colour image, width is 360, height is 640 and depth is 3 since most images have 3 channels for RGB). The block size of the output layer is linked to the actual size of the output (i.e. number of groups for classification). While the numbers and block sizes of other layers are chosen arbitrarily.

For image related tasks such as face recognition, shallower layers can be thought of as the identification of low level features such as shapes and tones of the faces, while deeper layers can be thought of as the identification of high level features such as eyes and noses.

The mechanics of input, hidden and output layers are very similar to ANN described earlier. The purpose of the activation layer in CNN is basically the same as the activation function employed in (70). For the convolutional layer, instead of 1D convolutions, 3D convolutions are used (i.e. dot product with a 3D filter, typically a 3×3×3 block). While the function of the pooling layer is to regularise (avoiding over-fitting) and to reduce dimension by resizing the blocks into smaller ones (usually max pooling: save only the local maximum within each block).

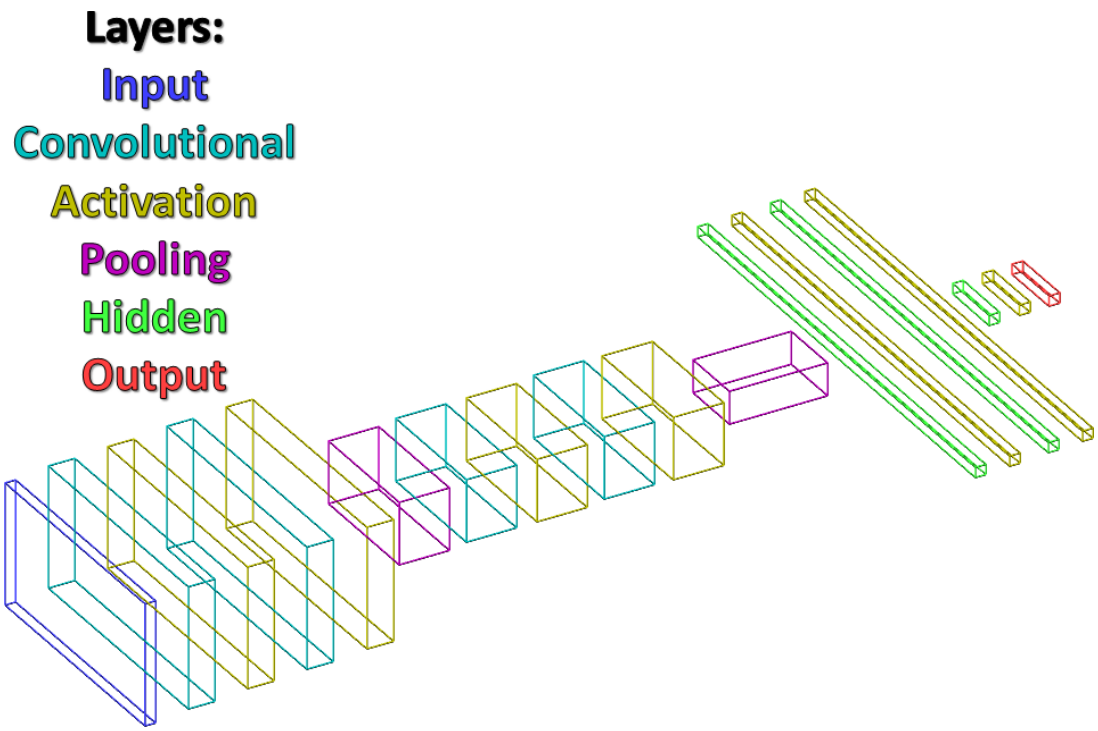

Figure 16 Example CNN setup: it contains 1 input, 4 convolutional, 7 activation, 2 pooling, 3 hidden and 1 output layers

Machine learning, especially CNN, is quickly becoming a new tool for solving many complex problems. However, it requires huge amount of samples for the network to learn adequately, the computational cost is also enormous and the training time can be long and highly unpredictable. Additionally, it is widely known that the results of the training can be sometimes puzzling, for example, when feeding a random generated image that doesn't look like anything into a trained network, it tends to response with a very confident output.

2.7 Human Detection

Human detection can be defined as a process of detecting the presence of human features from images or videos. Its applications are mainly found in the area of surveillance [77], these may include the recognition [78], following [79] and counting [80] of different people. The goal of human detection is to separate the human from the background in a given image or video by identifying common human-like features. As different people tend to have different features which are

caused by their variable appearances and postures, human detection can be a challenging task.

Generally, human detection methods can be divided into global based [81] and local based [82]. Global based methods treat the human object as a whole, while local based methods separate the human object into different body parts and treat them as individual units. In comparison, global based methods tend to yield more consistent results than the local based methods, but suffer from limited variations of viewpoints. On the other hand, local based methods tend to be more robust when dealing with different types of articulated body postures, but at the same time, their performances are heavily dependent on the detection accuracy of every body parts.

The most influential and widely known human detection method is the Histogram of Oriented Gradients (HOG) [81]. HOG is a feature descriptor that heavily relies on the extraction of gradient orientations and the use of linear SVM classifier.

The first step of the algorithm is the computation of the gradient values. Two simple kernels are used for extracting the gradient, as given in (73) and (74).

$$G_x = [-1 \quad 0 \quad 1] \tag{73}$$

$$G_y = \begin{bmatrix} -1 \\ 0 \\ 1 \end{bmatrix} \tag{74}$$

where G_x and G_y are the gradient filters along x (horizontal) and y (vertical) axes, respectively.

A dense grid of uniformly spaced cells is applied to divide the image into descriptor blocks, the blocks are typically arranged to overlap with their neighbours, this is done to allow multiple contributions from the same block. The magnitude and orientation of the blocks are then computed using (10) and (11), respectively. Orientation binning is performed to quantise the orientation values into 9 bins which are evenly spread cross 360 degrees. Weighted histograms are then created using these 9 channels with magnitude acting as the weighting factor.

The next step involves normalising the blocks, it is believed that normalisation introduces better invariance to illumination, shadow and edge contrast. HOG examined several different normalisation methods with insignificant difference in detection results, two commonly used methods are given in (75) and (76).

$$f = \frac{v}{\|v\|_1 + c} \tag{75}$$

$$f = \frac{v}{\sqrt{\|v\|_2^2 + c^2}} \tag{76}$$

where v is the unnormalised descriptor vector containing all histograms in a given block, c is a small constant used to avoid division by zero, $||v||_1$ is the L1 norm (Manhattan distance) while $||v||_2$ is the L2 norm (Euclidean distance).

The final step is the training phase, in which the descriptors are fed into a supervised learning system. Typically a linear SVM classifier (as discussed earlier in Section 2.6.1) is trained to distinguish humans between positive and negative images from a dataset (the original HOG method used about 2500 positive and 1250 negative images).

An example implementation of HOG with the original image and the detection results is provided in Fig. 17. The magnitude of the gradient is illustrated by the intensity of the lines (white is strong and grey is weak), while the orientation of the gradient is binned and is represented by the angle of these line. The final detected human ROI is indicated by the red rectangle.

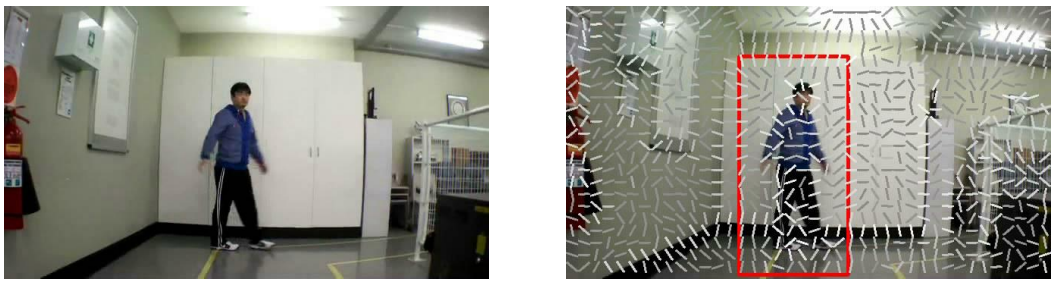

(a) Original (b) HOG

Figure 17 Example result of HOG

HOG is renowned for its human detection ability by utilising a large amount of training images. However, the accuracy of HOG is heavily influenced by the quality and quantity of these training images. This is because, in order to train a classifier successfully, it requires continuously recurring shape events in the given blocks of the training images [83]. HOG generally suffers from speed issues due to its energy intensive feature computations and the training itself can be a time consuming task. Many existing methods tend to design their approaches based on HOG or utilise it as an additional tool for their algorithms.

One method states that humans in standing positions tend to have distinguishing colour characteristics [84], therefore addition colour information can be utilised with HOG descriptors. This is done by extracting colour frequency and co-occurrence features in each channel of the converted HSV colour space. It also employed the partial least square regression analysis [85] onto the descriptors. These additional elements improved the accuracy of HOG, however at the same time the computational cost is also increased.

Another method utilises the omega shaped features of human heads [86]. This approach argues that the HOG feature based classifier is generally accurate but very slow to work with, while Haar feature based classifiers [87] are typically fast but prone to noises. Thus, it is believed greater robustness can be achieved by combining these two classifiers. This is done by employing Haar feature classifier to filter out obvious negative image patches and then rely on HOG for the detection using the remaining image patches. This approach greatly increased the computational speed with only a small drop in accuracy. However, only the head of a person is considered, the rest of the body are completely ignored.

Scale-Invariant Feature Transform (SIFT) can also be used for human detection [88]. SIFT [89] is an algorithm designed to detect and describe local features by extracting distinctive invariant features. SIFT descriptors are similar to HOG in the sense that both descriptors utilise gradient features. The difference is that HOG is computed in dense grids while SIFT is computed in sparse grids with orientation alignment. By combining HOG and SIFT descriptors, higher detection rate can be achieved.

However, the robustness of these methods tends to suffer significantly with online processing, since both descriptors require reasonably high computational cost.

You Only Look Once (YOLO) is a general purpose object detector which can be tuned for human detection [90]. By converting the detection problem to a fixed grid regression problem, YOLO is able to minimise the computational cost required during run-time. This is done by dividing the image into sparse grids in which each grid detects only one object. A 24-layered CNN network is employed for the detection, the first 20 layers are employed for pre-training purposes, the detection layers are followed by 2 fully connected layers, while an average pooling and a single fully connected layers are attached to the end of training layers. Because of its fast detection speed, YOLO is regarded as a real-time detector, however the precision level of the detection results tends to be low, this is mostly due to its fixed grid nature.

2.8 Object Tracking

In computer vision, object tracking is about keeping track of the position of the target object on the image continuously through a period of time. This may seem like a straightforward task, but it remains a challenging problem due to several complications such as occlusion, out of view, illumination, shadow, motion blur and change of viewpoint [91]. Its applications can include surveillance [92], mapping [93], medical imaging [94], automated manufacturing [95], gesture [22] and behaviour recognitions [96].

Object tracking methods can be generally divided into two groups: learning based and non-learning based. Learning based methods focus on the training of feature classifiers to distinguish between the foreground object and the background noise, while non-learning based methods usually concerned with the tracking of specific features using pre-determined parameters. Learning based methods tend to be relatively more resistant against background interference but require large pools of training samples that contain relevant features to achieve satisfactory results. On the

contrary, non-learning based methods do not require any training, their results may be prone to noise.

Learning based methods have gained traction in recent years mostly due to the advancements in hardware, as the training and simulation time have been reduced significantly compared to a decade ago. One of the well known methods in this topic is Tracking-Learning-Detection (TLD) [97]. TLD proposes that the object tracking task can be decomposed into three components: tracking, learning and detection. These components work independently of each other as median flow is used to track objects between frames, detection in a single frame is done based on template matching and nearest neighbour classifier, growing and pruning are achieved through learning of false positive and negative errors. Another widely known method is Online AdaBoost Tracking (OAB) [98]. OAB allows feature updates during tracking by utilising fast computable features such as Haar-like wavelets, orientation histograms and local binary patterns. It also employs two types of classifiers: weak classifier that corresponds to a single feature and strong classifier that represents a set of weak classifiers. Local Sparse Appearance Model and K-selection based Tracking (LSK) [99] is a method focus on the learning of the target appearance. LSK relies on a static sparse dictionary and a dynamic basis distribution to limit the drifting of the tracking. The object appearance is also modelled using a sparse coding histogram based on a learned dictionary that improved detection.

Non-learning based methods tend to work with specific features. An example of such methods is Kernel based Tracking (KNL) [100]. KNL regularises the feature histogram based object representation by using spatial masking with an isotropic kernel. It employs mean shift to perform gradient based optimisation with metrics derived from the Bhattacharyya coefficient acting as the similarity measurement. Fragment based Tracking (FRG) [101] is another method, it is based on histogram tracking. For each frame, FRG introduces arbitrary patches to vote on possible positions and scales of the object, the voting is performed by comparing intensity and colour histogram with the corresponding patch. The vote maps are then combined using the minimum sum method. Locality Sensitive Histogram based Tracking (LSH) [102] also relies on histogram for tracking. However, unlike the conventional

histogram, LSH computes a weighted histogram at each pixel location with distance as the weight, such that boundary pixels have minimum impact to the corresponding histogram bin values. It also introduces a method of extracting illumination invariant features.

Examples of the results using object tracking methods described earlier are presented in Fig. 18. In the figure, the input image with original ROI and the test image with detected ROIs using different methods are given in (a) and (b), respectively. The original ROI and the detected ROIs are also provided separately, as shown in (c) to (i). The size of these ROIs is increased by a factor for visualisation and comparison purposes, their actual sizes are illustrated by the different rectangular ROIs in (a) and (b).

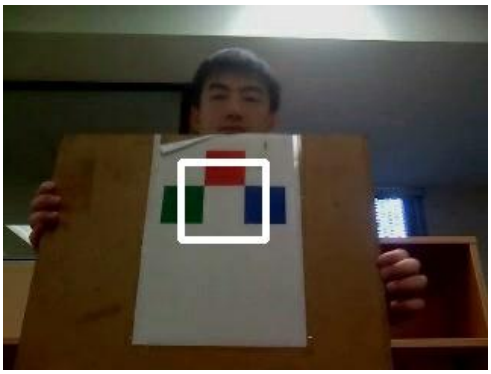

(a) Input image with original ROI

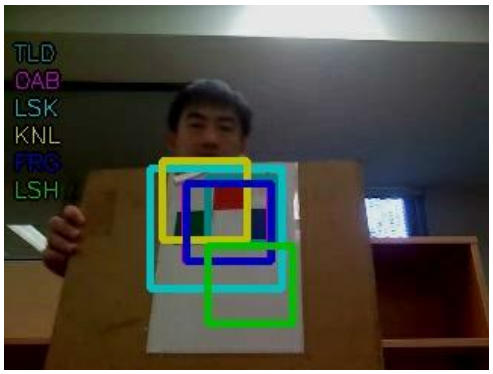

(b) Test image with detected ROIs

(c) Original

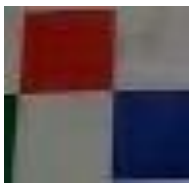

(d) TLD

(e) OAB

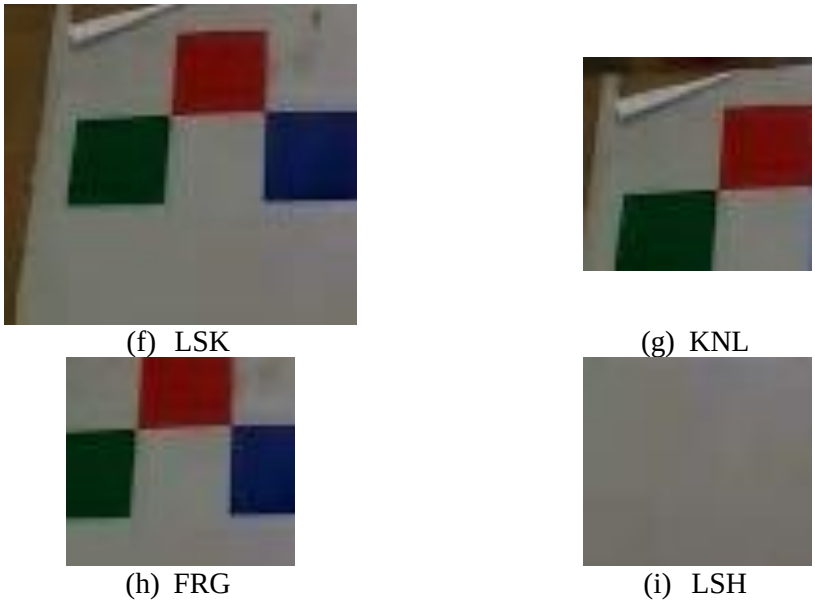

(f) LSK (g) KNL

(h) FRG (i) LSH

Figure 18 Example results of object tracking

2.9 Target Pursuit Using UAV

Although UAV is initially designed for military purposes which can be traced back to as early as the World War I [103], nowadays, UAV is mainly used for photogrammetric applications such as surveillance and remote sensing. In recent times, there is an evidenced increase in popularity of using UAV for various applications such as target pursuit, this is because when compared to manned systems, UAV is cheaper, faster and safer [104]. Additionally, most UAVs tend to be small since there is no need for human pilots onboard. This allows them to operate in tight spaces and rather close to the object, thus acquiring more images with higher quality. Another important reason of the increased demand can be explained by the spreading of low cost GPS and INS combined systems. The combination of GPS and INS is known to provide reliable velocity and position estimations, which are necessary for high precision navigations [105].

Among the applications of UAV, vision based target pursuit is a challenging and complex problem, this is because it consists of many sub-problems which are typically concerned with the detection, tracking and following of the object of interest. Other issues such as localisation, path planning, obstacle avoidance and

multi-robot cooperation can also be considered which further increase the difficulty. Until recent years, there are very few practical approaches related to this to topic [6–10], as the majority of the related existing methods are developed using computer simulation with the assumption of ideal environmental factors [1–5]. This is mostly due to advancements in both hardware and software of small UAVs such as quadrotors during the past decade. Among the few methods developed, one method approached the pursuit problem by focusing on tracking the colour of the target [6], this is done by employing a colour based probabilistic tracking scheme based on Camshift [106]. This method is experimented with the tracking of a balloon using a drone at close range. Another method [7] working on the tracking of the entire body of a standing person also chose Camshift. This approach relied on Camshift to detect candidate ROIs, the most suitable ROI is then determined by comparing the corresponding sizes and histogram. Kalman filter [107] is employed for the localisation of both the drone and target person with respect to a common reference frame. Other approaches, such as the one presented in [8] employed TLD [97] to track a human target. This is done by tracking gradient based and greyscale intensity features belonging to the torso of a person, the drone is then programmed to follow the person.

While most methods relied on front facing cameras for tracking the target, downward facing ones can also be used. An example is this implementation [9], in which a drone is programmed to pursuit a remotely controlled toy car using a downward pointing camera. It employs a colour tracking approach based on the particle filter [108] with considerations of noise and occlusion. A similar experiment is performed with a moving landing platform [10]. This is done by tracking the platform using rectangle detection and optical flow [54]. The position of the platform is computed based on centroid of image moments.

Based on the results provided in these practical methods, such as the example tracking frames shown in Fig. 19, it can be seen that the methods are able to track their designed targets within their test environments. However, their targets tend to be simple objects that contain monochromatic colours with very little texture variances, these targets also appear highly salient when compared to the

surroundings. Therefore, it is evident that current research in this topic is lacking of reliable approaches.

(a) Tracking a red balloon using a front facing camera [6]

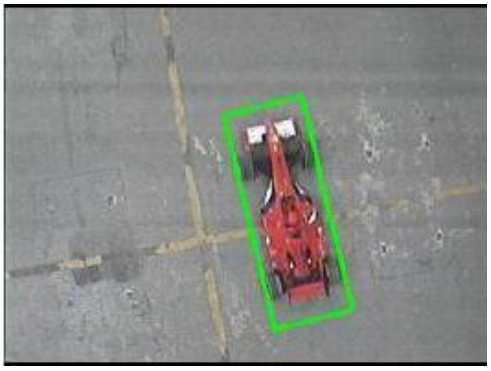

(b) Tracking a red toy car using a downward facing camera [9]

Figure 19 Example tracking frames of existing practical approaches

2.10 Motion Control of Quadrotor

Among the different types of UAVs, quadrotor has gained the most attention. One of the reasons behind this is because the architecture of the quadrotor, as it is a simple rotorcraft that does not rely on complicated swash plates and linkages found in conventional rotorcraft [109]. Another reason is because of its enhanced payload capacity and manoeuvrability due to its unique configuration [110].

A quadrotor is an under actuated dynamic system with four input forces (four fixed rotors with two pairs turn in opposite direction) and six output coordinates (fully spatial movements that consists of pitch, roll, yaw, heave, surge and sway). These movements can be visualised using Fig. 20, where the red, green and blue axes represent positive movements of heave, surge and sway, respectively, the rotation around each of the red, green and blue axes represent yaw, roll and pitch, respectively (right hand rule, anti-clockwise is positive).

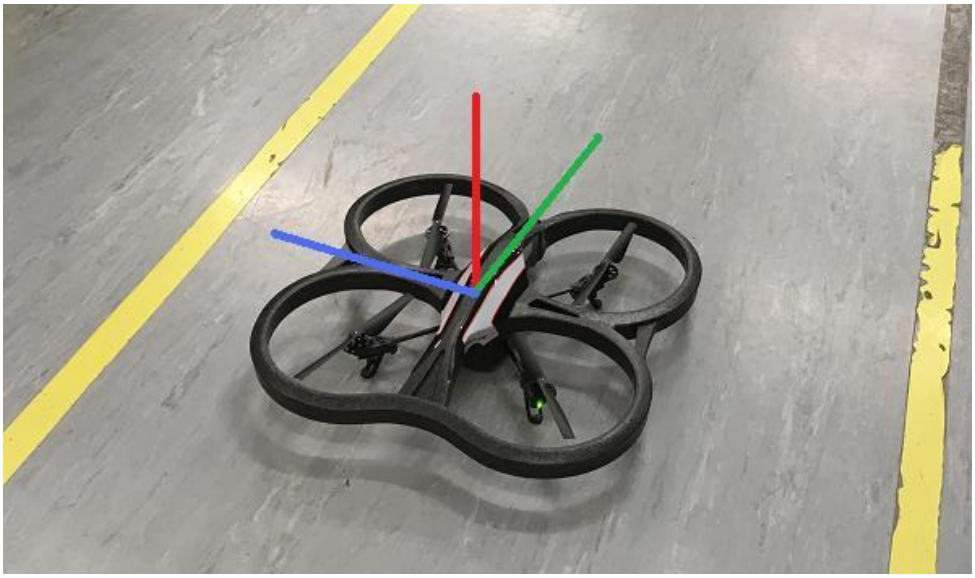

Figure 20 Spatial movements of a quadrotor: pitch, roll, yaw, heave, surge and sway

Since one pair of opposite propellers rotates in clockwise direction while the other pair rotates in anti-clockwise direction, this causes the net aerodynamic torque to be exactly zero, thus eliminates the need of a yaw stabilising rotor found in conventional helicopters. Typical rotor configuration of quadrotor with its rotation directions is given in Fig. 21, where *C* and *A* represent clockwise and anti-clockwise rotations, respectively.

Figure 21 Typical rotor configuration of quadrotor

Various motions of quadrotor can be produced by controlling the individual rotor speeds of all four motors, as given in Fig. 22, where + and – represent increasing and

decreasing rotor speeds, respectively, *O* represents equilibrium rotor speed that keeps the quadrotor stable when hovering (thrust equals to weight, i.e. $4 \times O$ causes the quadrotor to hover over a fixed point). Pitch, roll and yaw rotations are achieved by creating speed variations between different pairs of propellers: pitch is affected by front and back pairs, roll is affected by left and right pairs, yaw is affected by diagonal pairs. Heave translation is achieved by varying the speed of all propellers evenly, while surge and sway translations are achieved by maintaining non-zero pitch and roll angles, respectively.

(a) Hover

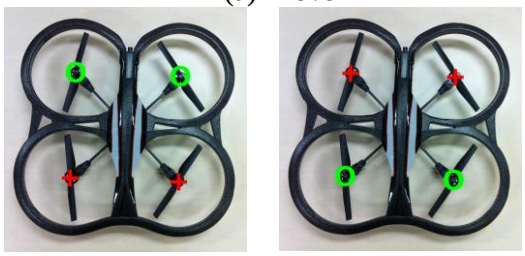

(b) Surge

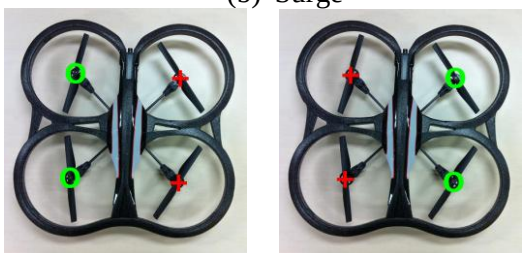

(c) Sway

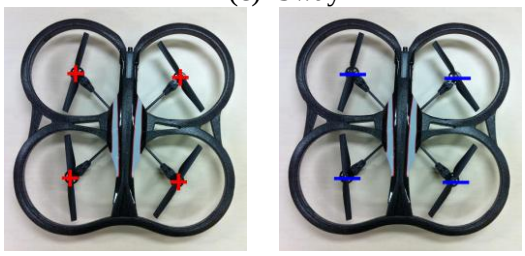

(d) Heave

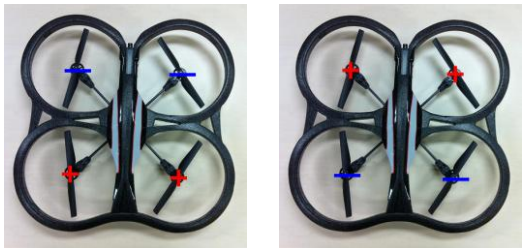

(e) Pitch

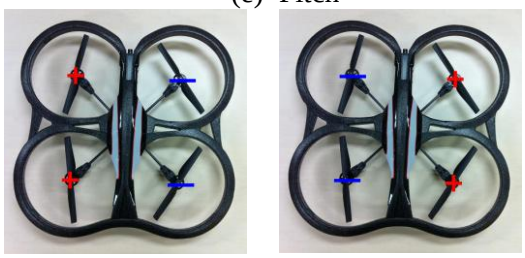

(f) Roll

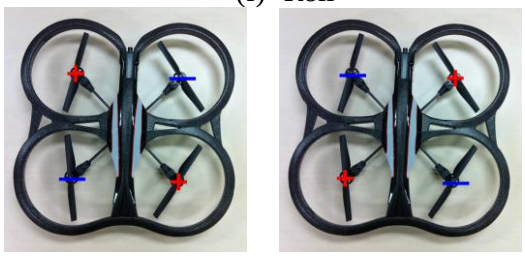

(g) Yaw

Figure 22 The motion control of quadrotor

In summary, employing UAVs for various applications has gained traction in recent years. Among the applications, vision based target pursuit is a challenging task, this is because it consists of many sub-problems which are typically concerned with the detection, tracking and following of the object of interest. This chapter reviews related topics including computer vision, various features, colour model, machine learning, human detection and object tracking. Existing methods in target pursuit and motion control of quadrotor have also been discussed. At present, the majority of related existing methods are developed using computer simulation with the assumption of ideal environmental factors, while the remaining few practical methods are mainly developed to track and follow simple objects that contain monochromatic colours with very little texture variances. It can be seen that current research in this topic is lacking of practical vision based approaches. Thus this research is aimed to fill the gap by developing a real-time algorithm capable of following a person continuously given only a photo input.

Chapter 3 Proposed Methods in Colour Based Feature Detection

This chapter proposes three methods in colour based feature detection. Section 3.1 introduces a colour enhancement method for colour segmentation. Section 3.2 discusses a colour identification method and Section 3.3 details the concept of a colour model for improved colour detection. The contents of this chapter are based on revised versions of author's publications resulting from this research [111–113]. These publications can also be found in the list of publications in Section 1.4.

3.1 A Colour Enhancement Method for Colour Segmentation

Existing colour segmentation methods tend to be designed for a specific colour space, they also tend to focus on the segmentation stage alone and employ little to none for pre-processing. In this section, a colour enhancement method that is capable of improving the results of colour segmentation is presented. The proposed colour enhancement method is named Chroma based Colour Enhancement (CCE), chroma can be defined as the colourfulness property relative to brightness, the goal of the enhancement is to boost the colour saliency of critical regions and to improve the consistency of segmentation results by maximizing chroma while preserving the hue angle. The enhancement procedure is efficient and easy to implement as it is designed to operate on raw RGB inputs and only requires one pass of the original image for filtering.

The proposed CCE method starts by finding the optimal threshold for colour enhancement. This is determined according to the colourfulness of the given image based on the mean chroma level. Critical colour regions of the image are then enhanced by maximizing the chroma while preserving the hue angle, this is done by

filtering through all three channels of the raw RGB inputs using the determined threshold. The detailed approach is described below.

Chroma is calculated based on common knowledge using (77) to (79). Mean chroma level can be interpreted as an indicator of the colourfulness of the image and is computed using (80). The optimal threshold is then obtained based on the mean chroma level using (81).

$$U_i = \min(r_i, g_i, b_i) \tag{77}$$

$$V_i = \max(r_i, g_i, b_i) \tag{78}$$

$$C_i = V_i - U_i \tag{79}$$

$$\bar{C} = \frac{1}{n}\sum_{i}^{n} C_i \tag{80}$$

$$C_T = \max\left(\frac{1}{8}, \frac{1}{4} - \bar{C}\right) \tag{81}$$

where i represents individual pixel, r, g, b are the red, green and blue intensity values, U and V are the minimum and maximum intensity values, respectively, n is the total number of pixels in the image, C is chroma, $\bar{C}$ is the mean chroma level and C_T is the optimal threshold for colour enhancement. C_T is employed to differentiate grey from ordinary colours. A colourful image tends to have less grey pixels than a colourless one, therefore threshold decreases when the mean chroma level increases and vise versa. The limits of C_T are determined empirically based on mean chroma level of typical photos (which tend to be medium to low levels).

Once the optimal threshold is determined, all three RGB channels of the image are filtered, in which the chroma level of every pixel is checked against the threshold. If its chroma level is greater or equal to the threshold, the pixel is assigned to the critical colour regions and colour enhancement is applied by maximising chroma while preserving the hue angle. Otherwise it is regarded as noise and the colour content of the pixel will be removed by converting it to greyscale.

The filtered RGB intensity values are obtained from the colour enhancement using (82) to (85).

$$I_i = \frac{r_i + g_i + b_i}{3} \tag{82}$$

$$R_i = \begin{cases} I_i, & C_i < C_T \\ 1, & C_i \geq C_T \text{ and } r_i = V_i \\ 0, & C_i \geq C_T \text{ and } r_i = U_i \\ \dfrac{r_i - U_i}{|g_i - b_i|}, & \text{otherwise} \end{cases} \tag{83}$$

$$G_i = \begin{cases} I_i, & C_i < C_T \\ 1, & C_i \geq C_T \text{ and } g_i = V_i \\ 0, & C_i \geq C_T \text{ and } g_i = U_i \\ \dfrac{g_i - U_i}{|r_i - b_i|}, & \text{otherwise} \end{cases} \tag{84}$$

$$B_i = \begin{cases} I_i, & C_i < C_T \\ 1, & C_i \geq C_T \text{ and } b_i = V_i \\ 0, & C_i \geq C_T \text{ and } b_i = U_i \\ \dfrac{b_i - U_i}{|r_i - g_i|}, & \text{otherwise} \end{cases} \tag{85}$$

where *i* represents individual pixel, *r*, *g*, *b* are the red, green and blue intensity values, *I* is the mean intensity, *U* and *V* are the minimum and maximum intensity values, respectively, *C* and C_T are the chroma level and the optimal threshold, respectively, *R*, *G* and *B* are the filtered red, green and blue intensity values after the colour enhancement process.

The result of the filtering is that pixels with dissimilar intensity values between the channels of RGB appear more salient than pixels with similar values, this allows the colours within the image to be much easier to identify and segment. Geometrically speaking, if a pixel lies closest to a particular colour, it is much harder for a colour segmentation method to associate it to another colour. Therefore, it is decided to use the Euclidean distance to examine the effectiveness of the proposed colour enhancement method by segmenting the images into different colour regions according to the nearest neighbour criterion. The number of colour regions can be pre-defined or determined automatically. In this experiment, it is decided to employ 8-colour system described in Section 2.3 for simplicity, the colours are white, black, blue, green, red, cyan, yellow and magenta.

To fully present the effectiveness of the proposed colour enhancement method, the proposed approach is compared with one of the traditional contrast based approaches [114] (referred to as traditional contrast enhancement or TCE). The original image, and the enhanced images using TCE and the proposed CCE methods are shown in Fig. 23, while the results of colour segmentation in RGB colour space using these three type of images are provided in Fig. 24. The original images are collected from various sources and have different sizes, intensity and quality, from the top to the bottom: the first three images are captured by the front facing camera of the quadrotor used in this research, the next two images are obtained from the INRIA person dataset and the rest are randomly selected from Google images.

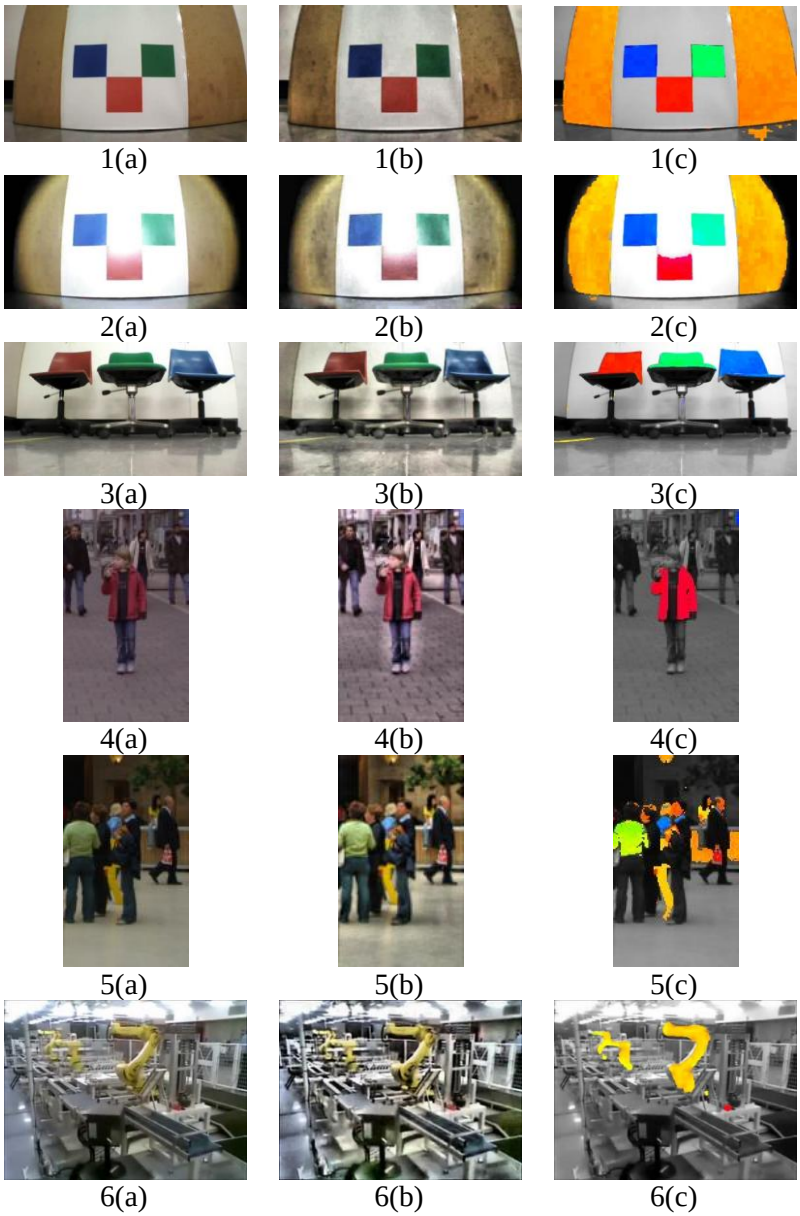

1(a) 1(b) 1(c)
2(a) 2(b) 2(c)
3(a) 3(b) 3(c)
4(a) 4(b) 4(c)
5(a) 5(b) 5(c)
6(a) 6(b) 6(c)

Figure 23 Original and enhanced images using TCE and CCE

*Original images (based on case number):
3 to 5: *http://pascal.inrialpes.fr/data/human*
6: *https://www.youtube.com/watch?v=woag8p2aEaE*
7: *http://geekongadgets.com/wp-content/uploads/2014/06/702325779.jpg*
8: *https://dirghakala.files.wordpress.com/2012/11/obama.jpg*
9: *https://exampundit.in/wp-content/uploads/2014/08/IBPSFIFANOTES.jpg*
10: *http://i.dailymail.co.uk/i/pix/2015/01/15/24BCA07300000578-2912489-image-a-25_1421364595463.jpg*
11: *http://www.maxtheknife.com/marshax3/marsha36.jpg*
12: *https://www.sneakerfiles.com/wp-content/uploads/2009/04/nike-terminator-low-pink-blue-turquoise-purple-4.jpg*


1(a)


1(b)


1(c)


2(a)


2(b)

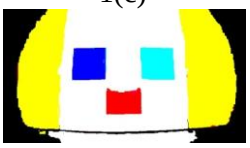
2(c)


3(a)


3(b)


3(c)


4(a)


4(b)


4(c)


5(a)


5(b)


5(c)


6(a)


6(b)


6(c)


7(a)


7(b)

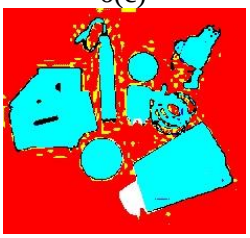
7(c)


8(a)


8(b)


8(c)

9(a)

9(b)

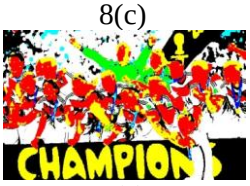

9(c)

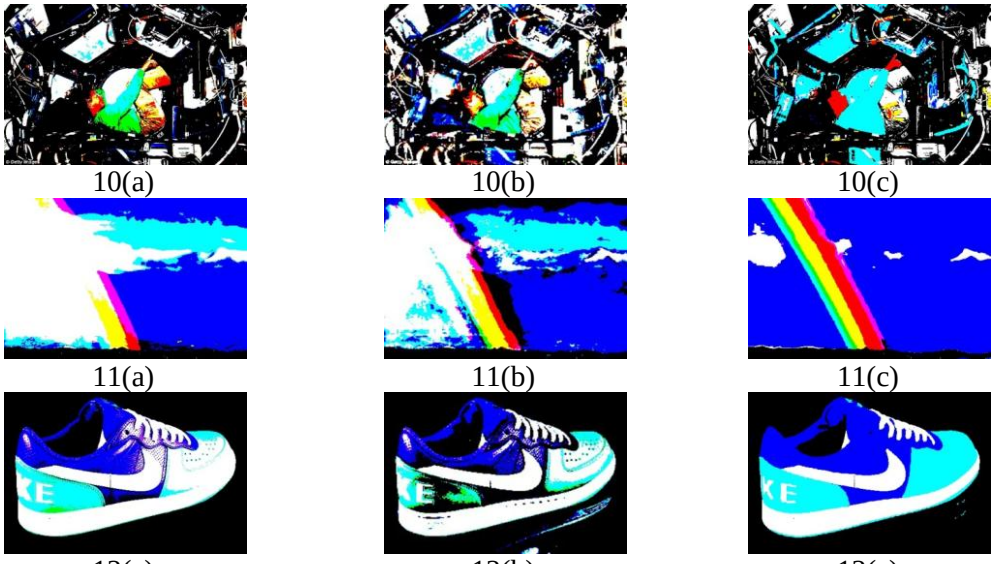

10(a) 10(b) 10(c)

11(a) 11(b) 11(c)

12(a) 12(b) 12(c)

(a) Segmentation using original (b) Segmentation using TCE (c) Segmentation using CCE

Figure 24 Colour segmentation using the original image, and the enhanced images using TCE and CCE

As illustrated in the figures, it can be unreliable to identify and segment the colours using images without any enhancement. Images enhanced with TCE method performed slightly better, but clearly not as good as the proposed CCE method. This can be obvious for many of the cases, for example, in case 1 of Fig. 24, the correct colours of all three squares are identified with the image enhanced using the proposed CCE method while others failed. These results indicate the high effectiveness of the proposed CCE method as the colours are segmented accurately and consistently under different lighting conditions with various image qualities.

3.2 A Colour Identification Method

Most of the existing colour identification methods are limited to their applications and are designed with the assumption that images with sufficient intensity and quality levels are provided. In this section, a colour identification method that is capable of identifying the required colour effectively from images with varying lighting condition and qualities is presented. This is done by extracting the desired

colour through adaptively determining the thresholds and the colour space that produce the best outcome.

The proposed colour identification method is named Adaptive Multi-channel Thresholding (AMT), it consists of three stages: image analysis, colour space selection and adaptive filtering. The proposed AMT method firstly analyses the image by collecting a variety of information, this is employed to determine the key properties of the image. The colour space selection scheme is then applied to find the most suitable hue based colour space by using the key properties obtained earlier. Finally, to extract the target colour, the image is filtered through all the channels of the selected colour space. The detailed approach is described below.

The first stage is image analysis, in which key properties of the image are determined. The obtained image properties include: value, chroma, lightness, saturation, hue, entropy (of hue), mean intensity and its standard deviation (of the foreground, the background and the entire image). The equations for value, chroma, lightness, saturation and hue are described earlier in Section 2.5, mean intensity is determined using (86) and (87), standard deviation and entropy are calculated based on common knowledge using (88) and (89), respectively.

$$I_i = \frac{r_i + g_i + b_i}{3} \tag{86}$$

$$\bar{I} = \frac{1}{n}\sum_{i}^{n} I_i \tag{87}$$

$$\sigma = \sqrt{\frac{1}{n}\sum_{i}^{n}(I_i - \bar{I})^2} \tag{88}$$

$$E = -\frac{1}{n}\sum_{i}^{n} H_i \, log_2 \frac{H_i}{n} \tag{89}$$

where i represents individual pixel, r, g, b are the red, green and blue intensities, respectively, n is the total number of pixels in the image, H is the hue, I and $\bar{I}$ are the

mean intensity of the pixel and the entire image, respectively, σ and E are the standard deviation and the entropy, respectively.

Additionally, the pixels are roughly classified into foreground and background through a simple hue filtering procedure, as given in (90).

$$\alpha = \begin{cases} 1, & \min(|H - H_d|, 360° - |H - H_d|) \leq 30° \\ 0, & \min(|H - H_d|, 360° - |H - H_d|) > 30° \end{cases} \quad (90)$$

where α is the class identifier in which 1 and 0 represent foreground and background, respectively, H and H_d are the actual and desired hue values, respectively. The desired value can be determined based on a pre-defined colour or it can be obtained automatically from a ROI. The absolute difference threshold is selected empirically as the shifting of hue due to lighting condition is common to occur but unlikely to be more than 30 °.

By finding these properties, the main characteristic of the image can be determined. For example, an image with low entropy and standard deviation levels tends to indicate the colour consistency is high and the image quality is low.

The second stage is the colour space selection, in which the most suitable colour space is selected based on properties obtained through image analysis. Generally, in hue based colour models there are four commonly used colour spaces: HSV, HSL, HCV and HCL. The selection of these colour spaces is important because each colour space has its own measures of colour purity and brightness under different lighting conditions. The key in the selection is to differentiate between the lightness with the value in the colour brightness channel, and between the chroma with the saturation in the colour purity channel.

When the foreground has a wider spread of intensity than the background, it can be said that the foreground has a higher variance in the brightness channel than the background. Therefore both the maximum and minimum values of the RGB should be considered and hence L is selected to represent the brightness of the image,

otherwise, only the maximum value is considered and hence V is selected, as given in (91).

$$B = \begin{cases} L, & \sigma^+ \geq \sigma^- \\ V, & \sigma^+ < \sigma^- \end{cases} \tag{91}$$

where B represents the colour brightness channel, L and V represent lightness and value channels, respectively, the superscripts + and – represent the foreground and background, respectively, σ is the standard deviation of the intensity.

It is found that saturation is more suited under illumination effect while chroma performed better under the influence of shadow. When the mean intensity level is closer to the maximum than the minimum with respect to standard deviation, it can be said that the image is more likely to be under the influence of illumination than shadow, as given in (92).

$$P = \begin{cases} S, & \min\left(\frac{\bar{I}^+}{\sigma^+}, \frac{\bar{I}^-}{\sigma^-}\right) \geq \min\left(\frac{1-\bar{I}^+}{\sigma^+}, \frac{1-\bar{I}^-}{\sigma^-}\right) \\ C, & \min\left(\frac{\bar{I}^+}{\sigma^+}, \frac{\bar{I}^-}{\sigma^-}\right) < \min\left(\frac{1-\bar{I}^+}{\sigma^+}, \frac{1-\bar{I}^-}{\sigma^-}\right) \end{cases} \tag{92}$$

where P represents the colour purity channel, S and C represent saturation and chroma channels, respectively, the superscripts + and – represent the foreground and background, respectively, $\bar{I}$ and σ are the mean and standard deviation of the intensity, respectively.

The third and final stage is the adaptive filtering, in which the original hue channel and the selected colour purity and brightness channels that were determined earlier are filtered based on two sets of limits: upper and lower limits.

The hue limits are determined based on the colour entropy of the image and the number of foreground pixels found in (93). It is noticed that an image with high entropy level and large foreground area tends to require a small hue tolerance for filtering, as given in (94).

$$H_1 = H_d - \left(1 - \frac{E}{\log_2 360°}\sqrt{\frac{n^+}{n}}\right)30° \tag{93}$$

$$H_2 = H_d + \left(1 - \frac{E}{\log_2 360°}\sqrt{\frac{n^+}{n}}\right)30° \tag{94}$$

where H_1 and H_2 are the lower and upper hue limits, respectively, n^+ and n are the numbers of foreground and total pixels in the image, respectively, H_d is the desired hue value, E is the entropy. Note: $\log_2 360°$ is the maximum entropy and $30°$ is the absolute difference threshold used in (90).

The brightness limits are computed based on foreground intensity, background intensity and standard deviation of intensity. An image with low background and foreground intensities but large standard deviation tends to favour a small brightness tolerance for filtering, as given in (95) and (96).

$$B_1 = \max\left(B_T, \min\left(\frac{\bar{I}^+ + \bar{I}^-}{2} - \sigma, \sigma\right)\right) \tag{95}$$

$$B_2 = \min\left(1 - B_T, \max\left(\frac{\bar{I}^+ + \bar{I}^-}{2} + \sigma, 1 - \sigma\right)\right) \tag{96}$$

where B_1 and B_2 are the lower and upper brightness limits, respectively, the superscripts + and – represent the foreground and background, respectively, $\bar{I}$ and σ are the mean and standard deviation of the intensity, respectively. As colour regions located next to absolute white (maximum) and absolute black (minimum) are difficult to differentiate, a brightness threshold B_T of 1% is applied to each of the limits to filter out those regions.

The purity limits are obtained based on the brightness limits. However, the upper limit is adjusted to the maximum, this is done because colour purity is a reliable measure of the strength of the colours presented in the image, as given in (97) and (98).

$$P_1 = B_1 \tag{97}$$

$$P_2 = 1 \tag{98}$$

where P_1 and P_2 are the lower and upper purity limits, respectively, B_1 is the lower brightness limit.

Based on these selections, the required colour can then be obtained through multi-channel filtering. To fully present the effectiveness of the proposed AMT method, the method is firstly examined with the detection of red square in the five benchmark images, as shown in Fig. 25.

These five images are captured by the front facing camera of the quadrotor used in this research under very different lighting conditions, from the top to the bottom: the first image is captured under normal lighting conditions, the next two images are captured under shadow effects and the last two images are capture under illumination effects. In the figure, the original benchmark images are shown in (a), results using the simple hue filter are given in (b), results using AMT (without adaptive colour space selection) in HCV, HCL, HSV and HSL are provided in (c) to (f), respectively, results using AMT with adaptive colour space selection are presented in (g).

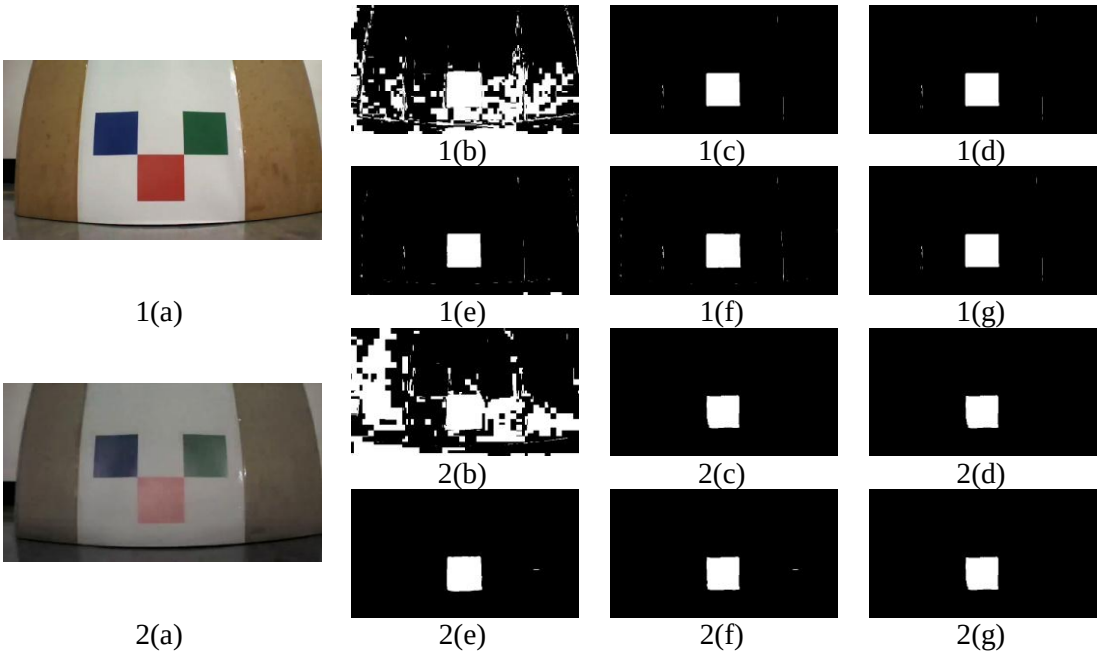

1(a) 1(b) 1(c) 1(d)

1(e) 1(f) 1(g)

2(a) 2(b) 2(c) 2(d)

2(e) 2(f) 2(g)

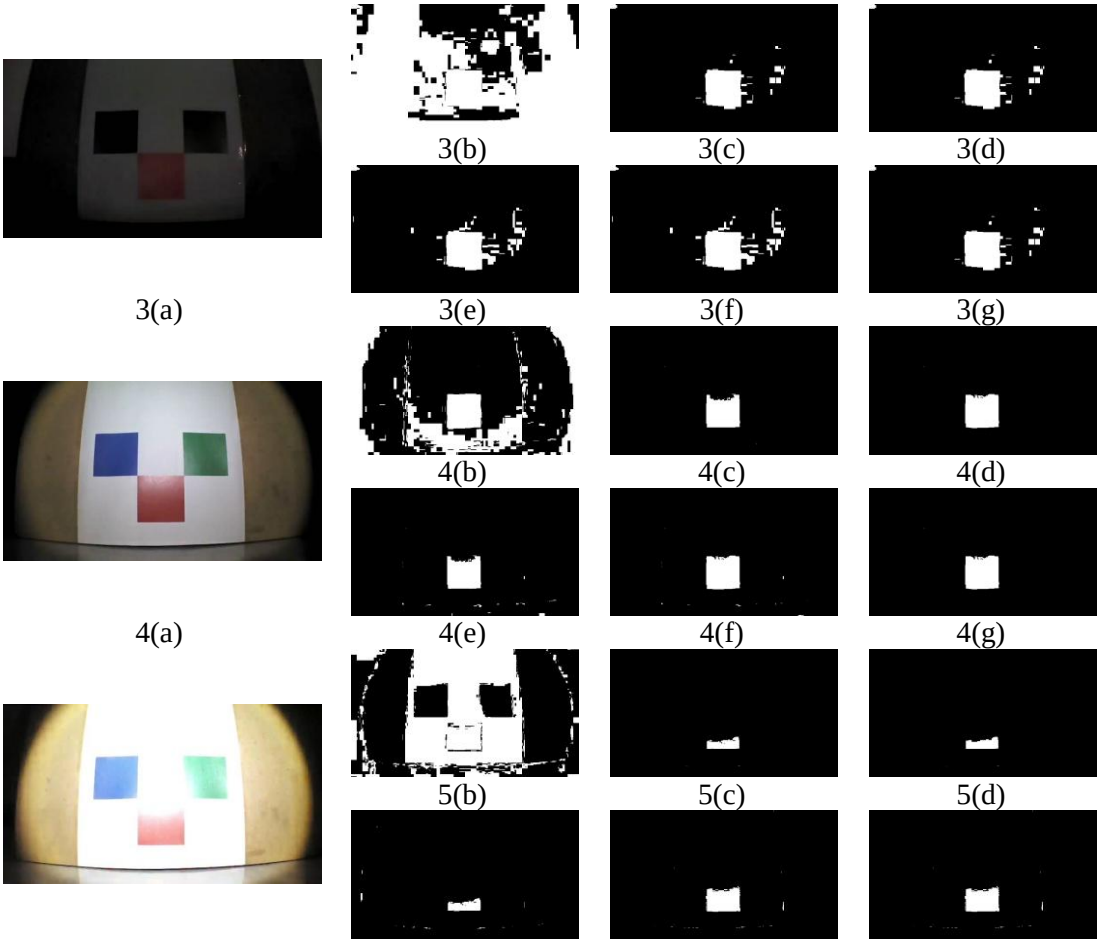

Figure 25 Colour identification using AMT with benchmark images

These colour identification results are also compared based on F_1 scores in percentage with the mean for each case highlighted in bold, as listed in Table III. F_1 scores have been frequently used as an accuracy indicator [115], it is typically computed based on precision and recall, as given in (99).

$$F_1 = \frac{2\beta\gamma}{\beta + \gamma} \tag{99}$$

where β and γ are precision and recall percentages, respectively.

Precision is the percentage of the correctly detected foreground pixels (true positive) among the detected pixels (true positive and false positive), while recall is the percentage of the correctly detected foreground pixels (true positive) among the actual foreground pixels (true positive and false negative). This can be hard to interpret, since true positive and false negative sums up to 100%, an alternate way is to substitute precision and recall with false positive and false negative, as given in (100) and (101). False positive is simply the percentage of pixels that are falsely identified as foreground, while false negative is simply the percentage of pixels that are falsely identified as background, as given in (102).

$$\gamma = 1 - F^{-} \tag{100}$$

$$\beta = \frac{1 - F^{-}}{1 - F^{-} + F^{+}} \tag{101}$$

$$F_1 = \frac{2(1 - F^{-})}{2 - F^{-} + F^{+}} \tag{102}$$

where β and γ are precision and recall percentages, respectively, F^{+} and F^{-} are false positive and false negative percentages, respectively.

TABLE III F_1 SCORES OF AMT WITH BENCHMARK IMAGES

Lighting	Simple			HCV			HCL		
Condition	F^{+}	F^{-}	F_1	F^{+}	F^{-}	F_1	F^{+}	F^{-}	F_1
Normal	566.88	0.00	26.08	3.80	1.36	97.45	3.82	1.08	97.58
Shadow 1	748.40	0.00	21.09	0.62	6.08	96.56	0.62	6.08	96.56
Shadow 2	1859.29	0.00	9.71	42.31	0.08	82.50	42.31	0.08	82.50
Illumination 1	638.23	0.02	23.86	0.95	11.34	93.52	1.81	3.13	97.51
Illumination 2	1061.08	3.53	15.34	0.08	74.14	41.07	0.07	73.00	42.50
Mean	974.78	0.71	**19.22**	9.55	18.60	**82.22**	9.73	16.67	**83.33**
Lighting	HSV			HSL			Adaptive		
Condition	F^{+}	F^{-}	F_1	F^{+}	F^{-}	F_1	F^{+}	F^{-}	F_1
Normal	13.34	0.42	93.54	7.76	0.01	96.26	3.82	1.08	97.58
Shadow 1	8.51	0.08	95.88	1.05	4.56	97.14	0.62	6.08	96.56
Shadow 2	74.12	0.08	72.92	74.12	0.08	72.92	42.31	0.08	82.50
Illumination 1	5.84	11.34	91.17	3.87	3.13	96.51	1.81	3.13	97.51
Illumination 2	2.92	72.85	41.75	2.68	33.89	78.33	2.68	33.89	78.33
Mean	20.95	16.95	**79.05**	17.90	8.33	**88.23**	10.25	8.85	**90.50**

Secondly, the proposed filter is also examined with the detection of different colours from various other images, as shown in Fig. 26. These images are collected from various sources and have different sizes, intensity and quality, from the top to the bottom: the first two images are captured by the front facing camera of the quadrotor used in this research, the next image is obtained from the INRIA person dataset and the rest are randomly selected from Google images. In the figure, the desired hue values of the target colours to be identified are listed in (a), the original images are shown in (b), the results of the proposed method with adaptive colour space selection are presented in (c). Note: for the last image, the desired colour is obtained automatically based on the average hue of the selected ROI.

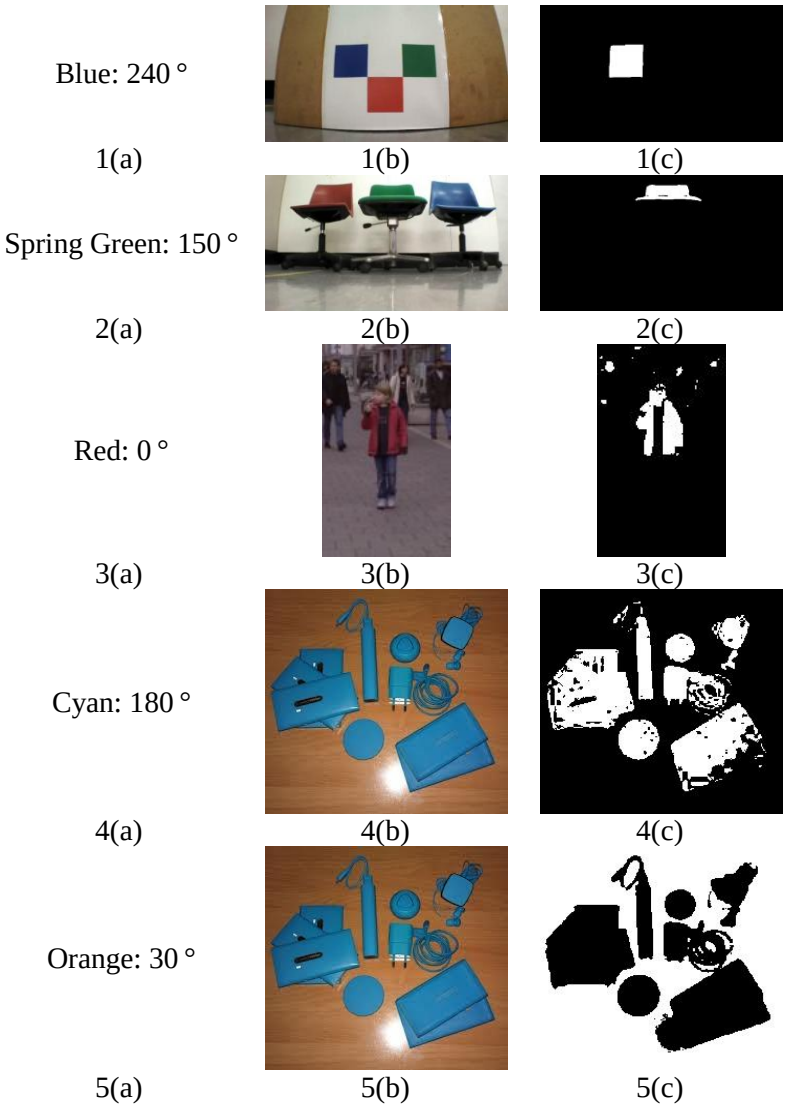

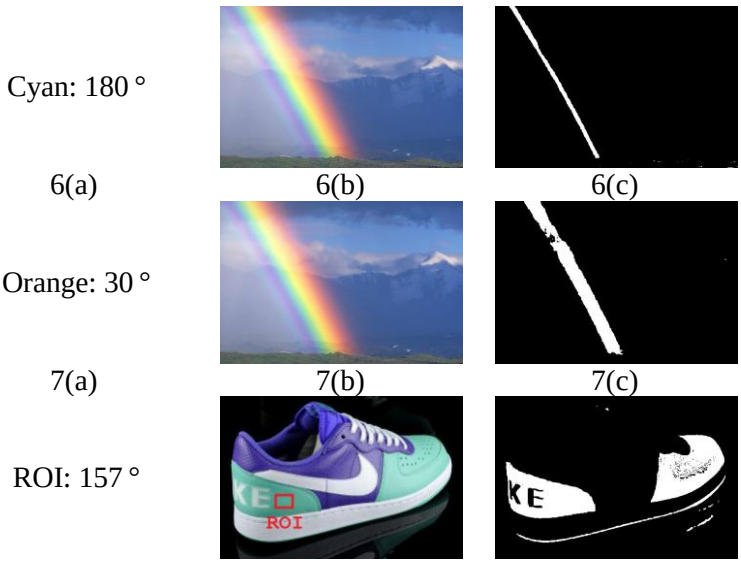

Figure 26 Colour identification using AMT with various other images

These results indicate the high effectiveness of the proposed AMT method as the required colours are extracted successfully under different lighting conditions and image qualities. In Table III, the mean F_1 score for the five benchmark images is 90.50% which is relatively high considered that four out of five cases are under the effects of illumination or shadow. In the case when the required colour is unknown, the proposed method can still be applied as long as a ROI is selected to indicate the desired colour, as demonstrated in case 8 of Fig. 26.

3.3 A Colour Model

Currently, approaches working with colour based features tend to rely on a specific colour model (typically hue based colour spaces). However, exiting colour models are known to be environment dependent in which slight changes of environmental factors such as lighting could greatly reduce the reliability. In this section, a colour

*Original images (based on case number):
3: *http://pascal.inrialpes.fr/data/human*
4 & 5: *http://geekongadgets.com/wp-content/uploads/2014/06/702325779.jpg*
6 & 7: *http://www.maxtheknife.com/marshax3/marsha36.jpg*
8: *https://www.sneakerfiles.com/wp-content/uploads/2009/04/nike-terminator-low-pink-blue-turquoise-purple-4.jpg*

model that can be used to detect the required colours accurately even with varying lighting conditions and image qualities is presented. The proposed colour model is named Hue-Purity-Brightness (HPB), it consists of three colour components: hue, purity and brightness. Hue represents the colour angle, purity represents the colourfulness and brightness represents intensity. It can be converted from the RGB colour model and it can be represented in three different 3D geometric shapes: sphere, hemisphere and cylinder, each of these 3D shapes also contains two variations.

3.3.1 HPB Sphere

In a RGB cube, since the distance can vary greatly between different points on the surface to the centroid (absolute grey), this could result unreliable detections for in-between colours as the distance does not truly reflect the actual difference between neighbouring colours. This problem could be alleviated if the distance between the surface to the centroid is normalised and this becomes the key idea of the first representation: HPB spherical colour model.

In this colour model, the original RGB colour cube is transformed into a spherical structure through radius equalising. Since the radius of the spherical model is affected by both purity and brightness, a variation is to preserve the original brightness of RGB by only consider the purity component during the equalising procedure, the first and second cases are referred to as type I and type II, respectively, as shown in Fig. 27.

The conversion from RGB to HPB sphere type I is given in (103) to (113).

$$\alpha = \tan^{-1}\left(\frac{g-\frac{1}{2}}{r-\frac{1}{2}}\right) \tag{103}$$

$$\beta = \tan^{-1}\left(\frac{b-\frac{1}{2}}{r-\frac{1}{2}}\right) \tag{104}$$

$$\gamma = \tan^{-1}\left(\frac{b-\frac{1}{2}}{g-\frac{1}{2}}\right) \tag{105}$$

$$D_r = \min\left(\frac{1}{2}, \left|\frac{1}{2\tan\alpha}\right|, \left|\frac{1}{2\tan\beta}\right|\right) \tag{106}$$

$$D_g = \begin{cases} \min\left(\frac{1}{2}, \left|\frac{1}{2\tan\gamma}\right|\right), & \alpha = 90° \text{ or } \alpha = 270° \\ \min\left(\frac{1}{2}, D_r|\tan\alpha|\right), & \text{otherwise} \end{cases} \tag{107}$$

$$D_b = \begin{cases} \min\left(\frac{1}{2}, \left|\frac{\tan\gamma}{2}\right|\right), & \alpha = 90° \text{ or } \alpha = 270° \\ \min\left(\frac{1}{2}, D_r|\tan\beta|\right), & \text{otherwise} \end{cases} \tag{108}$$

$$D = \sqrt{{D_r}^2 + {D_g}^2 + {D_b}^2} \tag{109}$$

$$\begin{bmatrix} X \\ Y \\ Z \end{bmatrix} = \begin{bmatrix} \frac{2}{\sqrt{6}} & -\frac{1}{\sqrt{6}} & -\frac{1}{\sqrt{6}} \\ 0 & \frac{1}{\sqrt{2}} & -\frac{1}{\sqrt{2}} \\ \frac{1}{\sqrt{3}} & \frac{1}{\sqrt{3}} & \frac{1}{\sqrt{3}} \end{bmatrix} \left(\frac{\sqrt{3}}{2D}\left(\begin{bmatrix} r \\ g \\ b \end{bmatrix} - \frac{1}{2}\right) + \frac{1}{2}\right) \tag{110}$$

$$H = \tan^{-1}\left(\frac{Y}{X}\right) \tag{111}$$

$$P = 2\sqrt{\frac{X^2 + Y^2}{3}} \tag{112}$$

$$B = \frac{Z}{\sqrt{3}} \tag{113}$$

where r, g and b are the red, green and blue intensities, respectively, α, β and γ are yaw, pitch and roll angles relate to the centroid, respectively, D is the maximum possible distance based on the yaw, pitch and roll angles, X, Y and Z form the global fixed frame corresponding to the original red, green and blue axes, respectively, H, P and B are the hue, purity and brightness components, respectively. Note: the 3×3 rotation matrix in (110) is simply used to align brightness with Z.

The conversion from RGB to HPB sphere type II is given in (114) to (123).

$$\begin{bmatrix} X' \\ Y' \\ Z \end{bmatrix} = \begin{bmatrix} \frac{2}{\sqrt{6}} & -\frac{1}{\sqrt{6}} & -\frac{1}{\sqrt{6}} \\ 0 & \frac{1}{\sqrt{2}} & -\frac{1}{\sqrt{2}} \\ \frac{1}{\sqrt{3}} & \frac{1}{\sqrt{3}} & \frac{1}{\sqrt{3}} \end{bmatrix} \begin{bmatrix} r \\ g \\ b \end{bmatrix} \tag{114}$$

$$H = \tan^{-1}\left(\frac{Y'}{X'}\right) \tag{115}$$

$$\theta = H - \left\lfloor \frac{H}{120°} \right\rfloor 120° \tag{116}$$

$$\delta = \sqrt{Z\left(Z - \sqrt{3}\right) + 1} \tag{117}$$

$$\varphi = \sin^{-1}\left(\frac{Z\sqrt{3} - 1}{2\delta}\right) \tag{118}$$

$$D' = \begin{cases} \delta\sqrt{2}\left(\frac{\cos\varphi}{\cos\theta}\right), & \theta \leq \varphi \\ -\delta\sqrt{2}\left(\frac{\cos\varphi}{\cos(\theta + 60°)}\right), & \theta > \varphi \text{ and } \theta + \varphi \geq 120° \\ \delta\sqrt{2}\left(\frac{\sin(\varphi + 30°)}{\cos(\theta - 60°)}\right), & \text{otherwise} \end{cases} \tag{119}$$

$$D = \begin{cases} \frac{Z}{\sqrt{2}\sin\left(150° + \left\lfloor \frac{H}{120°} \right\rfloor 120° - H\right)}, & Z \leq \frac{1}{\sqrt{3}} \\ \frac{\sqrt{3} - Z}{\sqrt{2}\sin\left(210° + \left\lfloor \frac{H - 60°}{120°} \right\rfloor 120° - H\right)}, & Z \geq \frac{2}{\sqrt{3}} \\ D', & \frac{1}{\sqrt{3}} < Z < \frac{2}{\sqrt{3}} \end{cases} \tag{120}$$

$$\begin{bmatrix} X \\ Y \end{bmatrix} = \begin{bmatrix} X' \\ Y' \end{bmatrix} \frac{1}{D} \sqrt{Z\left(\sqrt{3} - Z\right)} \tag{121}$$

$$P = 2\sqrt{\frac{X^2 + Y^2}{3}} \tag{122}$$

$$B = \frac{Z}{\sqrt{3}} \tag{123}$$

where r, g and b are the red, green and blue intensities, respectively, D is the maximum possible distance based on the hue angle, X, Y and Z form the global fixed frame corresponding to the original red, green and blue axes, respectively, H, P and B are the hue, purity and brightness components, respectively. Note: the 3×3 rotation matrix in (114) is simply used to align brightness with Z and superscript $'$ indicates the intermediate value.

The inverse conversion from HPB sphere type I to RGB is given in (124) to (135).

$$X = \frac{P\sqrt{3}}{2}\sin H \tag{124}$$

$$Y = \frac{P\sqrt{3}}{2}\cos H \tag{125}$$

$$Z = B\sqrt{3} \tag{126}$$

$$\begin{bmatrix} r' \\ g' \\ b' \end{bmatrix} = \begin{bmatrix} \frac{2}{\sqrt{6}} & 0 & \frac{1}{\sqrt{3}} \\ -\frac{1}{\sqrt{6}} & \frac{1}{\sqrt{2}} & \frac{1}{\sqrt{3}} \\ -\frac{1}{\sqrt{6}} & -\frac{1}{\sqrt{2}} & \frac{1}{\sqrt{3}} \end{bmatrix} \begin{bmatrix} X \\ Y \\ Z \end{bmatrix} \tag{127}$$

$$\alpha = \tan^{-1}\left(\frac{g' - \frac{1}{2}}{r' - \frac{1}{2}}\right) \tag{128}$$

$$\beta = \tan^{-1}\left(\frac{b' - \frac{1}{2}}{r' - \frac{1}{2}}\right) \tag{129}$$

$$\gamma = \tan^{-1}\left(\frac{b' - \frac{1}{2}}{g' - \frac{1}{2}}\right) \tag{130}$$

$$D_r = \min\left(\frac{1}{2}, \left|\frac{1}{2\tan\alpha}\right|, \left|\frac{1}{2\tan\beta}\right|\right) \tag{131}$$

$$D_g = \begin{cases} \min\left(\frac{1}{2}, \left|\frac{1}{2\tan\gamma}\right|\right), & \alpha = 90° \text{ or } \alpha = 270° \\ \min\left(\frac{1}{2}, D_r|\tan\alpha|\right), & \text{otherwise} \end{cases} \tag{132}$$

$$D_b = \begin{cases} \min\left(\frac{1}{2}, \left|\frac{\tan\gamma}{2}\right|\right), & \alpha = 90° \text{ or } \alpha = 270° \\ \min\left(\frac{1}{2}, D_r|\tan\beta|\right), & \text{otherwise} \end{cases} \tag{133}$$

$$D = \sqrt{{D_r}^2 + {D_g}^2 + {D_b}^2} \tag{134}$$

$$\begin{bmatrix} r \\ g \\ b \end{bmatrix} = \left(\frac{2D}{\sqrt{3}}\left(\begin{bmatrix} r' \\ g' \\ b' \end{bmatrix} - \frac{1}{2}\right) + \frac{1}{2}\right) \tag{135}$$

where r, g and b are the red, green and blue intensities, respectively, α, β and γ are yaw, pitch and roll angles relate to the centroid, respectively, D is the maximum possible distance based on the yaw, pitch and roll angles, X, Y and Z form the global fixed frame corresponding to the original red, green and blue axes, respectively, H, P and B are the hue, purity and brightness components, respectively. Note: the 3×3 rotation matrix in (127) is simply the inverse (and transpose due to orthogonality) of the rotation matrix in (110). Superscript $'$ indicates the intermediate value.

The inverse conversion from HPB sphere type II to RGB is given in (136) to (145).

$$X = \frac{P\sqrt{3}}{2}\sin H \tag{136}$$

$$Y = \frac{P\sqrt{3}}{2}\cos H \tag{137}$$

$$Z = B\sqrt{3} \tag{138}$$

$$\theta = H - \left\lfloor\frac{H}{120°}\right\rfloor 120° \tag{139}$$

$$\delta = \sqrt{Z\left(Z - \sqrt{3}\right) + 1} \tag{140}$$

$$\varphi = \sin^{-1}\left(\frac{Z\sqrt{3} - 1}{2\delta}\right) \tag{141}$$

$$D' = \begin{cases} \delta\sqrt{2}\left(\frac{\cos\varphi}{\cos\theta}\right), & \theta \le \varphi \\ -\delta\sqrt{2}\left(\frac{\cos\varphi}{\cos(\theta + 60°)}\right), & \theta > \varphi \text{ and } \theta + \varphi \ge 120° \\ \delta\sqrt{2}\left(\frac{\sin(\varphi + 30°)}{\cos(\theta - 60°)}\right), & \text{otherwise} \end{cases} \tag{142}$$

$$D = \begin{cases} \dfrac{Z}{\sqrt{2}\sin\left(150° + \left\lfloor \dfrac{H}{120°} \right\rfloor 120° - H\right)}, & Z \le \dfrac{1}{\sqrt{3}} \\ \dfrac{\sqrt{3} - Z}{\sqrt{2}\sin\left(210° + \left\lfloor \dfrac{H - 60°}{120°} \right\rfloor 120° - H\right)}, & Z \ge \dfrac{2}{\sqrt{3}} \\ D', & \dfrac{1}{\sqrt{3}} < Z < \dfrac{2}{\sqrt{3}} \end{cases} \tag{143}$$

$$\begin{bmatrix} X' \\ Y' \end{bmatrix} = \begin{bmatrix} X \\ Y \end{bmatrix} \frac{D}{\sqrt{Z\left(\sqrt{3} - Z\right)}} \tag{144}$$

$$\begin{bmatrix} r \\ g \\ b \end{bmatrix} = \begin{bmatrix} \dfrac{2}{\sqrt{6}} & 0 & \dfrac{1}{\sqrt{3}} \\ -\dfrac{1}{\sqrt{6}} & \dfrac{1}{\sqrt{2}} & \dfrac{1}{\sqrt{3}} \\ -\dfrac{1}{\sqrt{6}} & -\dfrac{1}{\sqrt{2}} & \dfrac{1}{\sqrt{3}} \end{bmatrix} \begin{bmatrix} X' \\ Y' \\ Z \end{bmatrix} \tag{145}$$

where *r*, *g* and *b* are the red, green and blue intensities, respectively, *D* is the maximum possible distance based on the hue angle, *X*, *Y* and *Z* form the global fixed frame corresponding to the original red, green and blue axes, respectively, *H*, *P* and *B* are the hue, purity and brightness components, respectively. Note: the 3×3 rotation matrix in (145) is simply the inverse (and transpose due to orthogonality) of the rotation matrix in (110). Superscript ′ indicates the intermediate value.

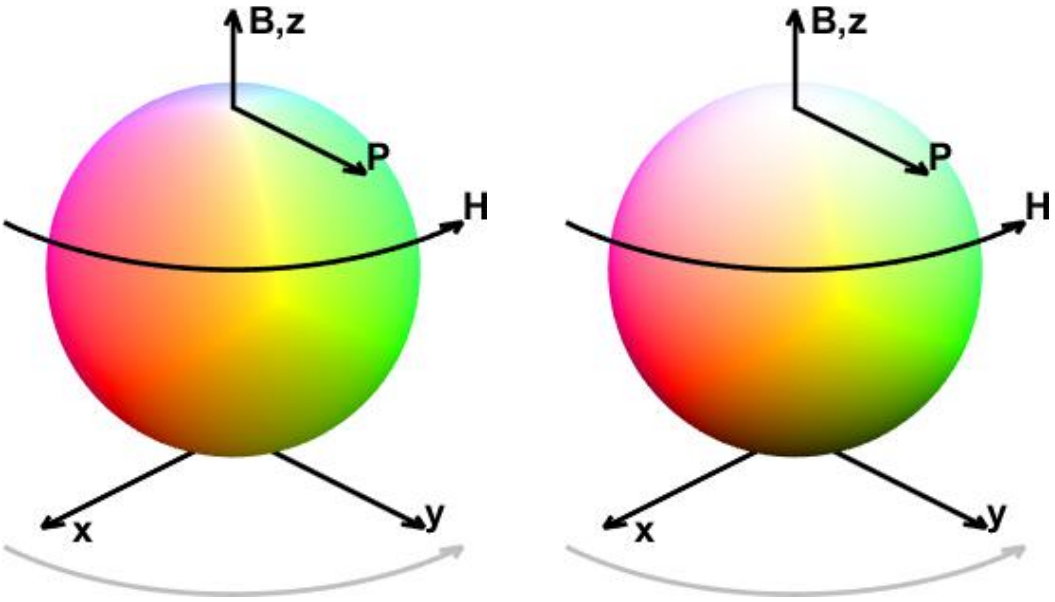

(a) HPB sphere I (b) HPB sphere II

Figure 27 HPB spherical colour models

3.3.2 HPB Hemisphere

In the first representation, the original RGB cube is transformed into HPB sphere so that the distance between any point on the surface to the centroid (absolute grey) stays the same. However, since the lengths of the brightness and the purity components are different (brightness is exactly twice as long as purity), another model is proposed in the second representation: HPB hemispherical colour model. The purity and brightness components of the two spheres (type I and type II) in the first representation are normalised in the new model, as shown in Fig. 28.

The conversion from RGB to HPB hemisphere type I is very similar to the spherical conversion (type I) in the first representation except an additional step (146) is inserted after (110).

$$\begin{bmatrix} X_h \\ Y_h \end{bmatrix} = \begin{bmatrix} X_s \\ Y_s \end{bmatrix} \sqrt{\frac{\sqrt{3} + Z_s}{Z_s}} \tag{146}$$

where *X*, *Y* and *Z* form the global fixed frame corresponding to the original red, green and blue axes, respectively, *h* and *s* represent hemisphere and sphere, respectively.

The conversion from RGB to HPB hemisphere type II is very similar to the spherical conversion (type II) in the first representation except (128) is replaced with (147).

$$\begin{bmatrix} X \\ Y \end{bmatrix} = \begin{bmatrix} X' \\ Y' \end{bmatrix} \frac{1}{D} \sqrt{3 - Z^2} \tag{147}$$

where *X*, *Y* and *Z* form the global fixed frame corresponding to the original red, green and blue axes, respectively, *D* is the maximum possible distance based on the hue angle. Note: superscript ‘ indicates the intermediate value.

Furthermore, since the lengths of purity and brightness component are now equal (for both type I and type II), purity computation needs to be updated by replacing (112) and (122) with (148).

$$P = \sqrt{\frac{X^2 + Y^2}{3}} \tag{148}$$

where *X* and *Y* are the global fixed axes corresponding to the original red and green axes, respectively, *P* is the purity component.

Correspondingly, during the inverse conversion (for both type I and type II), *X* and *Y* computations need to be updated by replacing (124) and (125), (136) and (137) with (149) and (150).

$$X = P\sqrt{3} \sin H \tag{149}$$

$$Y = P\sqrt{3} \cos H \tag{150}$$

where *X* and *Y* are the global fixed axes corresponding to the original red and green axes, respectively, *H* and *P* are the hue and purity components, respectively.

Then, the only difference between the inverse conversion from HPB hemisphere type I to RGB and the spherical inverse (type I) in the first representation is the additional step (151) which is inserted before (127).

$$\begin{bmatrix} X_s \\ Y_s \end{bmatrix} = \begin{bmatrix} X_h \\ Y_h \end{bmatrix} \sqrt{\frac{Z_h}{\sqrt{3} + Z_h}} \tag{151}$$

where *X*, *Y* and *Z* form the global fixed frame corresponding to the original red, green and blue axes, respectively, *h* and *s* represent hemisphere and sphere, respectively.

The only difference between the inverse conversion from HPB hemisphere type II to RGB and the spherical inverse (type II) in the first representation is the replacement of (144) with (152).

$$\begin{bmatrix} X' \\ Y' \end{bmatrix} = \begin{bmatrix} X \\ Y \end{bmatrix} \frac{D}{\sqrt{3 - Z^2}} \tag{152}$$

where *X*, *Y* and *Z* form the global fixed frame corresponding to the original red, green and blue axes, respectively, *D* is the maximum possible distance based on the hue angle. Note: superscript ‘ indicates the intermediate value.

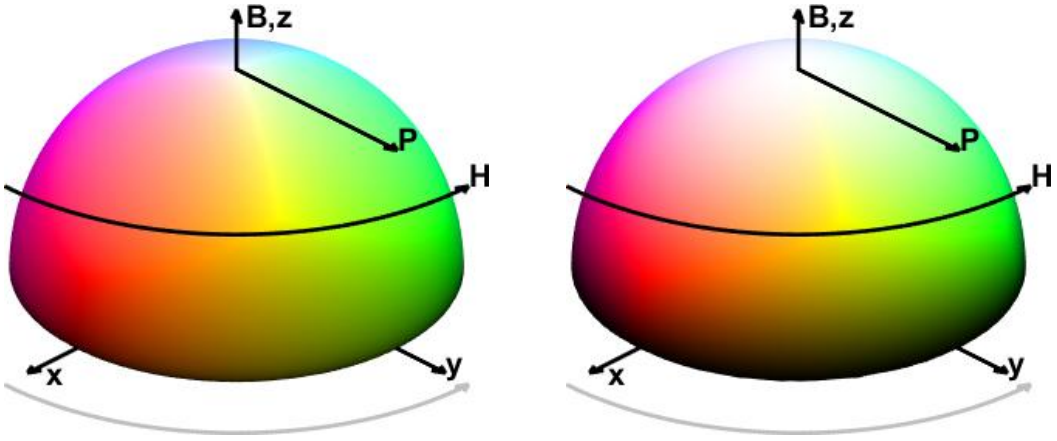

(a) HPB hemisphere I (b) HPB hemisphere II

Figure 28 HPB hemispherical colour models

3.3.3 HPB Cylinder

Since the length of the purity component of the spherical model in the first representation is not constant, an alternative model is proposed in the third representation: HPBr cylindrical colour model. The cylindrical structure is the result of replacing the absolute distance with relative distance in the purity component (equalising purity along brightness) of the spherical model in the first representation, as shown in Fig. 29.

Again, the conversion from RGB to HPB cylinder type I is very similar to the spherical conversion (type I) except an additional step (153) is inserted after (110).

$$\begin{bmatrix} X_c \\ Y_c \end{bmatrix} = \begin{bmatrix} X_s \\ Y_s \end{bmatrix} \sqrt{\frac{3}{4Z_s\left(\sqrt{3} - Z_s\right)}} \tag{153}$$

where *X*, *Y* and *Z* form the global fixed frame corresponding to the original red, green and blue axes, respectively, *c* and *s* represent cylinder and sphere, respectively.

The conversion from RGB to HPB cylinder type II is very similar to the spherical conversion (type II) except (121) is replaced with (154).

$$\begin{bmatrix} X \\ Y \end{bmatrix} = \begin{bmatrix} X' \\ Y' \end{bmatrix} \frac{\sqrt{3}}{2D} \tag{154}$$

where *X*, *Y* and *Z* form the global fixed frame corresponding to the original red, green and blue axes, respectively, *D* is the maximum possible distance based on the hue angle. Note: superscript ‘ indicates the intermediate value.

Correspondingly, the only difference between the inverse conversion from HPB cylinder type I to RGB and the spherical inverse (type I) is the additional step (155) which is inserted before (127).

$$\begin{bmatrix} X_s \\ Y_s \end{bmatrix} = \begin{bmatrix} X_c \\ Y_c \end{bmatrix} \sqrt{\frac{4Z_c(\sqrt{3} - Z_c)}{3}} \tag{155}$$

where *X*, *Y* and *Z* form the global fixed frame corresponding to the original red, green and blue axes, respectively, *c* and *s* represent cylinder and sphere, respectively.

The only difference between the inverse conversion from HPB cylinder type II to RGB and the spherical inverse (type II) is the replacement of (144) with (156).

$$\begin{bmatrix} X' \\ Y' \end{bmatrix} = \begin{bmatrix} X \\ Y \end{bmatrix} \frac{2D}{\sqrt{3}} \tag{156}$$

where *X*, *Y* and *Z* form the global fixed frame corresponding to the original red, green and blue axes, respectively, *D* is the maximum possible distance based on the hue angle. Note: superscript ′ indicates the intermediate value.

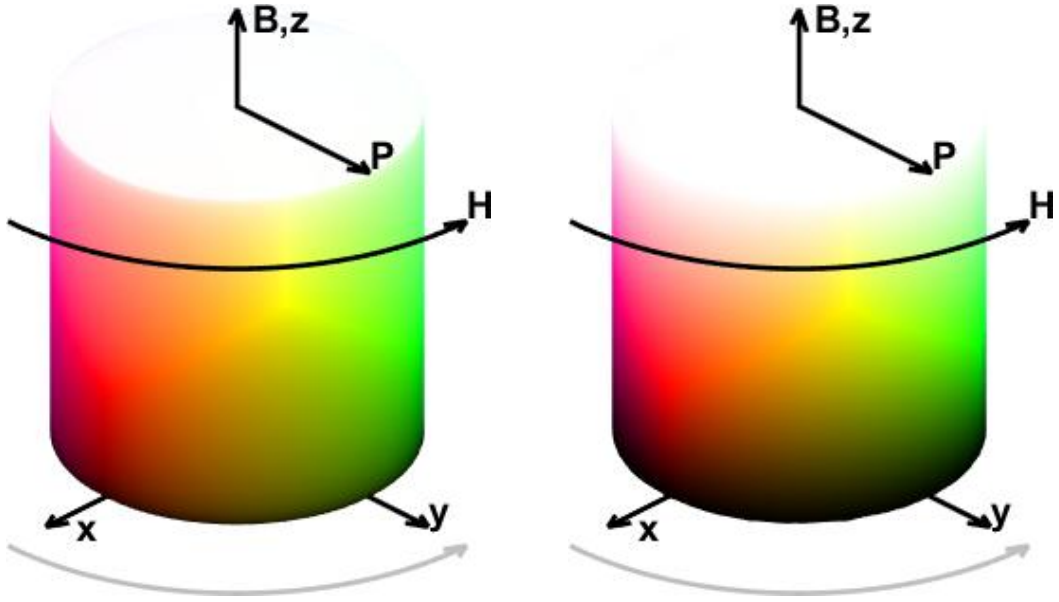

(a) HPB cylinder I (b) HPB cylinder II

Figure 29 HPB cylindrical colour models

To assess the effectiveness of the proposed HPB model, the model is examined with the detection of red square in the five benchmark images using AMT (describe earlier in Section 3.2), as shown in Fig. 30. AMT is selected since it is designed for hue based colour filtering and the results can be compared with existing hue based colour models such as HCV, HSV, HSV and HSL.

These five images are captured by the front facing camera of the quadrotor used in this research under very different lighting conditions, from the top to the bottom: the first image is captured under normal lighting conditions, the next two images are captured under shadow effects and the last two images are capture under illumination effects. In the figure, the original benchmark images are shown in (a), colour identification results with sphere type I, hemisphere type I, cylinder type I, sphere type II, hemisphere type II and cylinder type II models are presented, respectively.

These colour identification results are also compared based on F_1 scores in percentage with the mean for each case highlighted in bold, as listed in Table IV. In the table, F^+ and F^- are false positive and false negative percentages, respectively, F_1 scores are computed based on false positive and false negative percentages using (109). Additionally, the overall and individual rankings of colour models based on F_1 scores are provided with the mean highlighted in bold, as listed in Table V. Note: F_1 scores of existing hue based colour models are listed earlier in Table III.

As demonstrated in the results using benchmark images, compared to existing hue based colour models, the proposed HPB model is relatively more effective at determining the correct colours. Among all the cases, the hemisphere type I model has achieved the highest individual F_1 score (98.30%), while cylinder type I model has produced the best overall outcome (89.00%).

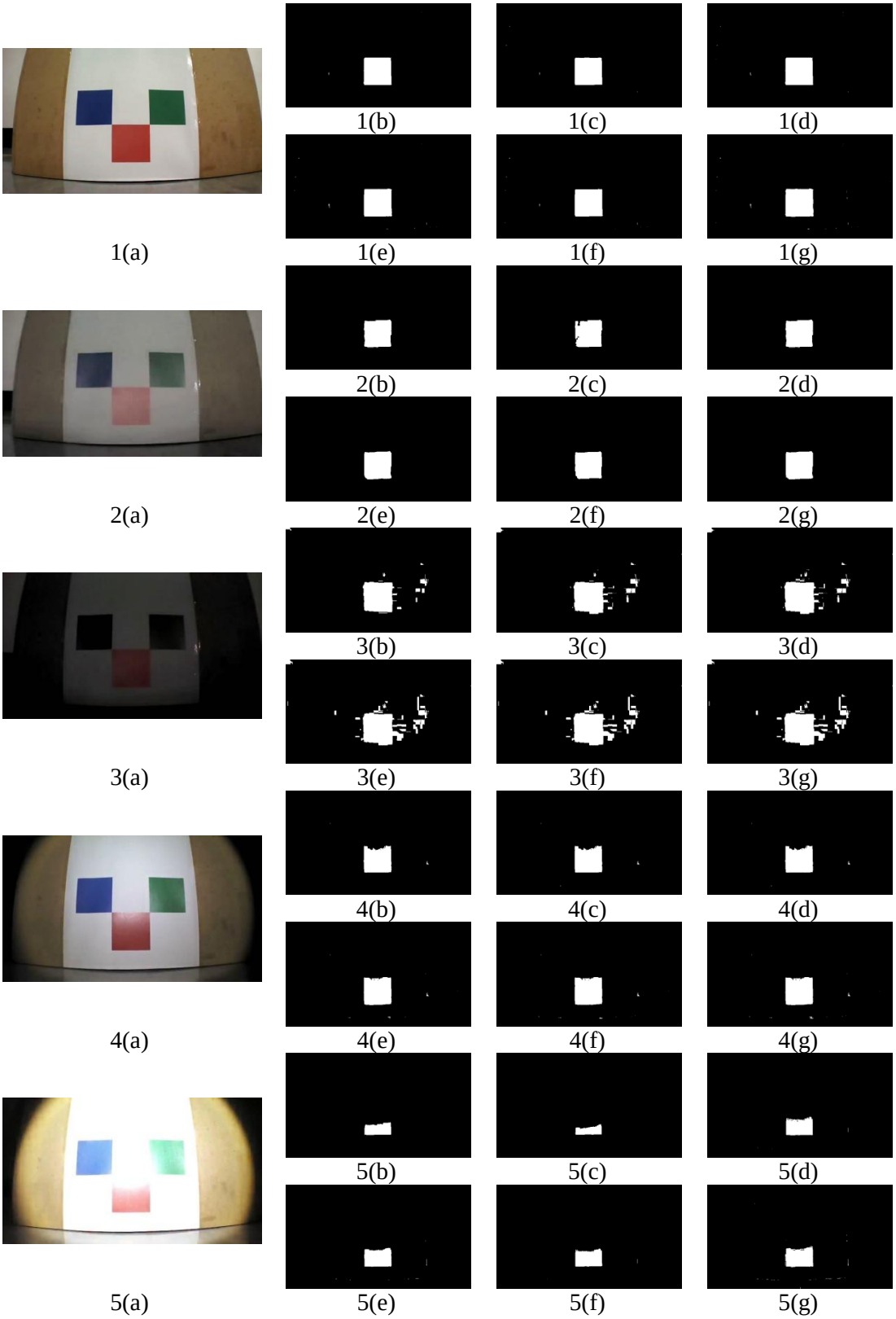

Figure 30 Colour identification with HPB model

TABLE IV F_1 SCORES OF COLOUR IDENTIFICATION WITH HPB MODEL

Lighting Condition	Sphere I			Hemisphere I			Cylinder I		
	F^+	F^-	F_1	F^+	F^-	F_1	F^+	F^-	F_1
Normal	3.76	0.12	98.09	3.03	0.42	98.30	3.99	0.11	97.99
Shadow 1	2.31	3.58	97.04	1.25	7.42	95.53	2.33	3.58	97.03
Shadow 2	31.93	0.00	86.23	44.75	0.00	81.72	47.31	0.00	80.87
Illumination 1	1.88	7.78	95.02	1.76	7.82	95.06	2.05	7.78	94.94
Illumination 2	0.00	60.58	56.55	0.00	72.64	42.96	0.22	40.92	74.17
Mean	7.98	14.41	**86.59**	10.16	17.66	**82.71**	11.18	10.48	**89.00**
Lighting Condition	Sphere II			Hemisphere II			Cylinder II		
	F^+	F^-	F_1	F^+	F^-	F_1	F^+	F^-	F_1
Normal	6.25	0.02	96.96	4.41	0.04	97.82	7.41	0.02	96.42
Shadow 1	2.24	1.91	97.93	0.68	4.73	97.24	2.24	1.75	98.01
Shadow 2	75.94	0.00	72.48	75.95	0.00	72.48	75.95	0.00	72.48
Illumination 1	4.30	2.42	96.67	4.00	2.45	96.80	4.69	2.41	96.49
Illumination 2	1.23	36.51	77.09	0.29	41.41	73.75	3.00	32.85	78.93
Mean	17.99	8.17	**88.23**	17.07	9.73	**87.62**	18.66	7.41	**88.46**

TABLE V RANKINGS OF COLOUR MODELS BASED ON F_1 SCORES

Rank	Normal		Shadow 1		Shadow 2	
	Model	F_1	Model	F_1	Model	F_1
1st	Hemisphere I	98.30	Cylinder II	98.01	Sphere I	86.23
2nd	Sphere I	98.09	Sphere II	97.93	HCV	82.50
3rd	Cylinder I	97.99	Hemisphere II	97.24	HCL	82.50
4th	Hemisphere II	97.82	HSL	97.14	Hemisphere I	81.72
5th	HCL	97.58	Sphere I	97.04	Cylinder I	80.87
6th	HCV	97.45	Cylinder I	97.03	HSV	72.92
7th	Sphere II	96.96	HCV	96.56	HSL	72.92
8th	Cylinder II	96.42	HCL	96.56	Sphere II	72.48
9th	HSL	96.26	HSV	95.88	Hemisphere II	72.48
10th	HSV	93.54	Hemisphere I	95.83	Cylinder II	72.48
Rank	Illumination 1		Illumination 2		Overall	
	Model	F_1	Model	F_1	Model	F_1
1st	HCL	97.51	Cylinder II	78.93	Cylinder I	**89.00**
2nd	Hemisphere II	96.80	HSL	78.33	Cyldiner II	**88.46**
3rd	Sphere II	96.67	Sphere II	77.09	Sphere II	**88.23**
4th	HSL	96.51	Cylinder I	74.17	HSL	**88.23**
5th	Cylinder II	96.49	Hemisphere II	73.75	Hemisphere II	**87.62**
6th	Hemisphere I	95.06	Sphere I	56.55	Sphere I	**86.59**
7th	Sphere I	95.02	Hemisphere I	42.96	HCL	**83.33**
8th	Cylinder I	94.94	HCL	42.5	Hemisphere I	**82.71**
9th	HCV	93.52	HSV	41.75	HCV	**82.22**
10th	HSV	91.17	HCV	41.07	HSV	**79.05**

In summary, this chapter proposed three methods in colour based feature detection: a colour enhancement method for colour segmentation (CCE), a colour identification method (AMT) and a colour model (HPB) for improved colour detection. CCE is an efficient and simple filtering tool to boost the colour saliency level of the image, the drawback of this procedure is the loss of texture detail. AMT is an adaptive multi-channel colour identification method that can be applied even when the image is heavily affected by effects such as illumination and shadow. However, the colour space selection scheme employed by this approach is currently limited to hue based colour spaces. HPB is a novel colour model that consists of three colour components: hue, purity and brightness. Compared to existing hue based colour models, HPB model allows enhanced colour detection from images. However, the computation required to convert between the model and RGB is relatively more expensive than traditional hue based models. These methods have not been implemented into the real-time tracking and pursuit system (Chapter 5) primarily due to the limited computational power.

Chapter 4 Proposed Methods in Object Detection and Tracking

This chapter proposes two methods in object detection and tracking. Section 4.1 introduces a human detection method using gradient maps and Section 4.2 presents an object tracking method using tiered templates. The contents of this chapter are based on revised versions of author's publications resulting from this research [116–118]. These publications can also be found in the list of publications in Section 1.4.

4.1 A Human Detection Method

Existing human detection methods tend to rely heavily on pre-training. In this section, an alternate route is proposed by introducing a method that is capable of detecting, extracting and segmenting the human body figure robustly from the background without prior training. This is done by detecting face, head and shoulder separately, mainly using gradient maps.

The proposed method is named Gradient based Human Detection (GHD), it consists of four stages: scaled gradient mapping, blob filtering, body estimation and figure extraction. A flowchart of the method is shown in Fig. 31.

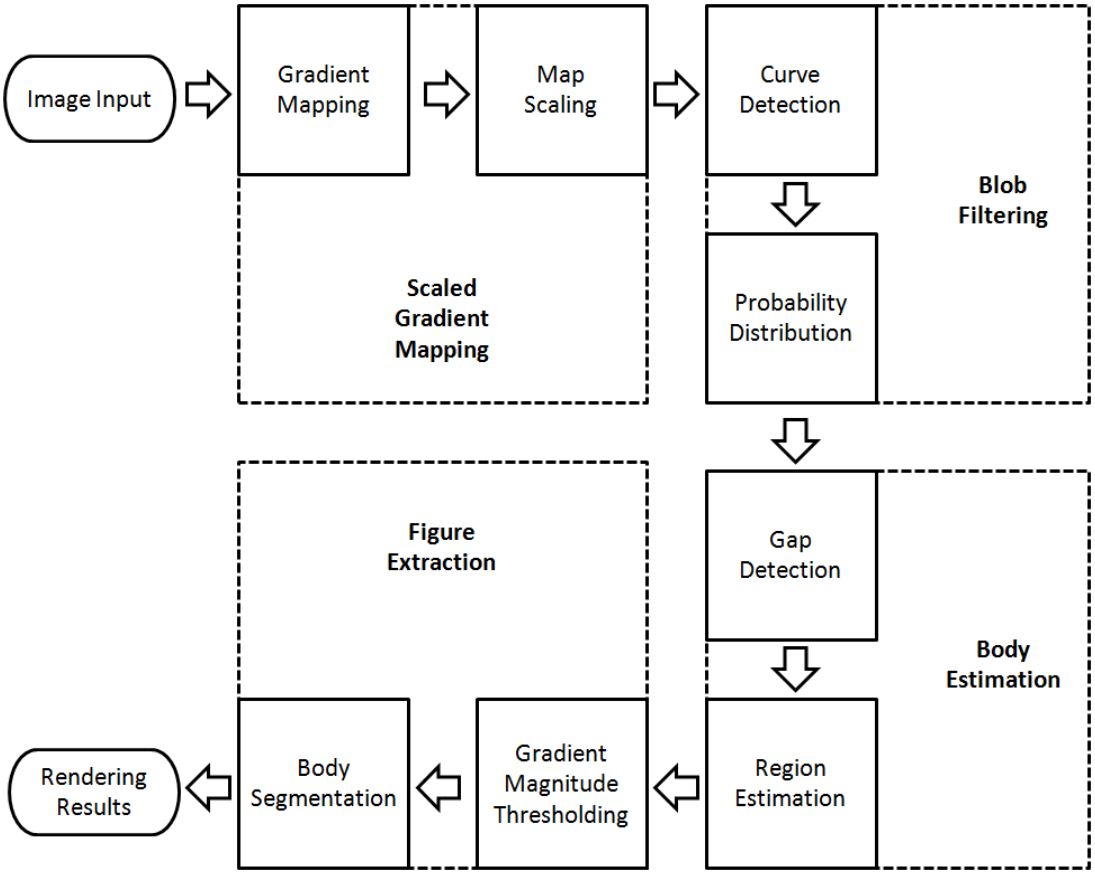

Figure 31 Flowchart of the proposed human detection method

4.1.1 Scaled Gradient Mapping

The first stage of the GHD is scaled gradient mapping in which two types of maps are generated and scaled: magnitude and orientation. The input image is firstly converted to greyscale, gradients are then obtained along both horizontal and vertical axes of the image using two simple kernels, as given earlier in (73) and (74). The gradient magnitude and orientation maps are then generated using (157) and (158).

$$r = \sqrt{(x^+ + x^-)^2 + (y^+ + y^-)^2} \tag{157}$$

$$\theta = \tan^{-1}\left(\frac{y^+ - y^-}{x^+ - x^-}\right) \tag{158}$$

where the superscripts + and – represent the positive (right, down) and negative (left, up) directions, respectively, x and y are the gradient values obtained from the kernels

along horizontal and vertical axes, respectively, r and θ are magnitude and orientation of the gradient, respectively.

Finally, both gradient maps are scaled into 8 smaller sizes by a set of scaling factors, as given in (159).

$$\alpha = \left\{\frac{1}{2}, \frac{1}{3}, \frac{1}{4}, \frac{1}{6}, \frac{1}{8}, \frac{1}{12}, \frac{1}{16}, \frac{1}{24}\right\} \tag{159}$$

where α represents the set of scaling factors. The values are selected empirically to accommodate various sizes of human in the image.

During the scaling procedure, max pooling is applied for the magnitude maps in which only the local maximum within each block is saved. The size of the block is related to the scaling factor and is simply $1/\alpha$. For the orientation maps, both positive and negative directions of the gradient along horizontal and vertical axes are considered, as given in (160).

$$\theta_\alpha = \tan^{-1}\left(\frac{Y^+ - Y^-}{X^+ - X^-}\right) \tag{160}$$

where θ_α is the scaled orientation, the superscripts + and – represent the positive (right, down) and negative (left, up) directions, respectively, X and Y are the maximum gradient within the block along horizontal and vertical axes, respectively.

The original image and gradient orientation map are shown in Fig. 32 (a) and (b), respectively.

(a) Original input (b) Gradient orientation map

Figure 32 Original input and gradient orientation map

4.1.2 Blob Filtering

The second stage of the GHD is blob filtering in which blobs are formed and filtered based on the results of face, head and shoulder detectors. Firstly, as both head and shoulder have distinctive curvatures, curve detection is employed to detect possible head and shoulder regions. This is done via two curve templates which can be represented as two 3 by 3 kernels, as given in (161) and (162).

$$C_1 = \begin{bmatrix} \emptyset & 116.57° & 90° \\ 153.43° & \emptyset & \emptyset \\ 180° & \emptyset & \emptyset \end{bmatrix} \quad (161)$$

$$C_2 = \begin{bmatrix} 90° & 63.43° & \emptyset \\ \emptyset & \emptyset & 26.57° \\ \emptyset & \emptyset & 0° \end{bmatrix} \quad (162)$$

where C_1 and C_2 are the two curve templates, $\emptyset$ represents null (element not considered). The values are determined based on their relative angles from each of the bottom corners in the kernels.

Using sliding window approach, the scaled gradient maps are then searched for patches that contain similar gradient features with the templates. The similarity level between the patch and the template can be determined by computing the weighted difference using (163).

$$\psi = \frac{R \sum_i^n \theta_t - \theta_p}{\sum_i^n r_p} \tag{163}$$

where ψ is the weighted difference, θ_t and θ_p are the orientations of the patch and template, respectively, r_p is the magnitude, R is the maximum magnitude of the image, n is the total number of valid(non-null) elements in the template (n = 4).

When the weighted difference of a region falls below a certain threshold, it can be said that there is a high chance of seeing parts of the head or shoulder, the weight difference threshold for curve detection is obtained using (164). The results of the curve detection based on the curve templates are then joined together to form blobs. This is done by horizontal filling in which a blob is formed if the distance between the pair of curves is smaller than the maximum detectable width of the human figure in the image, as given in (165).

$$T_C = 30°\omega \tag{164}$$

$$H\left(\frac{\varphi}{2\varphi + 1}\right) \leq T_d \tag{165}$$

where T_C is the maximum weighted difference threshold for curve detection, ω is the scale factor based on the number of blobs formed in the image, φ is the golden ratio ($\varphi \approx 1.62$), H is the height of the image, T_d is the maximum width threshold between the pair of curves for horizontal filling. Note: the default ω value is 1, if the total number of blobs found is less than 2, ω is increased by 0.5 and detection process restarts, ω is capped at 2.

Golden ratio is known to be relatively accurate in estimating the proportions of the human body [119], by letting the width of the head equal to 1, the relative size of the human figure can be found as shown in Fig. 33.

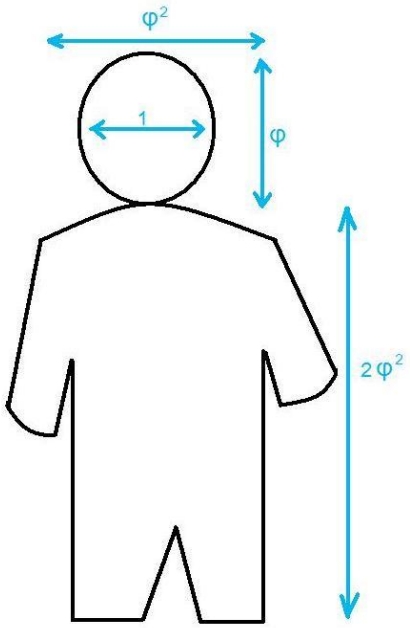

Figure 33 Estimated human body proportions using golden ratio (head to knee)

For face detection, a simple feature based Haar classifier [120] is implemented. Since the method is prioritised on head and shoulder detections, the parameters of the face classifier are tuned towards high precision rather than high recall. As Haar classifiers tend to yield clusters of ROIs around the detected faces, the number of overlaps at the cluster centre is used as the confidence measure for the face detector. Two cut-off thresholds have been established based on the size of the image to describe the confidence of the detected ROI as low, medium or high, as given in (166) to (168).

$$t = \max\left(1, \frac{\min(W, H)}{500}\right) \tag{166}$$

$$f_l = 4(t^2 + t) \tag{167}$$

$$f_h = 8(2t^2 + t) \tag{168}$$

where f_l and f_h are the two thresholds for low and high confidences, t is a size parameter determined based on the image width W and height H.

At this stage, several (or no) blobs may form depending on the level of background noise. To identify the true head and shoulder blobs, a probability model based on

Gaussian probability distribution function is employed for blob filtering in which the pair of blobs with the highest probability is obtained. In the case when the head or shoulder or both blobs are missing, but the confidence for face detection is high, the blobs are reconstructed. The model considered four possible cases: face only, face and head, face and shoulder, head and shoulder. Each case is considered separately and competes with each other in which the case with the highest probability selected.

The probability for the face only case is given in (169).

$$P_{FO} = \begin{cases} \sqrt{\frac{f}{4f_h}}, & f < f_h \\ \sqrt{\frac{1}{4} - \sqrt{\frac{f_h}{16f}}} + \frac{1}{2}, & f \geq f_h \end{cases} \tag{169}$$

where P_{FO} is the probability for the face only case, f and f_h are the face detection confidence and high confidence cut-off.

For the face and head case, the normalised confidence of the face detection is computed first based on the overlapped area of face and head, as given in (170). The probability of the case is then calculated using (171).

$$f' = f\left(\frac{a_o}{\max(a_f, a_h)}\right) \tag{170}$$

$$P_{FH} = \begin{cases} \sqrt{\frac{f'}{4f_l}}, & f' < f_l \\ \sqrt{\frac{1}{4} - \sqrt{\frac{f_l}{16f'}}} + \frac{1}{2}, & f' \geq f_l \end{cases} \tag{171}$$

where P_{FH} is the probability for the face and head case, f_l is the low confidence cut-off, f' is the normalised confidence of the face detection based on the overlapped area a_o, face area a_f and head area a_h.

For the face and shoulder, and the head and shoulder cases, Gaussian probability distribution function is applied to find the best pair of blobs. This is done by examining all pairs with five types of confidence measures, as list in Table VI, where δ and σ are the desired output and standard deviation for each of the confidence measures, respectively, x and y are the horizontal and vertical centroid positions, respectively, w and h are the width and height of the blob, respectively, a is area, φ is the golden ratio, H is the height of the image. Note: δ and σ are selected based on the maximum detectable human size in the image and golden ratio.

TABLE VI CONFIDENCE MEASURES FOR THE FACE AND SHOULDER, AND THE HEAD AND SHOULDER CASES

Type	Confidence Measures	Algebraic Expression	δ	σ
A	Horizontal centroid difference	$x_2 - x_1$	0	$2w_1$
B	Vertical centroid difference over width	$\frac{y_2 - y_1}{w_1}$	φ	φ
C	Height over width	$\frac{h_1}{w_1}$	$\frac{\varphi}{2}$	$\frac{\varphi}{2}$
D	Width ratio	$\frac{w_2}{w_1}$	φ^2	φ^2
E	Area sum	$a_1 + a_2$	$\frac{H^2}{20}$	$\frac{H^2}{20}$

The overall probability is then calculated using (172).

$$P_{FS} = P_{HS} = \prod_{i=1}^{n} e^{-\left(\frac{\eta_i - \delta_i}{\sigma_i}\right)^2} \tag{172}$$

where P_{FS} and P_{HS} are the probabilities for the face and shoulder, and the head and shoulder cases, respectively, η and δ are the actual and desired outputs, respectively, σ is the standard deviation, n is the total number of types.

The results of face, head and shoulder detections are illustrated in Fig. 34 using white, red and yellow rectangles, respectively.

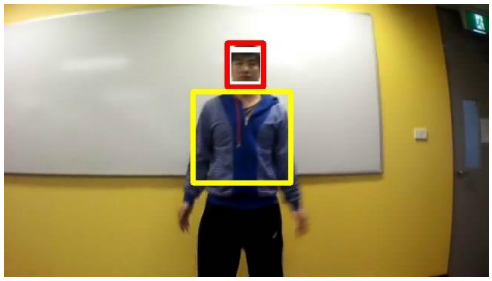

Figure 34 Face, head and shoulder detections

4.1.3 Body Estimation

The third stage of the GHD is the body estimation in which the human body regions are estimated. Firstly, gap detection is performed to locate possible gaps below the armpit and between the legs, these gaps can be assumed as regions with multiple edges and significant orientation changes. This is done similar to the curve detection described earlier in which a gap template is used and it can be represented as a 3 by 3 kernel using (173).

$$G = \begin{bmatrix} \emptyset & -90° & \emptyset \\ \emptyset & \emptyset & \emptyset \\ -26.57° & \emptyset & -153.43° \end{bmatrix} \tag{173}$$

where G is the gap template, $\emptyset$ represents null (element not considered). The values are determined based on their relative angles to an element lays below the kernel.

Correspondingly, the weighted difference between the patch and the template can be determined using (163). The results of the gap detection based on the gap template are then fused together by vertical filling. The weight difference threshold for gap detection is obtained using (174).

$$T_G = 120° - 60°(\omega - 1) \tag{174}$$

where T_G is the maximum weighted difference threshold for gap detection, ω is the scale factor based on the number of blobs formed in the image. Note: the default ω

value is 1, if the total number of blobs found is less than 2, ω is increased by 0.5 and the detection process restarts, ω is capped at 2.

The human body region can then be estimated using eleven overlapping blocks, as shown in Fig. 35. The filled areas in the figure represent detected head and shoulder blobs, the three red blocks (1–3) are the estimated gap regions, while the eight blue blocks (4–11) are the estimated body regions based on Fig. 33. Each block overlaps at least one other region to ensure maximum coverage of the human body.

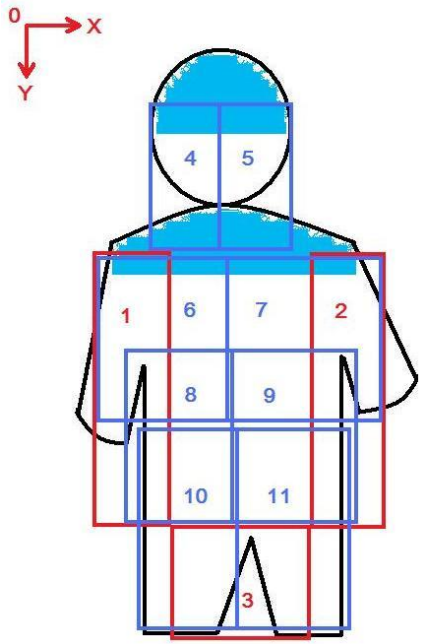

Figure 35 Estimated human body regions (head to knee)

The position and size of the blocks are listed in Table VII, where φ is the golden ratio, i is the block number, X and Y are the horizontal and vertical centroid positions, respectively, w and h are the width and height, respectively, h and s represent head and shoulder, respectively, G_1 represents the minimum horizontal position of the gap regions detected in block 1, G_2 represents the maximum horizontal position of the gap regions detected in block 2, G_3 represents the horizontal centroid position of the gap regions detected in block 3. Note: the origin of the image is located at top left corner.

TABLE VII POSITION AND SIZE OF THE ESTIMATED HUMAN BODY REGIONS

i	X_i	Y_i	W_i	H_i
1	$X_h - \frac{W_h\varphi^2}{2}$	$Y_s + \frac{3W_h\varphi^2 - H_s}{4}$	$W_h\varphi(\varphi - 1)$	$\frac{3W_h\varphi^2 - H_s}{2}$
2	$X_h + \frac{W_h\varphi^2}{2}$	$Y_s + \frac{3W_h\varphi^2 - H_s}{4}$	$W_h\varphi(\varphi - 1)$	$\frac{3W_h\varphi^2 - H_s}{2}$
3	X_h	$Y_s + \frac{7W_h\varphi^2 - 2H_s}{4}$	$W_h\varphi$	$\frac{W_h\varphi^2}{2}$
4	$X_h - \frac{W_h}{4}$	$\frac{Y_h + Y_s}{2}$	$\frac{W_h}{2}$	$Y_s - Y_h$
5	$X_h + \frac{W_h}{4}$	$\frac{Y_h + Y_s}{2}$	$\frac{W_h}{2}$	$Y_s - Y_h$
6	$\frac{3G_1 + G_2}{4}$	$Y_s + \frac{2W_h\varphi^2 - H_s}{4}$	$\frac{G_2 - G_1}{2}$	$W_h\varphi^2 - \frac{1}{2}H_s$
7	$\frac{G_1 + 3G_2}{4}$	$Y_s + \frac{2W_h\varphi^2 - H_s}{4}$	$\frac{G_2 - G_1}{2}$	$W_h\varphi^2 - \frac{1}{2}H_s$
8	$\frac{3G_1 + G_2 + 4G_3 - W_h\varphi^2}{8}$	$Y_s + W_h\varphi^2 - \frac{H_s}{2}$	$\frac{W_h\varphi^2 - G_1 + G_2}{4}$	$W_h\varphi^2$
9	$\frac{G_1 + 3G_2 + 4G_3 + W_h\varphi^2}{8}$	$Y_s + W_h\varphi^2 - \frac{H_s}{2}$	$\frac{W_h\varphi^2 - G_1 + G_2}{4}$	$W_h\varphi^2$
10	$G_3 - \frac{W_h\varphi^2}{4}$	$Y_s + \frac{3W_h\varphi^2 - H_s}{2}$	$\frac{W_h\varphi^2}{2}$	$W_h\varphi^2$
11	$G_3 + \frac{W_h\varphi^2}{4}$	$Y_s + \frac{3W_h\varphi^2 - H_s}{2}$	$\frac{W_h\varphi^2}{2}$	$W_h\varphi^2$

The estimated body regions are drawn in Fig. 36, where neck, upper body, lower body and the region in between are represented by green, cyan, blue and magenta rectangles, respectively.

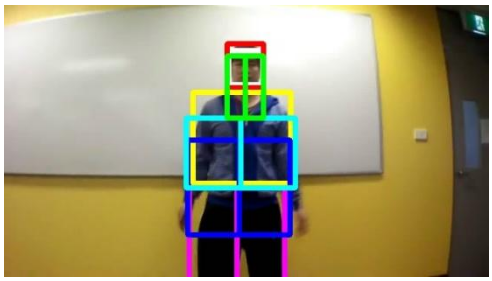

Figure 36 Estimated body regions

4.1.4 Figure Extraction

The fourth and the final stage of the GHD is the figure extraction in which the human figure is extracted and segmented into three parts: head, upper body and lower body. Firstly, The outline of the human body is generated by applying gradient magnitude thresholding with the block regions defined earlier, in which the bottom 75 percentile of the pixels in the block that belong to the gradient magnitude is removed. This is done to preserve key edge features while removing the texture and background noises.

Additional body outlines are also inserted to ensure minimum amount of outlines are available for filling the human figure. This is done by placing hollow circles at the centroids of the head (head blob), neck (blocks 4 and 5), shoulder (shoulder blob), upper body (blocks 6 and 7), lower body (blocks 10 and 11) and the regions in between (blocks 8 and 9). The radii of the circles are determined using (175).

$$R = \frac{\min(W, H)}{2\varphi} \tag{175}$$

where R is the radius, φ is the golden ratio, W and H are the width and height of the regions.

Horizontal filling is then performed by filling the space between the outlines. The human figure is generated by adding the head and shoulder blobs detected earlier while removing the filled gap regions. Finally, based on the estimated human body regions, body segmentation is applied to divide the human figure into three parts: head (head blob, blocks 4 and 5), upper body (shoulder blob, blocks 6 and 7), and lower body (blocks 10 and 11).

The unfilled body outlines and the final segmented body regions are provided in Fig. 37 (a) and (b), respectively. The final segmented results are rendered using red, green and blue colours, representing head, upper body and lower body, respectively.

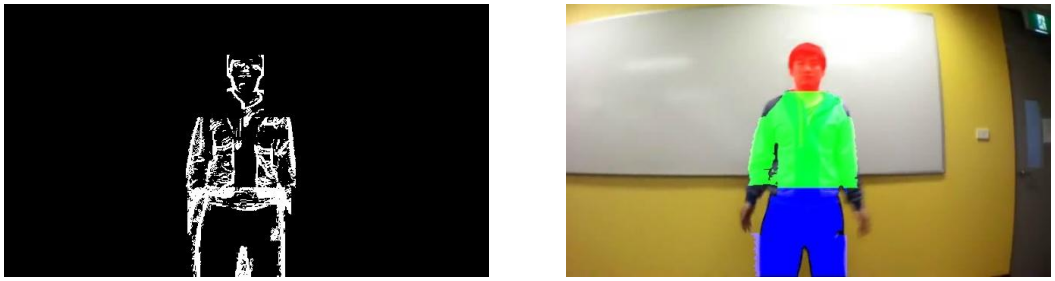

(a) Unfilled body outlines (b) Final segmented body regions

Figure 37 Unfilled body outlines and final segmented body regions

To assess the effectiveness of the proposed GHD method, the method is examined with various images, as shown in Fig. 38. These images are collected from various sources and have different sizes, intensity and quality, from the top to the bottom: the first two images are captured by the front facing camera of the quadrotor used in this research, the next two images are obtained from the INRIA person dataset and the last two images are selected from Google images. In the figure, the original images are shown in (a), the gradient orientation maps are presented in (b), the results of face, head and shoulder detections are illustrated in (c) using white, red and yellow rectangles, respectively, the estimated body regions are drawn in (d), where neck, upper body, lower body and the region in between are represented by green, cyan, blue and magenta rectangles, respectively, the unfilled body outlines are provided in (e) and the final segmented body regions are rendered in (f) with red, green and blue representing head, upper body and lower body, respectively.

As it can be seen from the figures, face detection (white rectangles) has failed to find the correct face regions when the person is not facing towards the camera (cases 2 and 5). Despite this, the method is still capable of detecting the person correctly using head and shoulder detections. These results indicate the high effectiveness of the proposed GHD method as the human figure is detected, extracted and segmented accurately.


1(a)

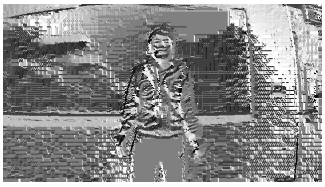
1(b)

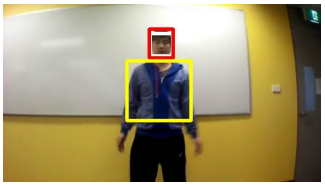
1(c)

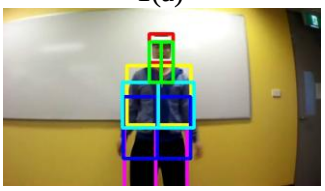
1(d)

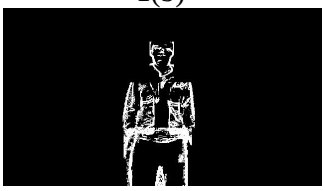
1(e)


1(f)

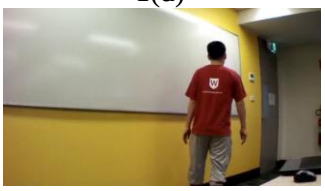
2(a)

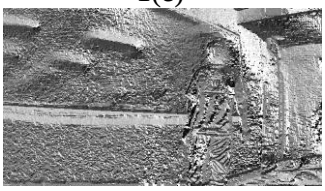
2(b)

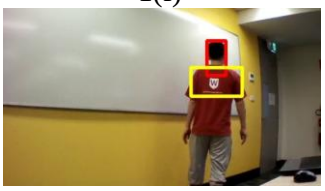
2(c)

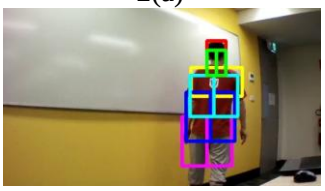
2(d)

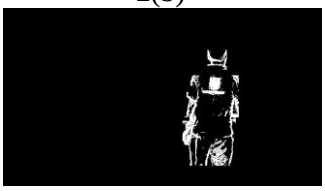
2(e)


2(f)


3(a)


3(b)


3(c)

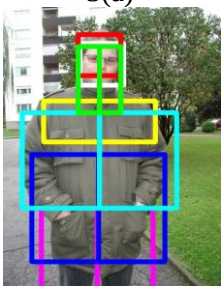
3(d)


3(e)


3(f)


4(a)


4(b)


4(c)

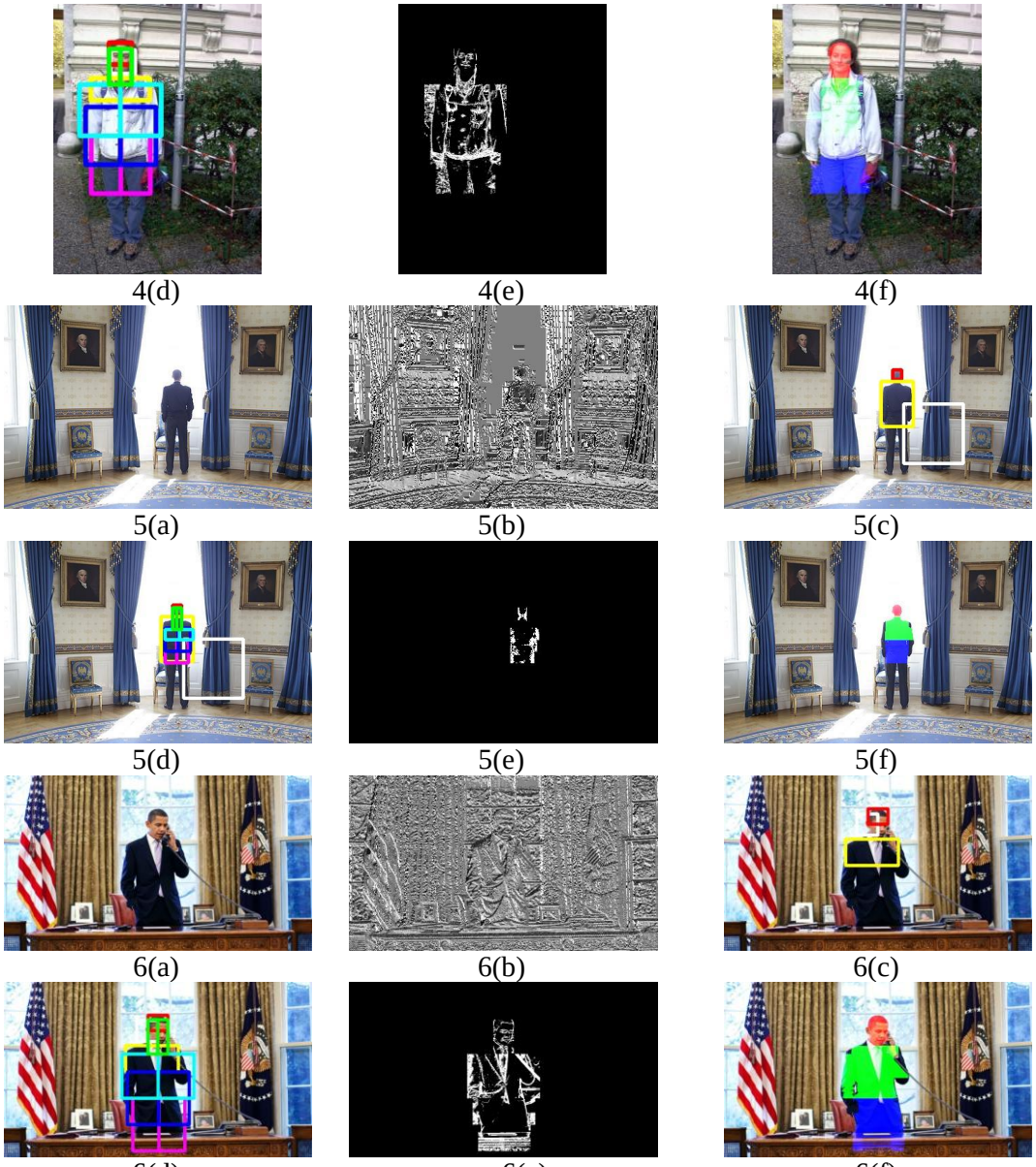

4(d) 4(e) 4(f)

5(a) 5(b) 5(c)

5(d) 5(e) 5(f)

6(a) 6(b) 6(c)

6(d) 6(e) 6(f)

(a) Original input*

(b) Gradient orientation map

(c) Face, head and shoulder detections

(d) Estimated body regions

(e) Unfilled body outlines

(f) Final segmented body regions

Figure 38 Human detection using GHD with various images

*Original images (based on case number):
3 & 4: *http://pascal.inrialpes.fr/data/human*
5: *http://img.timeinc.net/time/photoessays/2009/100_days_callie/obama_100days_49.jpg*
6: *https://peopledotcom.files.wordpress.com/2017/10/obama-oval-office.jpg*

4.2 An Object Tracking Method

Currently, object tracking can be divided into two groups: learning based and non-learning based, learning based methods tend to yield better results in noisy conditions, but suffer from high computational cost. On the other hand, non-learning methods usually perform well in constrained environments, but tend to be application specific. In this section, a generic and non-learning approach is proposed to track an object continuously and robustly in real time without prior training. This is done by combining intensity template matching with colour histogram model and employing a three-tier system for template management.

The proposed object tracking method is named the Tiered Template based Tracking (TTT). It involves three key stages: detection, update and tracking. Templates are used for all the stages to store and compare ROIs. They are organised into three tiers: tier 1 represents stable templates (usually large ROIs that contain the full object), they are rarely updated, tier 2 represents unstable templates (usually medium ROIs that contain part of the object), they are frequently updated and tier 3 represents temporary templates (usually small ROIs that may or may not contain part of the object), they are updated every frame. Initially, when the target ROI is provided manually or acquired automatically (for example, through human detection), it is immediately saved into tier 1. Detection checks for similar ROIs based on the templates, update policy decides the inclusion of templates based on the detected ROIs and tracking policy chooses the most suitable ROI to track.

4.2.1 Detection

The first stage of TTT is detection, for each frame, detection is called first to find similar ROIs based on the templates. All the templates in the three tiers are checked against the image using sliding window approach. Tiers are checked from the top to the bottom, for each tier, templates are checked in the order of time, when a template is found, any remaining templates are skipped and the checking procedure restarts from the next tier. Similarity is determined based on intensity template matching

using Normalised Cross Correlation (NCC) [121] and colour histogram model using Normalised Back Projection (NBP) [122].

For each template, NCC is applied to produce an intensity probability map by computing similarity in the intensity channel between the current template and the ROI in the current search window, as given in (176) to (178).

$$\alpha = \sum_{u,v} \left(t_{u,v} - \bar{t}\right)\left(w_{u,v} - \bar{w}\right) \tag{176}$$

$$\beta = \sqrt{\sum_{u,v} \left(t_{u,v} - \bar{t}\right)^2 \sum_{u,v} \left(w_{u,v} - \bar{w}\right)^2} \tag{177}$$

$$I_{x,y} = \frac{\alpha + \beta}{2\beta} \tag{178}$$

where I is the intensity probability of template t matches with the ROI in the current search window w, (x, y) is the global position within the image and (u, v) is the local position within the current template and search window, $\bar{t}$ and $\bar{w}$ are the mean intensity values of the template and the ROI in the current search window, respectively.

Colour probability maps are also obtained, this is done by computing similarity in the RGB channels using NBP, as given in (179).

$$C_{x,y} = \min\left(\frac{\sum_{u,v} f_{R_{u,v},G_{u,v},B_{u,v}}}{\sum_{u,v} f_{r_{u,v},g_{u,v},b_{u,v}}}, 1\right) \tag{179}$$

where C is the colour probability, (x, y) is the global position within the image and (u, v) is the local position within the current template and search window, (R, G, B) and (r, g, b) are the corresponding RGB bin positions of the image and the template, respectively, f is the corresponding RGB bin value of the template based on the bin position.

The combined intensity and colour probability map is then determined, as given in (180) and (181).

$$\gamma = \bar{f} T_1 \tag{180}$$

$$P = I(1 - \gamma) + \gamma C \tag{181}$$

where P is the combined probability, I and C are the intensity and colour probabilities, respectively, $\bar{f}$ is the mean of the corresponding RGB bin values based on the bin positions of the template, T_1 is a colour weight constant.

A good match requires a high similarity between the currently compared ROIs and low similarity with other ROIs. Therefore, detection is counted as successful if the maximum combined probability of a ROI is high and salient compared to the rest of the image, this is represented using two conditions, as given in (182) and (183).

$$P_1 \geq T_2 \tag{182}$$

$$\min\left(\frac{P_1 - P_2}{1 - P_1}, I_1, C_1\right) \geq T_3 \tag{183}$$

where P_1 and P_2 are the maximum and second maximum combined probabilities, respectively, I_1 and C_1 are the intensity and colour components of the first maximum, respectively, T_2 is a probability threshold constant, while T_3 is a saliency threshold constant. When finding the second maximum, neighbouring regions connected to the first maximum are excluded by masking out the surrounding ROIs and itself (a 3 by 3 ROI mask centred on the first maximum).

4.2.2 Update

The second stage of the TTT is update. Update is performed after the detection stage to include new templates and to replace old ones in the three tiers when necessary. During the update, if the detected ROI is deemed suitable for template inclusion, it is added into the corresponding tier. Similarity checks are performed between the ROI and all the templates in the current tier using (176) to (182). If any of the checks

returns a probability less than T_2, then the least similar one is replaced, if all the templates passed the similar check and the tier is full, the corresponding template found in the detection stage is replaced, else the ROI is added as a new template. Templates in the tier are then rearranged in the order of time. Tier 1 is regarded as the stable tier, it is rarely updated. Tier 2 is regarded as the unstable tier, in which whenever a template is updated, its size is also checked and readjusted if a larger or smaller template produces a more reliable result. Tier 3 is regarded as the temporary tier, in which if none of the templates in tier 3 are updated, all of them are removed.

An update policy is used to decide the inclusion of templates, the conditions are listed in Table VIII. These conditions are established based on general observations. For example, template in tier 2 is updated when detection is found in tier 1 but not in tier 2.

TABLE VIII UPDATE POLICY

Update Tier	Detected Tier	Additional Conditions
1	1&2	$!O_{1,2}\&(Q_2 \geq Q_1)\&(p_2 > p_1)$
2	1&2	$!O_{1,2}\&!(Q_2 \geq Q_1 \& p_2 > p_1)$
2	1&!2	
2	2	$(Q_m \geq Q_1 T_3)\&(2p_m - 1 \geq T_2)$
3	!1&2&!3	$S_{1,2}$
3	!1&2&3	$O_{2,3}$

where & and *!* represent the AND and NOT logic operations, respectively, p is the probability of the detected ROI based on the corresponding template, S is the similarity check explained previously to compare between the detected ROIs, O is an overlap check which is used to determine if the detected ROIs overlap with each other and is given in (184), Q is a colour quality measurement based on hue and chroma which is given in (185) and (186), p_m is the maximum probability given in (187), Q_m is the colour quality measurements using the template with the maximum probability.

$$\frac{W_{ij}H_{ij}}{\min(W_i, W_j)\min(H_i, H_j)} \geq T_4 \tag{184}$$

$$c = \max(r, g, b) - \min(r, g, b) \tag{185}$$

$$Q_i = \min\left(\frac{\bar{h}_i}{\bar{h}_1}, 1\right)\bar{c}_i \tag{186}$$

$$p_m = \max(p_2, p_2^-, p_2^+) \tag{187}$$

where W_{ij} and H_{ij} are the width and the height of the overlap between ROI i and j, respectively, W_i, H_i and W_j, H_j are the width and height of ROI i and j, respectively, T_4 is an overlap threshold constant, c is chroma, r, g, b are the RGB values, Q_i is the colour quality measurement of ROI i, $\bar{h}_i$ and $\bar{h}_1$ are the means of the corresponding hue bin values (of the most recently used template in tier 1) based on the bin positions of ROI i and the most recently used template in tier 1, respectively, $\bar{c}_i$ is the mean chroma value of ROI i, p_2, p_2^- and p_2^+ are the probabilities using the template with original, smaller and larger sizes, respectively.

4.2.3 Tracking

The third and the final stage of the TTT is tracking, since there could be multiple detections among the tiers, tracking is implemented to decide the most suitable ROI to track, this is done via a tracking policy, the conditions are listed in Table IX. These conditions are also established based on general observations. For example, template in tier 1 is selected for tracking when detection is found in tier 1 but not in tier 2.The symbols and operators used are defined the same as those in Table VIII.

TABLE IX TRACKING POLICY

Track Tier	Detected Tier	Additional Conditions
1	1&2	$!(!O_{1,2}\&(Q_2 \geq Q_1)\&(p_2 > p_1))$
1	1&!2	
2	1&2	$!O_{1,2}\&(Q_2 \geq Q_1)\&(p_2 > p_1)$
2	!1&2&3	$!O_{2,3}$
2	!1&2&!3	
3	!1&2&3	$O_{2,3}$

The hyperparameters involved in the method are listed in Table X.

TABLE X HYPERPARAMETERS

Constant	Value
Colour weight (T_1)	0.25
Probability threshold (T_2)	0.8
Saliency threshold (T_3)	0.5
Overlap threshold (T_4)	0.25
Number of RGB bins	16
Number of hue bins	12
Width & length increments of template	±5%
Minimum width & length of template	16 pixels
Maximum number of templates in tier 1, 2 and 3	{1, 2, 3}

The values of theses hyperparameters are chosen empirically based on the interpretation of the TTT method. The number of RGB bins is chosen as 16 because typically images are stored in 8 bits with a range of 256 values, this divides the RGB colour space evenly into 16×16×16 uniform cubes. For hue bins, 12 is chosen based on the number of primary, secondary and tertiary colours [113]. RGB can be regarded as the primary colours, 3 secondary colours can be obtained by mixing primary colours and 6 tertiary colours can be obtained by mixing the primary and secondary colours, this divides the hue evenly into 12 colour sectors. For the maximum number of templates in the tiers, several tier structures have been examined, it is found that using a simple structure of {1, 1, 1} is sufficient enough for tracking, higher accuracy can be achieved by increasing the maximum number of templates, but this also increased the computational cost. Using a laptop with 7th generation Intel core processors, structures of {1, 1, 1} and {1, 2, 3} achieved 22 and 16 frames per second with the benchmark videos, respectively.

The proposed TTT method has been examined with various benchmark videos from different datasets and is compared with six other methods, in which three are learning based: TLD [97], OAB [98], LSK [99] and the other three are non-learning based: KNL [100], FRG [101], LSH [102]. Firstly, all seven methods are implemented to test against seven sequences with their default starting ROIs.

Secondly, since an object's ROI can be perceived differently depending on the person, another test is performed with the same sequences but with alternate starting ROIs (of the same objects). Furthermore, to compare the robustness of those methods, additional tests are conducted with the starting ROIs shifted by one pixel (eight tests: one for each direction based on both default and alternate ROIs).

The sequences with their default and alternate starting ROIs along with the tracking frames are shown in Fig. 39, from the top to the bottom: the first four sequences are produced by the author using the front facing camera of the quadrotor used in this research. The next two sequences are listed in the reference [123], the last sequence is obtained from reference [124]. Information about the implementation of these methods can be found in reference [125].

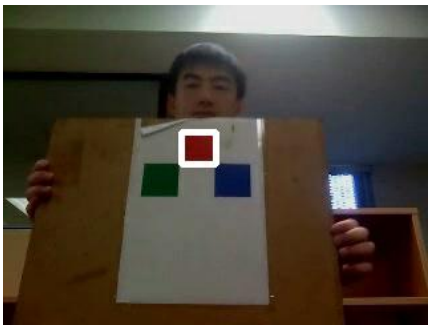

1(a)

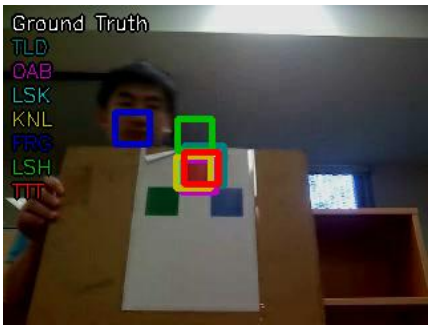

1(b)

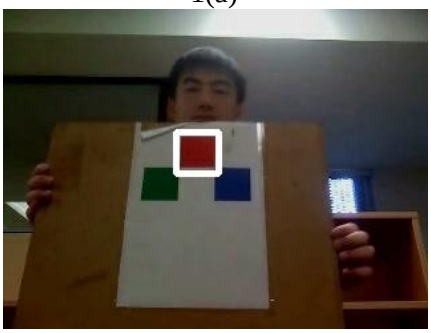

1(c)

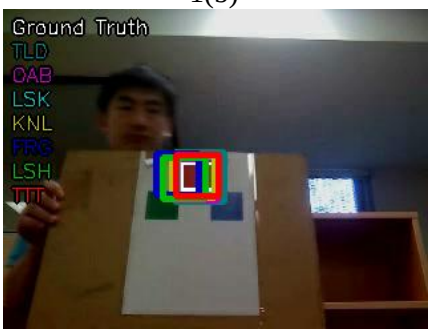

1(d)

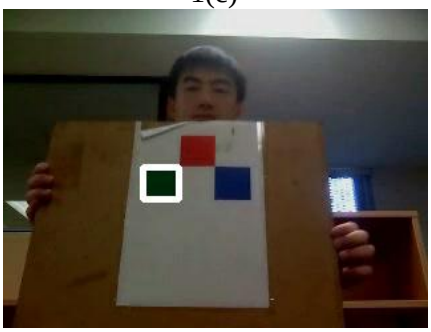

2(a)

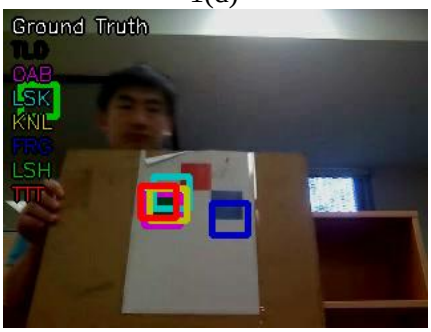

2(b)

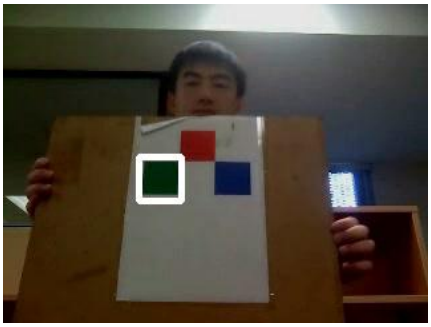

2(c)

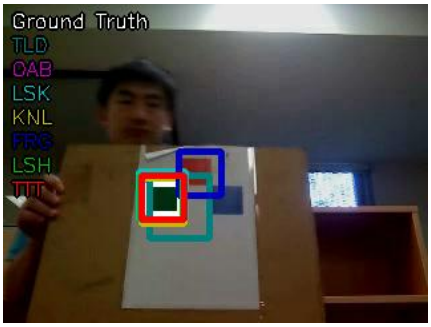

2(d)

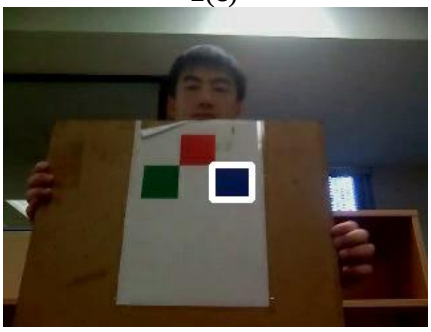

3(a)

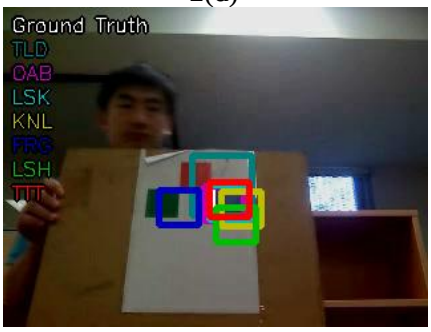

3(b)

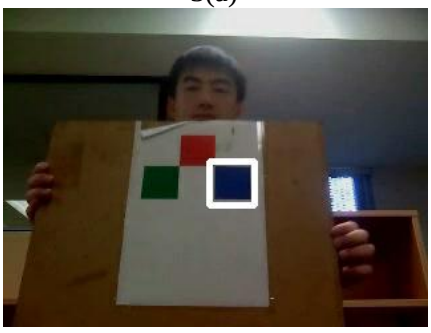

3(c)

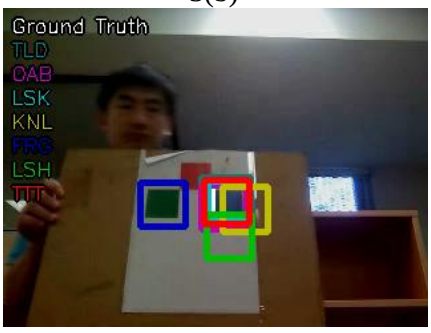

3(d)

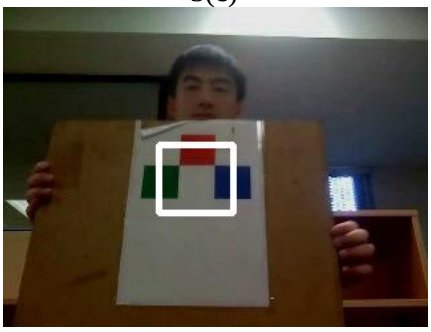

4(a)

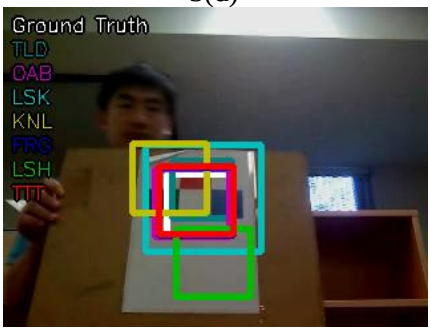

4(b)

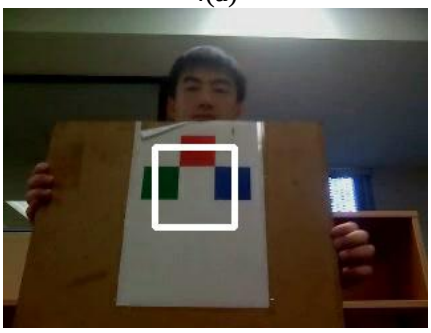

4(c)

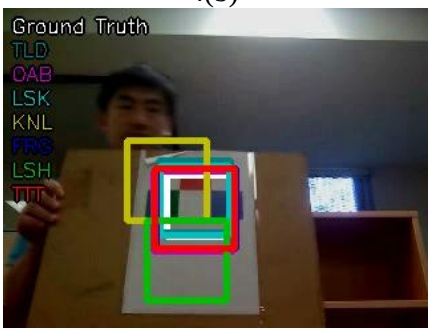

4(d)

5(a)

5(b)

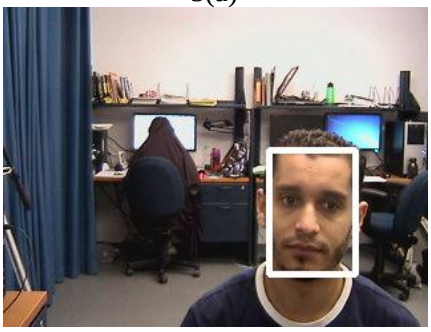

5(c)

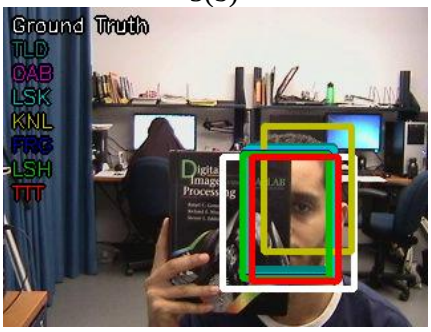

5(d)

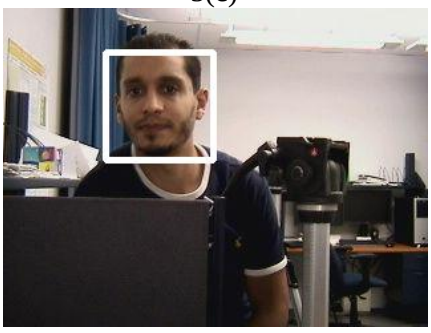

6(a)

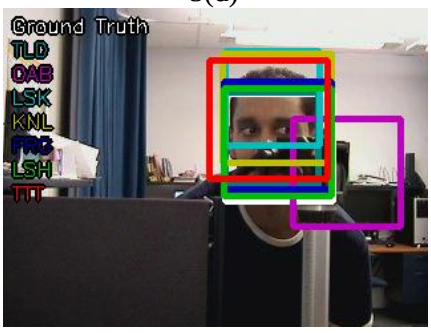

6(b)

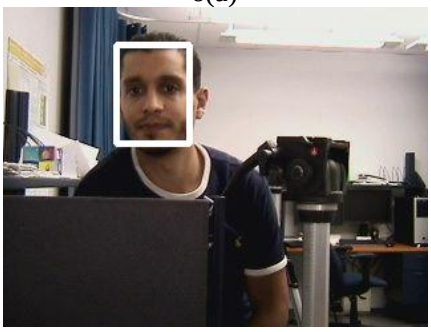

6(c)

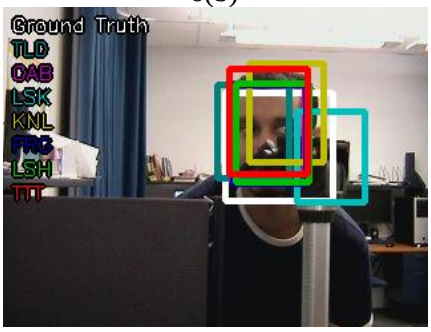

6(d)

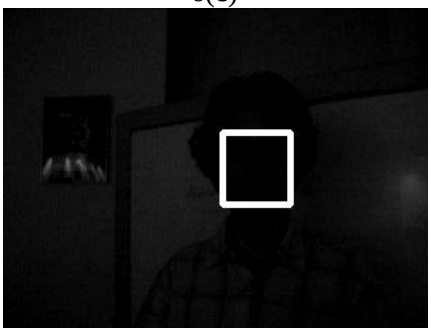

7(a)

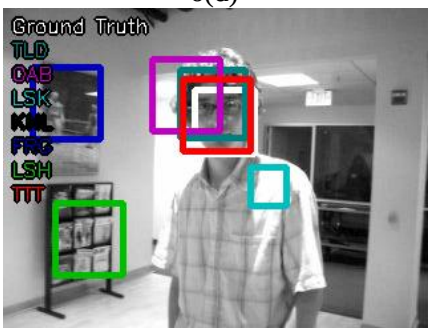

7(b)

7(c) 7(d)

(a) Initial frame with default starting ROI (b) Tracking frame with default starting ROI
(c) Initial frame with alternate starting ROI (d) Tracking frame with alternate starting ROI

Figure 39 Object tracking using GHD with various benchmark videos

Overlap performance evaluation [126] is a common technique to compare the tracking capabilities among different methods. For each frame, the overlap ratio is computed based on intersection over union between the tracked ROI and the ground truth ROI. A percentage threshold (typically 25% or 50%) is then applied to classify the frame into positive (successful) and negative (unsuccessful) groups. The overall performance score is simply the percentage of positive frames.

To illustrate the effectiveness of the methods, resultant curves of all the thresholds with the default, alternate and shifted starting ROIs are shown in Fig. 40. In the figure, the circles represent the most common choices of 25% and 50% threshold values. Note: a threshold of 0 (left most case) means the results is positive as long as an overlapped region exists, while a threshold of 1 (right most case) means the two ROIs need to be identical in order for the results to be counted as positive.

From the results, it can be clearly seen that the proposed TTT method performs superiorly over the existing methods in vast majority of the cases (thresholds of 10% to 90%).

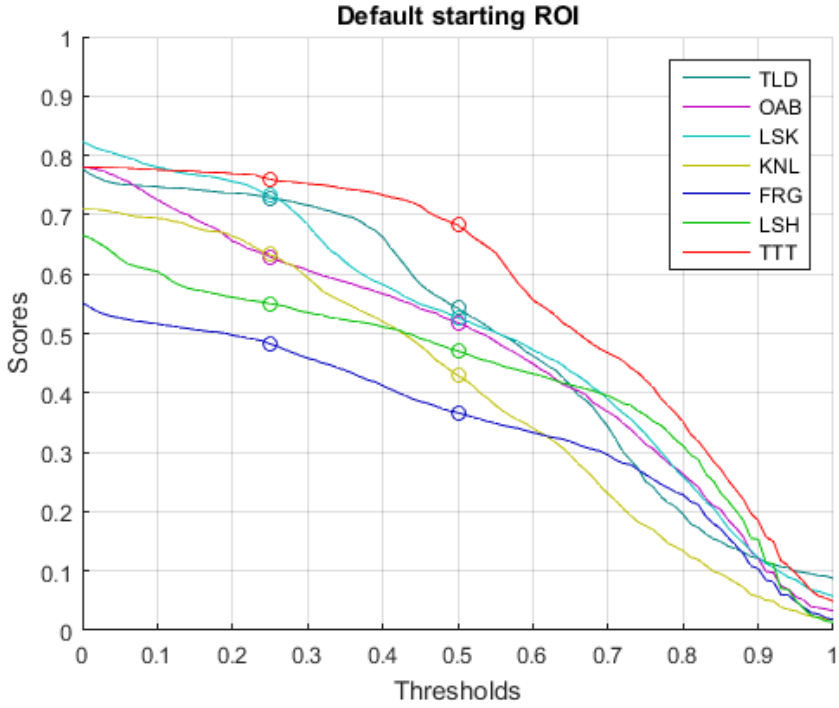

(a) Default starting ROI

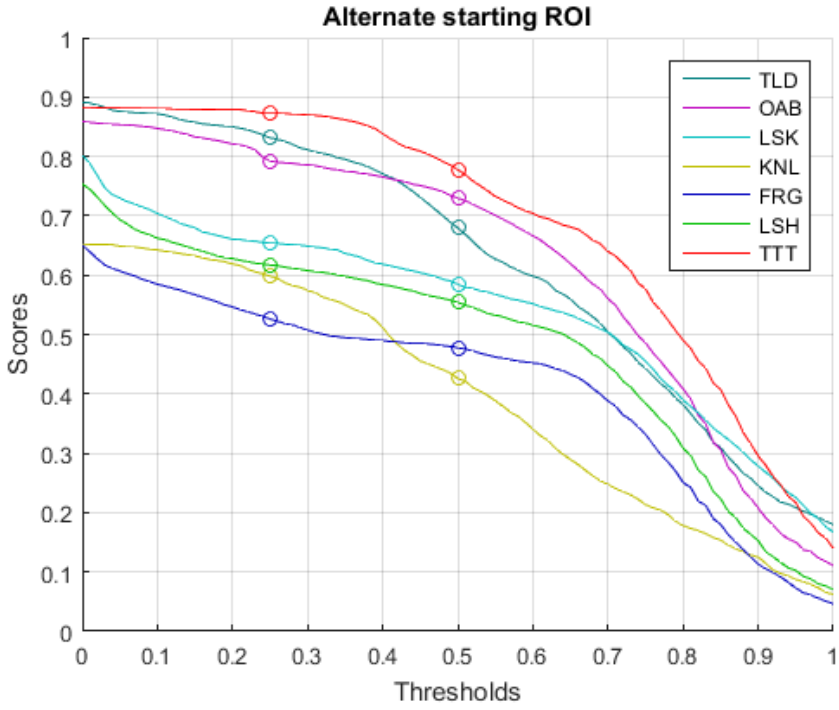

(b) Alternate starting ROI

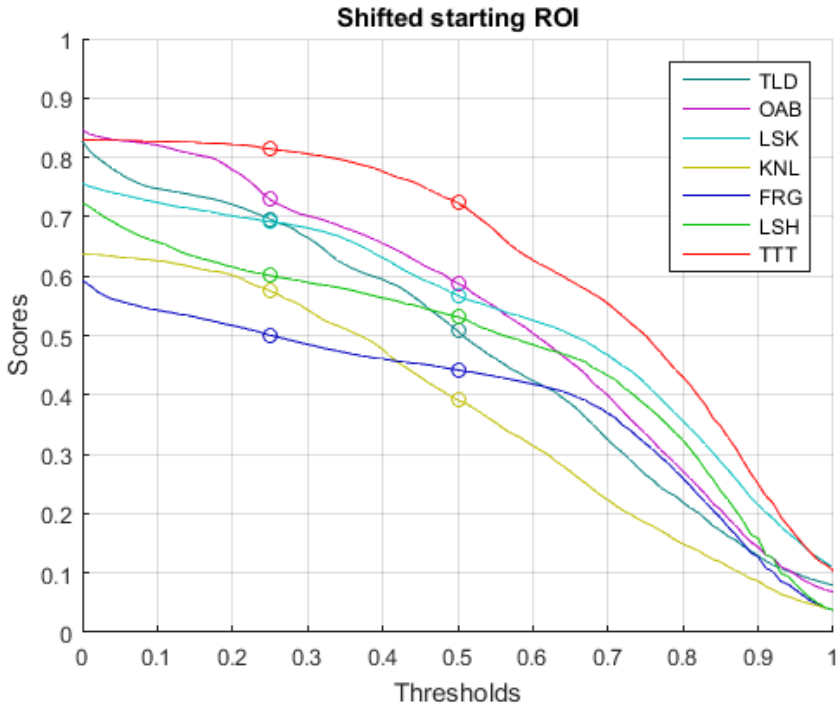

(c) Shifted starting ROI

Figure 40 Mean overlap scores with all thresholds

In summary, this chapter proposed two methods in object detection and tracking: an edge based human detection method (GHD) and template based object tracking method (TTT). The key idea of GHD is to detect the face, head and shoulder of a person separately, this is done mainly using gradient maps. The GHD is able to extract and segment the figure of the human body into key parts with relatively high accuracy and it does not require any prior training to achieve this. However, as the figure with the highest probability is extracted, it only supports single person detections at this stage. On the other hand, the key strategies involved in the TTT are: combining intensity template matching with colour histogram model to increase tracking robustness, employing a three-tier system to store templates, applying update and tracking policies for template management. The TTT method is proven to be fast and accurate, but the memory and computational requirements increases quadratically with increased number of targets. These methods have been implemented into the real-time tracking and pursuit system (Chapter 5). The GHD is employed for target acquisition, while real-time tracking is performed using the TTT.

Chapter 5 Vision Based Target Pursuit Using a UAV

This chapter discusses the proposed target pursuit methods and its related topics. Section 5.1 explains the depth estimation method using the onboard monocular vision. Section 5.2 describes the trajectory mapping method using the onboard sensors of the drone and Section 5.3 provides the results of the target pursuit experiment with three different modes: standby, sentry and search.

5.1 Depth Estimation Using the Onboard Monocular Vision

Depth is an important feature for many practical applications. It is typically obtained through the use of rangefinders such as a sonar sensor, it can also be estimated using cameras. In computer vision, depth estimation is a procedure to recover the depth information from 2D images, this is commonly done using stereovision. However, for small UAVs such as quadrotors, monocular vision based approach is more relevant. This is because compared to monocular vision, the configuration of dual cameras can be inflexible and inconvenient [127]. When a stereo pair is calibrated, it can only work if the target is within certain range of the calibration block, the geometry of the stereo pair also needs to be fixed at all time. Another factor is the limit of payload, most quadrotors can only carry a single camera. Furthermore, stereovision based approaches tend to suffer in operation speed due to high computational cost [128].

Generally, camera needs to be calibrated in order to recover the depth information. Camera calibration is the process of finding the true parameters of the camera used, these parameters can be divided into intrinsic and extrinsic parameters [129]. The intrinsic parameters consist of the focal length, location of the image centre, the skew and distortions, while the extrinsic parameters consist of the rotation and translation matrices, as given in (188) to (196).

$$s\begin{bmatrix} u \\ v \\ 1 \end{bmatrix} = If\left(E\begin{bmatrix} x \\ y \\ z \\ 1 \end{bmatrix}\right) \tag{188}$$

$$I = \begin{bmatrix} \alpha_x & \gamma & c_x \\ 0 & \alpha_y & c_y \\ 0 & 0 & 1 \end{bmatrix} \tag{189}$$

$$E = TR = \begin{bmatrix} 1 & 0 & 0 & T_x \\ 0 & 1 & 0 & T_y \\ 0 & 0 & 1 & T_z \\ 0 & 0 & 0 & 1 \end{bmatrix}\begin{bmatrix} R_{1,1} & R_{1,2} & R_{1,3} & 0 \\ R_{2,1} & R_{2,2} & R_{2,3} & 0 \\ R_{3,1} & R_{3,2} & R_{3,3} & 0 \\ 0 & 0 & 0 & 1 \end{bmatrix} \tag{190}$$

$$f\left(E\begin{bmatrix} x \\ y \\ z \\ 1 \end{bmatrix}\right) = f\left(\begin{bmatrix} x' \\ y' \\ z' \end{bmatrix}\right) = \begin{bmatrix} x'' \\ y'' \\ 1 \end{bmatrix} \tag{191}$$

$$\begin{bmatrix} x' \\ y' \\ z' \end{bmatrix} = \begin{bmatrix} R_{1,1} & R_{1,2} & R_{1,3} & T_x \\ R_{2,1} & R_{2,2} & R_{2,3} & T_y \\ R_{3,1} & R_{3,2} & R_{3,3} & T_z \end{bmatrix}\begin{bmatrix} x \\ y \\ z \\ 1 \end{bmatrix} \tag{192}$$

$$\begin{bmatrix} x'' \\ y'' \end{bmatrix} = \begin{bmatrix} 3r_2\left(\frac{x'}{z'}\right)^2 + \left(t + 2r_1\left(\frac{y'}{z'}\right) + 1\right)\left(\frac{x'}{z'}\right) + r_2\left(\frac{y'}{z'}\right)^2 \\ 3r_1\left(\frac{y'}{z'}\right)^2 + \left(t + 2r_2\left(\frac{x'}{z'}\right) + 1\right)\left(\frac{y'}{z'}\right) + r_1\left(\frac{x'}{z'}\right)^2 \end{bmatrix} \tag{193}$$

$$t = t_3\sigma^3 + t_2\sigma^2 + t_1\sigma \tag{194}$$

$$\sigma = \left(\frac{x'}{z'}\right)^2 + \left(\frac{y'}{z'}\right)^2 \tag{195}$$

$$s\begin{bmatrix} u \\ v \\ 1 \end{bmatrix} = \begin{bmatrix} \alpha_x & \gamma & c_x \\ 0 & \alpha_y & c_y \\ 0 & 0 & 1 \end{bmatrix}\begin{bmatrix} x'' \\ y'' \\ 1 \end{bmatrix} \tag{196}$$

where I and E are the intrinsic and extrinsic matrices, respectively, (u,v) and (x,y,z) are the locations of the points in the image plane and the Cartesian space, respectively, R and T are the rotation and translation matrices, respectively, $R_{1,1}$ to $R_{3,3}$ are the rotation parameters, T_x, T_y and T_z are the translation parameters with respect to x, y and z axes, s is the arbitrary scale factor, γ is the skew factor, α_x and α_y are the focal lengths along x and y components, respectively, c_x and c_y are the x and y locations of image centre, respectively, f represents the distortion function, superscript ‘ represents components of undistorted coordinate vector, while

superscript ‘′ represents components of distorted coordinate vector, r_1 and r_2 are the radial distortion parameters, t_1, t_2 and t_3 are the tangential distortion parameters.

For the depth estimation, the most important parameter is the focal length. It is typically estimated by comparing the detections of a template between different camera positions. A common template to use is the black and white chess board [129], the template needs to be detected by the camera from at least three different positions, this can be done either by moving the camera or the template. The focal length is obtained by solving the homography equations between the model plane and its image. This approach can provide accurate estimation, however it can be computationally expensive as the number of view increases, since the estimation of the homography equations for each view is an iterative non-linear procedure. Additionally, successful estimation of the focal length is not guaranteed as large distance or parallel orientation of the template tends to cause singularity.

Another possible template is scalene triangle [130]. In this approach, the template plane is moved vertically parallel to the camera plane multiple times, the distances between the template and camera planes are recorded for every movement. Sobel edge detector [33] is then applied, followed by extraction of the vertices of the triangles. Finally, estimation of intrinsic parameter is done through matching of the locations of these vertices. This approach can also achieve reasonably good estimation accuracy, but the procedure is inconvenient to perform as each movement requires precise alignment between the template and camera planes.

In this research, a simple procedure is implemented to recover the focal length of the front facing camera of the quadrotor using a colour template. This depth calibration procedure only needs to be conducted once per camera, the template is given in Fig. 41.

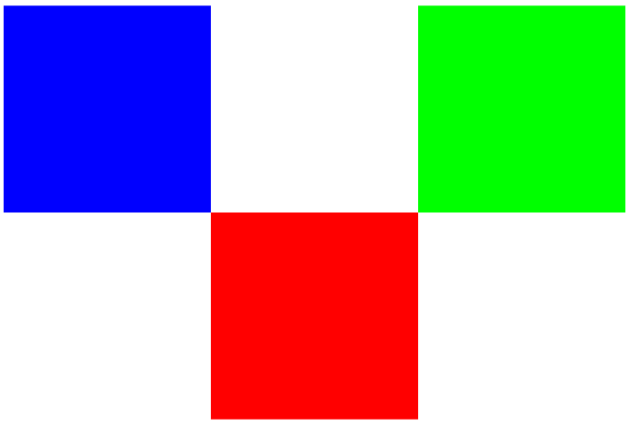

Figure 41 Depth estimation template

As shown in the figure, this is a very simple template that can be easily created and printed on a paper. For the three squares in the template, red square is the intended target, blue and green squares are employed for alignment purpose only, so that the image plane is parallel to the template plane. The size of each square should be the same, but their combined area can vary. In the experiment, the template is printed on an A4 paper, the actual physical size of each square is 55 ×55 millimetres.

The procedure involves facing the camera to the template (aim at the centre of the red square) and moving the drone some distance to the template (either towards or away from the template). After the movement, simply record the height of the red square appeared in the image in pixels. The focal length can be recovered by repeating the steps several times. The basic principle of the proposed depth estimation approach is given in Fig. 42, where C_1 and C_2 are the two different camera positions, respectively, h_1 and h_2 are the detected heights in pixels of the target, respectively, D is the depth, H is the actual physical width, f is the focal length.

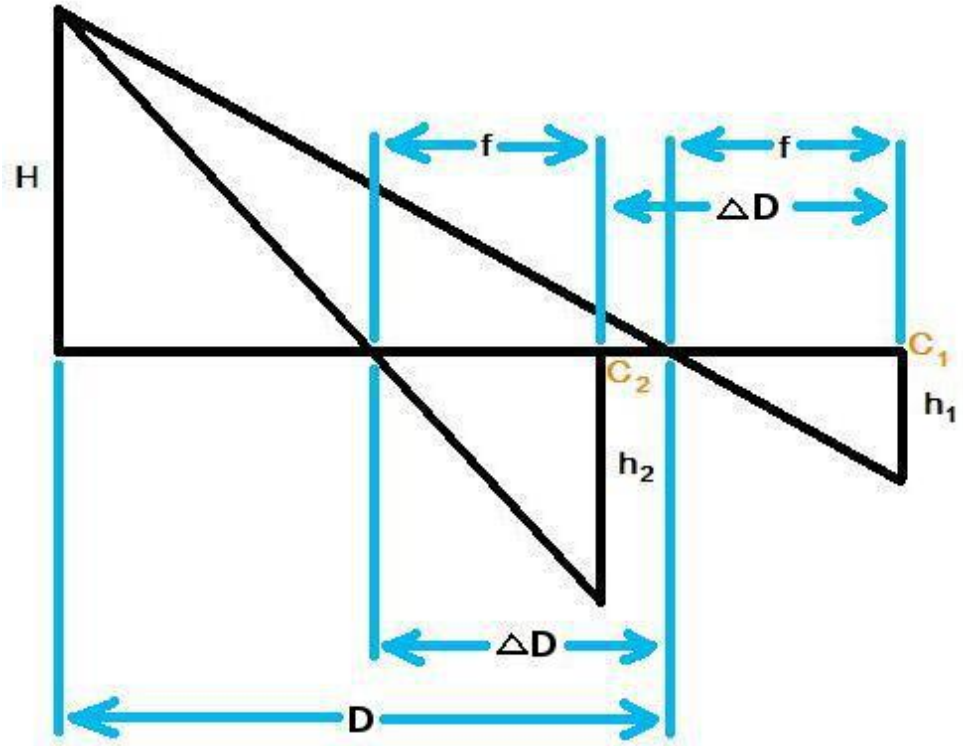

Figure 42 Basic principle of the proposed depth estimation procedure

By using the properties of similar triangles, two equations can be established for a single movement, as given in (197) and (198).

$$\frac{f}{D} = \frac{h_1}{H} \tag{197}$$

$$\frac{f}{D - \Delta D} = \frac{h_2}{H} \tag{198}$$

By rearranging the equations and adding more measurements, a single equation can be obtained to recover the focal length, as given in (199).

$$f = \frac{1}{n}\sum_{i=2}^{n+1} \frac{h_i h_{i-1} \Delta D}{H|h_i - h_{i-1}|} \tag{199}$$

where h_i is the image height in pixels of the i^{th} measurement, H is the actual physical height, f is the focal length, n is the total number of movements, D is the depth.

An example frame of the focal length recovery procedure is given in Fig. 43. In the figure, *r*, *g* and *b* represent the red, green and blue squares, respectively, *x* and *y* are the image width and height of the squares in pixels. Note: the original resolution of the frame is 360×640. For best results, the height of the red square should only be recorded if the camera is aligned with the template, in which the width and height of green and blue squares match with each other (i.e. $gx = bx$ and $gy = by$).

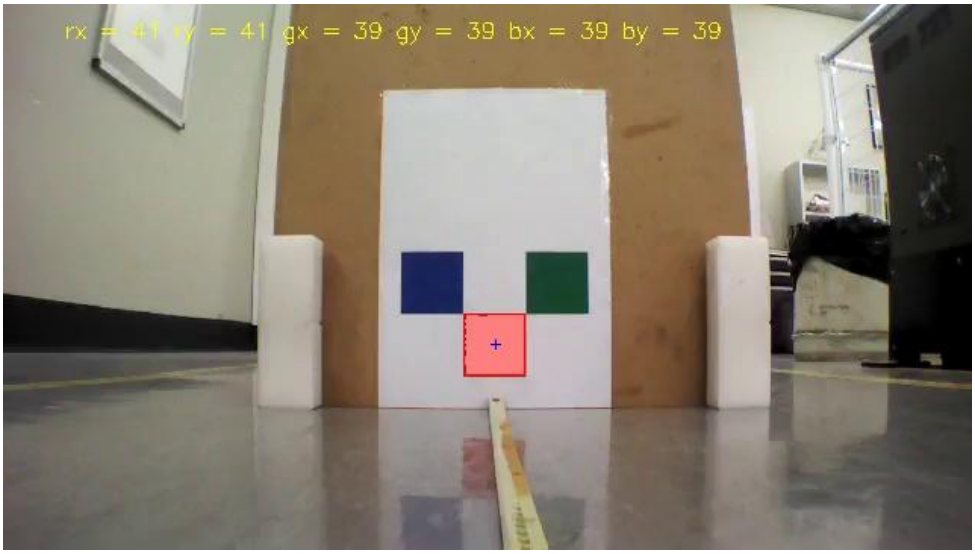

Figure 43 Example frame of the focal length recovery procedure

In the experiment, the drone is moved 20 times (21 measurements recorded). The image height of the red square detected using the camera is listed in Table XI, where h_i is the image height of the red square for i^{th} measurement. The distance of every movement is 50 millimetres, focal length is estimated to be approximately 557 pixels after 20 movements with 18 out of 20 applicable computations using (199). The two non-applicable cases are produced because the detected image height did not change during these two movements (division by zero error), this could be due to human error and the fact that the actual physical size of the square might be too small for the camera to detect.

TABLE XI FOCAL LENGTH ESTIMATION BASED ON IMAGE HEIGHT

i	h_i	f_i	i	h_i	f_i	i	h_i	f_i
1	25	-	8	37	381	15	61	621
2	25	-	9	39	656	16	68	539
3	28	212	10	41	727	17	79	444
4	30	381	11	43	801	18	87	781
5	31	845	12	48	375	19	101	571
6	34	319	13	51	742	20	121	556
7	34	-	14	56	519	21	151	554

Once the focal length is recovered, depth can be simply estimated using (200). Note: this is assuming the target object is near the centre of the camera, therefore the equation is only suited for a small area of viewing. During the pursuit, the drone is programmed to converge the target's position to the centre of the camera.

$$D = f\frac{H}{h} \tag{200}$$

where H and h are the physical and image height of the target, respectively, f is the focal length and D is the estimated depth.

The results and errors of depth estimation are shown in Fig. 44. In the figure, the results of depth estimation based on 20 movements are shown in (a), where blue line is the actual distance which is obtained through measurement using a ruler, while the red line is the estimated distance using the recovered focal length. The errors of depth estimation based on 20 movements are also given in (b). Additionally, a progressive plot of mean absolute errors as the number of movements increases is provided in (c). As expected, the mean absolute error decreases as the number of movements increases, it converges to approximately 1.7% after 20 movements. Note: due to the low resolution of the camera, the actual measurements contain noises.

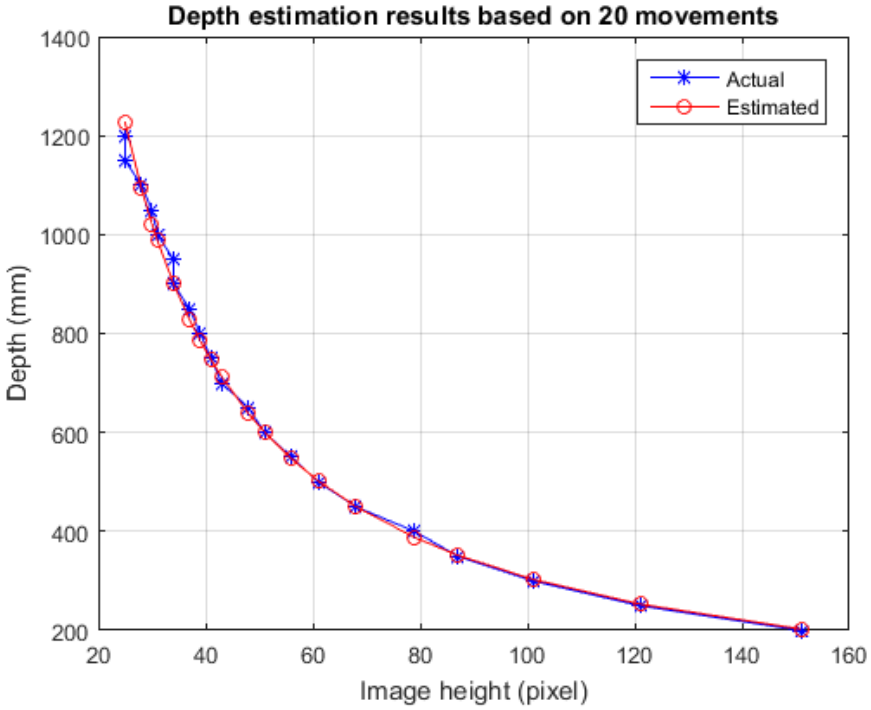

(a) Results based on 20 movements

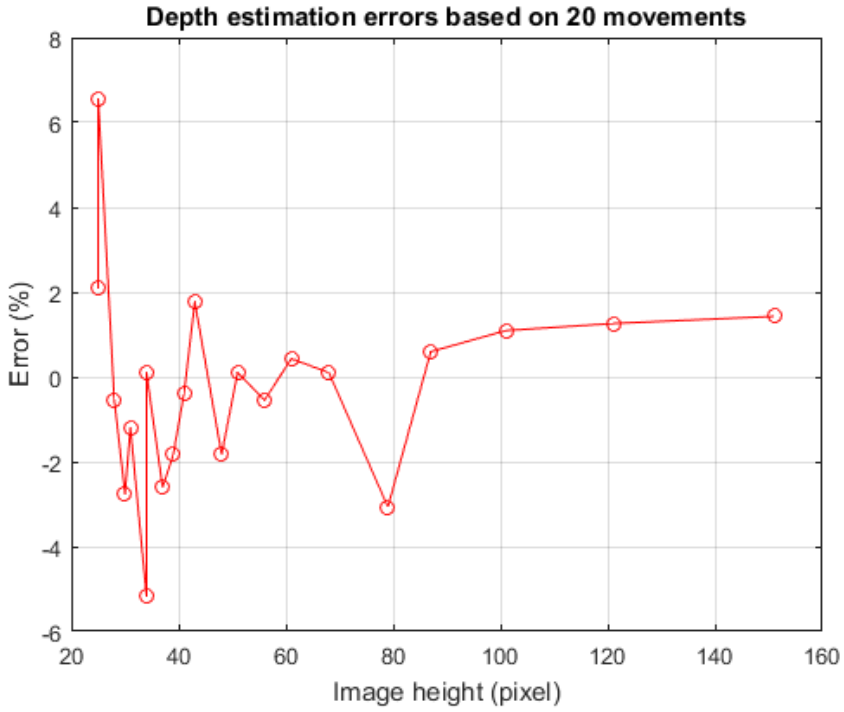

(b) Errors based on 20 movements

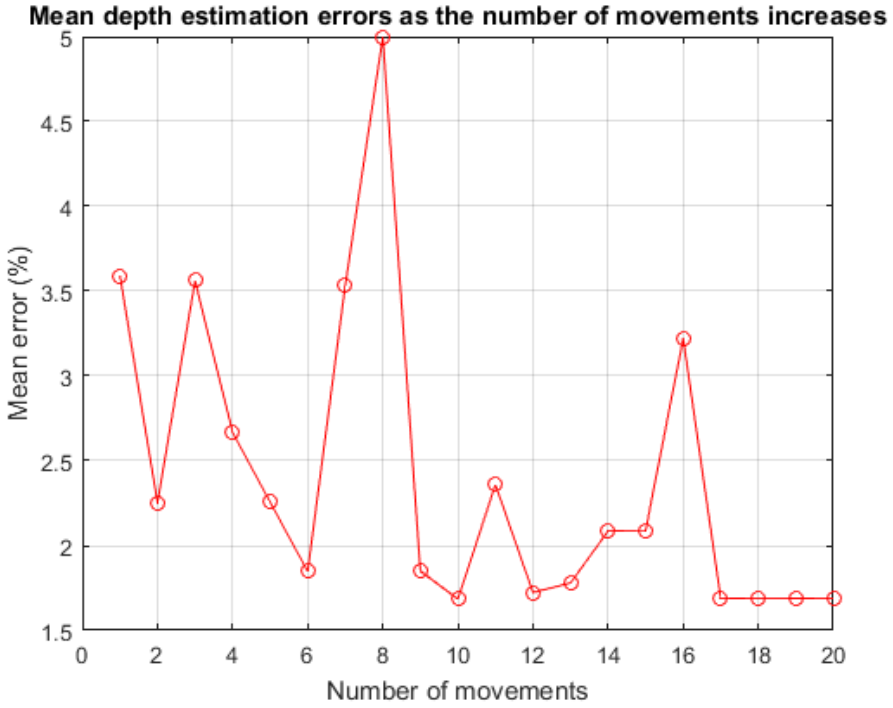

(c) Mean absolute errors as number of movements increases

Figure 44 Depth estimation results and errors

5.2 Trajectory Mapping

Since the drone is only equipped with INS (without GPS), the position is mapped by computing the displacement using dead reckoning based on roll, pitch and yaw angles, as given in (201) to (206).

$$R_\alpha = \begin{bmatrix} 1 & 0 & 0 \\ 0 & \cos\alpha & -\sin\alpha \\ 0 & \sin\alpha & \cos\alpha \end{bmatrix} \tag{201}$$

$$R_\beta = \begin{bmatrix} \cos\beta & 0 & \sin\beta \\ 0 & 1 & 0 \\ -\sin\beta & 0 & \cos\beta \end{bmatrix} \tag{202}$$

$$R_\gamma = \begin{bmatrix} \cos\gamma & -\sin\gamma & 0 \\ \sin\gamma & \cos\gamma & 0 \\ 0 & 0 & 1 \end{bmatrix} \tag{203}$$

$$P = \begin{bmatrix} P_x \\ P_y \\ P_z \end{bmatrix} \tag{204}$$

$$V = \begin{bmatrix} V_x \\ V_y \\ V_z \end{bmatrix} \tag{205}$$

$$\Delta P = R_\alpha R_\beta R_\gamma V \Delta t \tag{206}$$

where α, β and γ are the roll, pitch and yaw angles, R is the rotation matrix, P and V are position and velocity of the drone, respectively, t is time.

The diagonal angle of view of the camera is listed as 92 °, its aspect ratio is found to be 16:9, the horizontal and vertical angles of view can be determined based on geometry using (207) and (208).

$$\varepsilon_x = 2\tan^{-1}\left(\frac{16\tan\frac{92°}{2}}{\sqrt{16^2+9^2}}\right) \approx 84° \tag{207}$$

$$\varepsilon_y = 2\tan^{-1}\left(\frac{9\tan\frac{92°}{2}}{\sqrt{16^2+9^2}}\right) \approx 54° \tag{208}$$

where ε_x and ε_y are the horizontal and vertical angles of view, respectively.

The default height of the target is set to be 1.75 metres. It can be updated through the height estimation using (209) and (210).

$$\delta = P_z - H_T\frac{5}{2}\left(\frac{\varphi}{3\varphi+1}\right) \tag{209}$$

$$H_T' = \begin{cases} H_T + \delta\left(\frac{1}{2} - \frac{T_y}{h}\right), & \delta > 0 \text{ and } T_y < \frac{h}{2} \\ H_T - \delta\left(\frac{1}{2} - \frac{T_y}{h}\right), & \delta < 0 \text{ and } T_y > \frac{h}{2} \end{cases} \tag{210}$$

where P_z is the altitude of the drone, H_T is the estimated height of the target, φ is the golden ratio, δ is the physical height difference, h is the maximum image height in

pixel, T_y is the vertical centroid position of the upper body belonging to the target in the image. Superscript $'$ indicates the updated value. Note: the origin of the image at top left corner.

The distance to the target is determined based on the depth estimation obtained in (200) and is given in (211).

$$D = f\frac{H_T}{h_T}\left(\frac{\varphi}{3\varphi + 1}\right) \tag{211}$$

where H_T is the estimated height of the target, h_T is the image height of the upper body belonging to the target, φ is the golden ratio, f is the focal length and D is the estimated distance to the target.

The desired clearance to follow the target is also computed which is based on the maximum detectable human size, this is to ensure the key parts of the target are visible to the drone during pursuit, as given in (212).

$$C = \frac{H_T}{2\tan\frac{\varepsilon_y}{2}}\left(\frac{2\varphi + 1}{3\varphi + 1}\right) \tag{212}$$

where H_T is the estimated height of the target, φ is the golden ratio, δ is the physical height difference, ε_y is the vertical angle of view and C is the clearance. The clearance is about 1.25 metres for a 1.75 metres tall person.

Finally, the trajectory of the drone is plotted onto a 250×250 image representing a 10×10 metres map, as shown in Fig. 45. In the figure, the white vertical line from the centre of the map is north, green path is the trajectory of the drone, the white filled circle is the target in pursuit, the red and white unfilled circles are the current and intended positions, respectively, the lines attached to the circles represent visible range of the drone based on the angle of view.

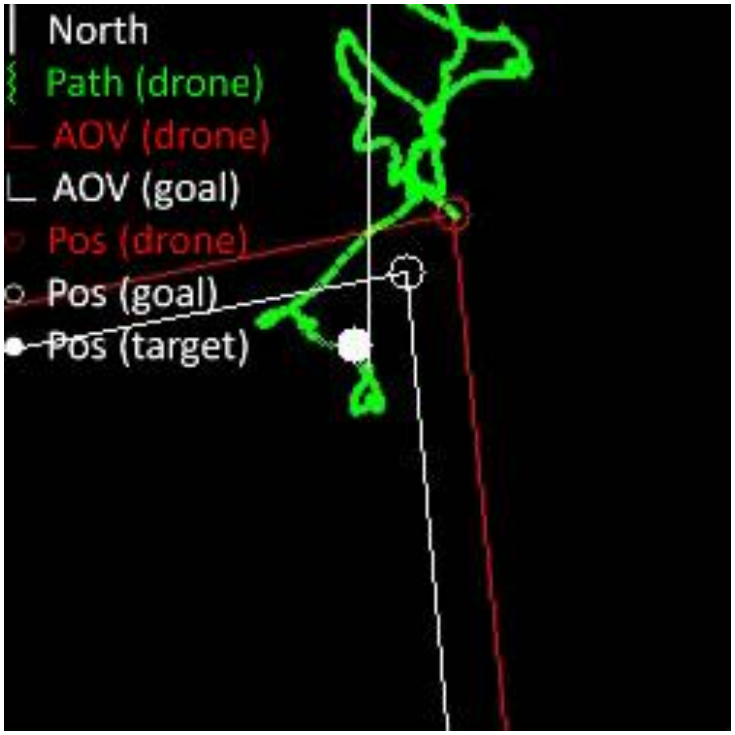

Figure 45 Example trajectory during target pursuit

5.3 The Flight Controller

The quadrotor used in this research is a Parrot AR Drone 2, the drone is originally designed to be controlled only via mobile applications such as FreeFlight[*] on iOS. However, since it does not support advanced capabilities such as image processing, a custom flight controller is built with Microsoft Visual Studio using C++, additional libraries installed are: OpenCV[†], CVDrone[‡], CVBlob[§] and CURL[**]. OpenCV is essential for image processing, CVDrone is necessary for communicating with the drone, CVBlob is helpful for filtering and rendering ROIs, CURL is useful for image fetching and remote control. The drone is controlled through WIFI, in which live video captured using the front facing camera of the drone is sent to a laptop for online processing and the actual controls are then sent back to the drone. The video

[*] *https://itunes.apple.com/app/id373065271*
[†] *https://opencv.org*
[‡] *https://github.com/puku0x/cvdrone*
[§] *https://github.com/emgucv/cvblob*
[**] *https://curl.haxx.se/*

can be streamed at 30 frames per second with 720×1280 resolution, for the tracking and pursuit experiment, the resolution has to be compressed into 180×320 in order to maintain 30 frames per second for online processing. This is due to the fact that the WIFI connection available is not suitable for high resolution video streaming and the laptop is only equipped with a low speed CPU (Intel core 2 Duo).

The flight controller supports three types of controls: keyboard, mouse and text messages. Since the drone itself is a WIFI access point, the actual motion of the drone is controlled by sending specific Attention (AT) commands, AT commands are typically used for communicating with modems. An example of using AT command to control the drone to take-off is:

```
sockCommand.sendf("AT*REF=%d,290718208\r", ++seq);
```

5.3.1 Keyboard

The easiest way to control the drone is via a keyboard, the keyboard controls are listed in Table XII. Note: the autopilot modes listed in the table are to be discussed in detail in Section 5.6.

TABLE XII KEYBOARD CONTROLS

Key	Function	Note
W	Go forward (surge)	Maximum: about 3 metres per second
S	Go backward (surge)	Maximum: about 3 metres per second
A	Shift left (sway)	Maximum: about 3 metres per second
D	Shift right (sway)	Maximum: about 3 metres per second
Z	Climb up (heave)	Maximum: about 1 metre per second
C	Climb down (heave)	Maximum: about 1 metre per second
Q	Rotate anti-clockwise (Yaw)	Maximum: about 120 °per second
E	Rotate clockwise (Yaw)	Maximum: about 120 °per second
X	Switch between cameras	Cameras: front and downward facing
V	Record video: On / Off	
B	Record trajectory: On / Off	
F	Activate autopilot	Deactivate by pressing any other keys
G	Switch between autopilot modes	Modes: standby, sentry and search
Space	Take-off / Land	
Escape	Emergency stop	Send landing command then exit controller

5.3.2 Mouse

The drone can also be controlled via a mouse, this is done by clicking anywhere on the trajectory map which is described earlier in Section 5.4. Mouse control is designed to only output surge translation and yaw rotation, this simplify the required motions to reach the target position, as given in (213) and (217).

$$\gamma_T = \tan^{-1}\left(\frac{Y_T - Y_D}{X_T - X_D}\right) \tag{213}$$

$$\Delta\gamma' = \gamma_T - \gamma_D \tag{214}$$

$$\Delta\gamma = \begin{cases} \Delta\gamma' + 360°, & \Delta\gamma' < -180° \\ \Delta\gamma' - 360°, & \Delta\gamma' > 180° \\ \Delta\gamma', & \text{otherwise} \end{cases} \tag{215}$$

$$R_\gamma = \frac{\Delta\gamma}{360°} \tag{216}$$

$$V_x = \left(\frac{1}{2} - |R_\gamma|\right)^2 \tag{217}$$

where T and D represent the target and the drone, respectively, X and Y are the horizontal and vertical positions on the trajectory map, γ is yaw, V and R are translation and rotation motions, respectively. Note: for safety reason, surge translation is capped at 75 centimetres per second, while yaw rotation is capped at 60 ° per second. R_γ is included in V_x so that yaw rotation has higher priority than surge translation. Superscript $'$ indicates the intermediate value.

5.3.3 Text Messages

Furthermore, the drone can be controlled remotely via text messages, this is achieved by sending specific text to an email address linked with the controller. In this approach, the email is automatically downloaded and read, in which all the texts are scanned for control commands that can trigger the drone to activate and move to a nearby location. However, since the controller also relies on WIFI to communicate with the drone, this means that the text commands can only be received when the drone is not active in which the controller automatically switch WIFI to connect to

the internet. The specific text commands are listed in Table XIII, where each ? represents an input character.

TABLE XIII TEXT COMMANDS

Text	Function
ACTD	Activate drone, must be included first before all other commands
MOVX??Y??	Move (P / N: positive or negative) (0–9) meters along *X* and *Y* directions, only outputs V_x and R_y, similar to mouse control
RECV	Record video
RECB	Record trajectory
AUTO?	Activate autopilot with mode (1–3: standby, sentry and search)

5.4 Autopilot Modes

The flight controller is built with three autopilot modes: standby, sentry and search. In standby mode, the drone takes-off immediately upon receiving a photo of a person and simply hovers until the intended target appears. In sentry mode, the drone is used to monitor an area and is only triggered when the target is detected through its camera. In search mode, the drone patrols in a fixed path continuously while searching for the target. An example third person view of the drone in standby mode is provided in Fig. 46.

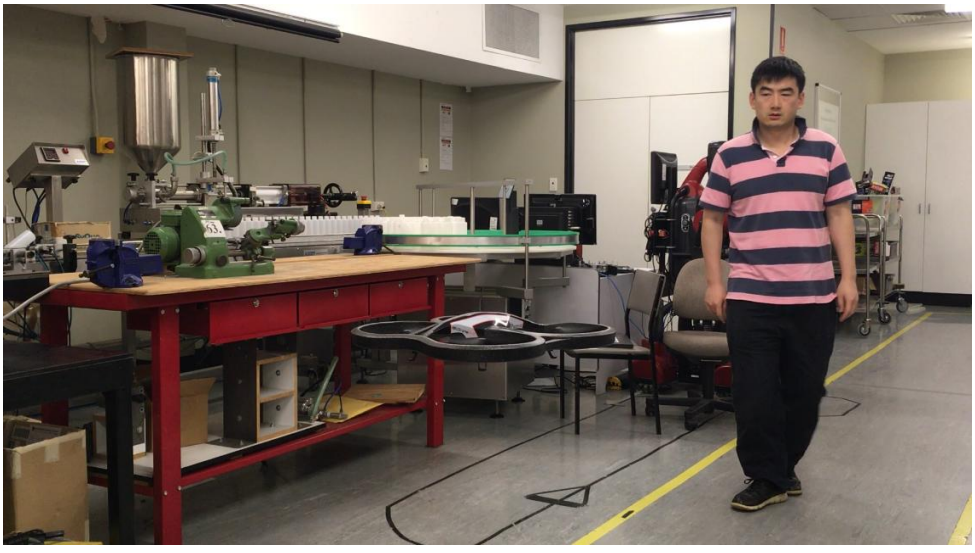

Figure 46 Example third person view of the drone in standby mode

Target pursuit is implemented into all three modes, a flowchart of the system is given in Fig. 47.

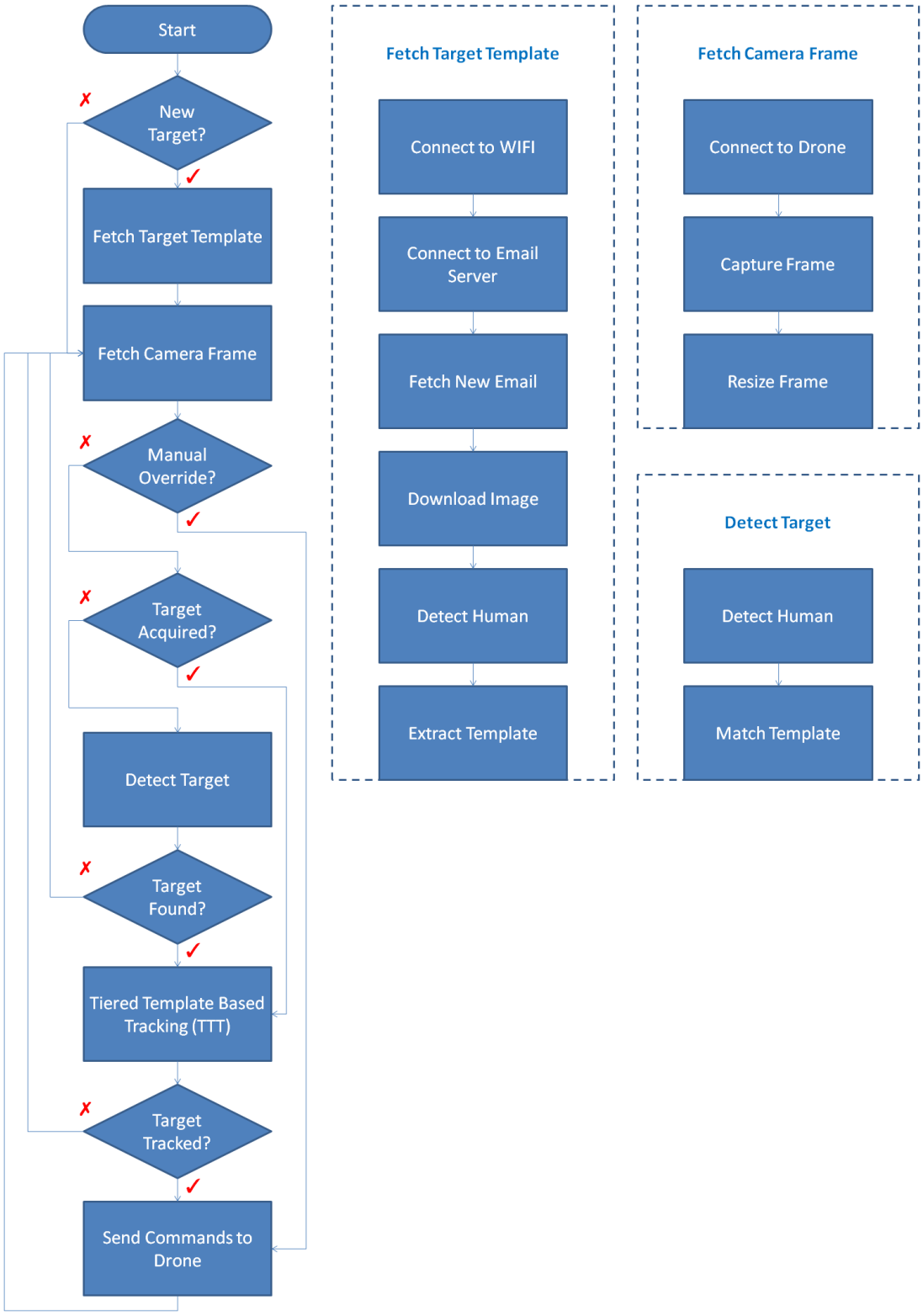

Figure 47 Flowchart of the target pursuit system

Firstly, to fetch the image, the system constantly checks for new emails that contain images, this is done by periodically sending the retrieve command to the email server using the Post Office Protocol (POP). The POP is a common internet standard protocol for communicating with email servers, the POP dialog is shown in Fig. 48. Once an image attached to the email is found, the image data are downloaded automatically. Since all images in emails are encoded with base64, a decoding procedure is needed. Base64 is simply used to convert 8-bits data into 6-bits format, the corresponding characters and their values are listed in Table XIV, where *C* and *i* represent the character and the value, respectively.

TABLE XIV BASE64 CHARACTERS

i	C_i	*i*	C_i	*i*	C_i	*i*	C_i	*i*	C_i	*i*	C_i	*i*	C_i	*i*	C_i
0	A	8	I	16	Q	24	Y	32	g	40	o	48	w	56	4
1	B	9	J	17	R	25	Z	33	h	41	p	49	x	57	5
2	C	10	K	18	S	26	a	34	i	42	q	50	y	58	6
3	D	11	L	19	T	27	b	35	j	43	r	51	z	59	7
4	E	12	M	20	U	28	c	36	k	44	s	52	0	60	8
5	F	13	N	21	V	29	d	37	l	45	t	53	1	61	9
6	G	14	O	22	W	30	e	38	m	46	u	54	2	62	+
7	H	15	P	23	X	31	f	39	n	47	v	55	3	63	/

```
* Connected to pop3.live.com (40.100.151.114) port 995 (#0)
* successfully set certificate verify locations:
*   CAfile: ./ca.crt
  CApath: none
* SSL connection using TLSv1.0 / ECDHE-RSA-AES256-SHA
* Server certificate:
*        subject: C=US; ST=Washington; L=Redmond; O=Microsoft Corporation; CN=ou
tlook.com
*        start date: 2017-09-13 00:00:00 GMT
*        expire date: 2018-09-13 12:00:00 GMT
*        subjectAltName: pop3.live.com matched
*        issuer: C=US; O=DigiCert Inc; CN=DigiCert Cloud Services CA-1
*        SSL certificate verify ok.
< +OK The Microsoft Exchange POP3 service is ready. [TQBFAFgAUABSADAAMQBDAEEAMAA
xADEAMgAuAGEAdQBzAHAAcgBkADAAMQAuAHAAcgBvAGQALgBvAHUAdABsAG8AbwBrAC4AYwBvAG0A]
> CAPA
< +OK
< TOP
< UIDL
< SASL PLAIN
< USER
< .
> AUTH PLAIN
< +
> dXdzdGVzdEBob3RtYWlsLmNvbQB1d3N0ZXN0QGhvdGlhaWwuY29tAFVzZXJuYW1lMTIz
< +OK User successfully authenticated.
> RETR 1
< +OK
* Connection #0 to host pop3.live.com left intact
Fetching Email: Success!
Downloading Attachment: Success!
Decoding Image: Success!
```

Figure 48 POP dialog for image fetching

Human detection using the proposed GHD method described earlier in Section 4.1 is then employed to find the possible human presented in the image. If detection is found, human segmentation is applied to divide the body figure into head, upper body and lower body. The final template is then extracted based on the largest square region centred in the upper body. Two cases with different clothing and background are presented in Fig. 49. In the figure, the original images downloaded from the email is shown in (a), the results of the GHD are provided in (b) to (f), the extracted upper body region is presented in (g) and the extracted template for tracking and pursuit is given in (h).

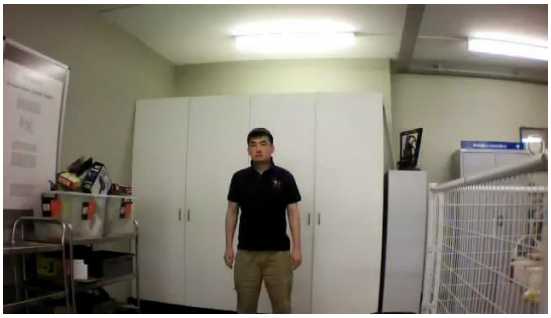

1(a)

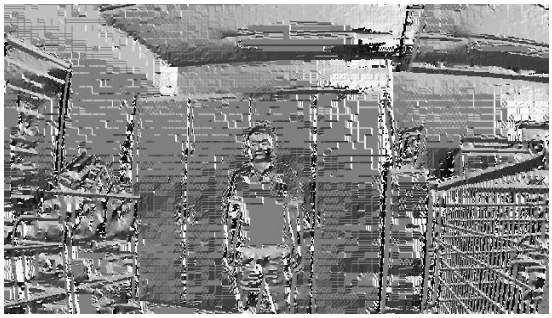

1(b)

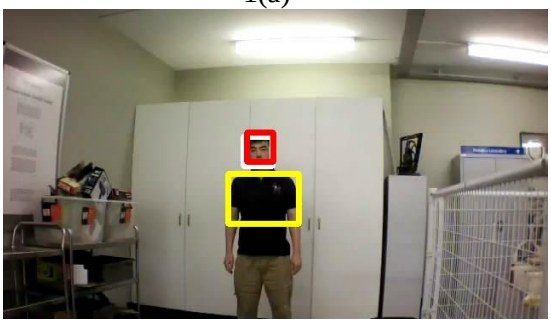

1(c)

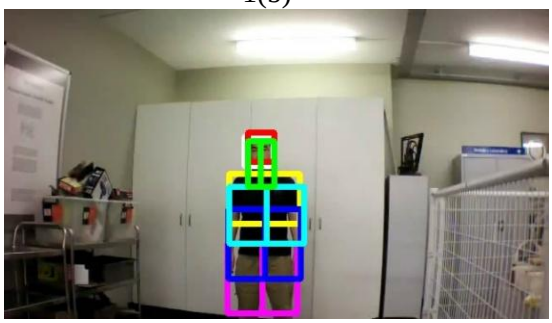

1(d)

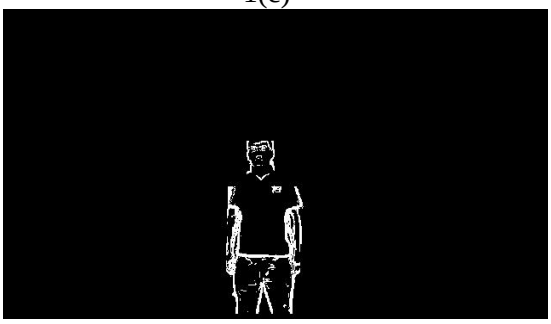

1(e)

1(f)

1(g)

1(h)

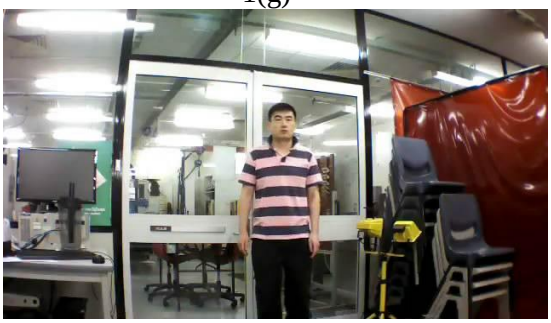

2(a)

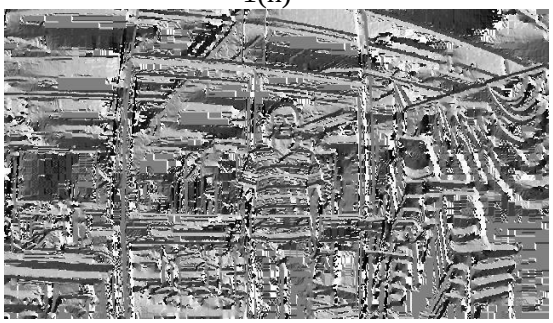

2(b)

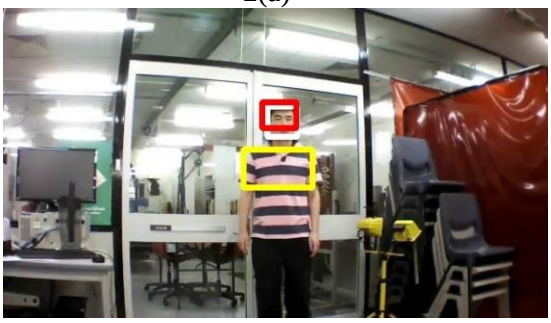

2(c)

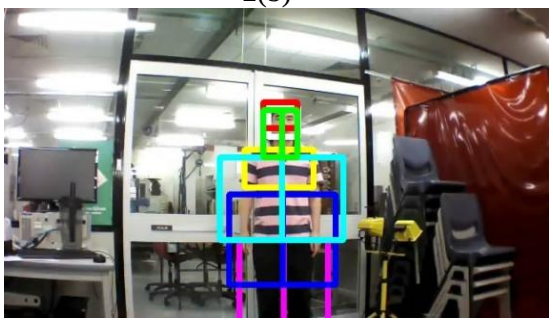

2(d)

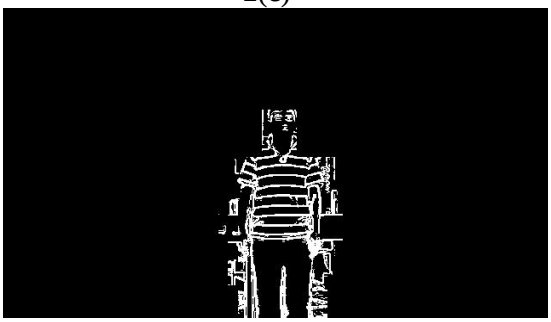

2(e)

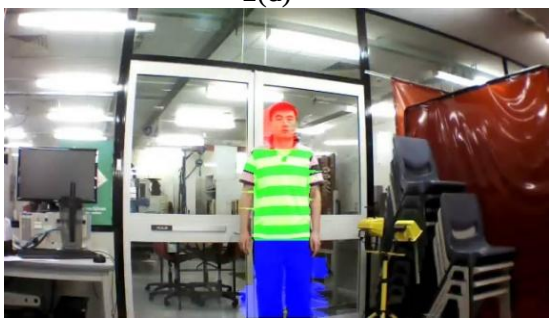

2(f)

2(g)

2(h)

(a) Original fetched image
(b) Gradient orientation map
(c) Face, head and shoulder detections
(d) Estimated body regions
(e) Unfilled body outlines
(f) Segmented body regions
(g) Extracted upper body region
(h) Extracted template

Figure 49 Human detection and template extraction

Once the template is extracted, the drone is activated by switching WIFI to connect to the drone, this is done using Network Shell (NETSH) commands, NETSH commands are typically used for network configurations. An example use to connect to the drone looks like this:

```
system("netsh wlan connect name=\"ardrone2_203074\"");
```

The connection is deemed successful if the drone starts transmitting live video feed, else the connection is retried every 30 seconds. The drone then behaves according to the autopilot mode, but the target acquisition method stays the same. This involves searching continuously in the live video feed which is done based on human detection and template matching. The proposed GHD method is used for human detection while the proposed TTT method described earlier in Section 4.2 is implemented for template matching. The target is only acquired if both methods returned true in which the human detection is employed to detect potential human looking figures, the upper body region of the figure is compared with the extracted template earlier using template matching. Simply put, the object in the image must look like a human and the upper body region of the object must match with the existing template. When successful, target is acquired by extracting the matched ROI as the starting template for tracking and pursuit. Finally, the target is tracked continuously using the TTT in which the required motions are computed and send to the drone to pursuit the target.

As the drone is capable of fully spatial movements (six output coordinates), after conducting several experiments, it is decided to simplify the motion control by only rely on three types of motions: yaw rotation, surge and heave translations, this is to ensure individual motions of the drone can be identified easily, as given in (218) to (221).

$$P_T = H_T \frac{5}{2}\left(\frac{\varphi}{3\varphi + 1}\right) \tag{218}$$

$$V_z = \frac{P_T - \min(P_z, 2P_T)}{2P_T} \tag{219}$$

$$R_\gamma = 2\left(1 - 2\frac{T_x}{w}\right)\left(\frac{1}{2} - |V_z|\right)^2 \tag{220}$$

$$V_x = \left(\frac{1}{2} - |R_\gamma|\right)^2 \tag{221}$$

where P_T and P_z are the desired and actual altitude of the drone, respectively, H_T is the estimated height of the target, φ is the golden ratio, w is the maximum image width, T_x is the horizontal centroid position of the upper body belonging to the target in the image, V_x and V_z are surge and heave translations, respectively, R_γ is yaw rotation. Note: for safety reason, during the experiment, surge and heave translations are capped at 75 and 50 centimetres per second, respectively, while yaw rotation is capped at 60 ° per second. V_x, V_z and R_γ are chained together (V_z is included in R_γ, while R_γ is included in V_x), this means that heave translation has the highest priority between the three motions, while surge translation has the lowest priority, this is to ensure the drone is flying at the desired altitude and facing the desired direction before moving forward.

5.4.1 The Standby Mode

In the standby mode, the drone simply stays hovering after it takes-off. Two example tracking and pursuit sequences are shown in Fig. 50 and Fig. 51. In the figures, the live pursuit sequences are presented in (a), while the trajectory maps are provided in (b). The motion control of V_z (heave translation), V_x (surge translation) and R_γ (yaw rotation) are displayed at the top left corner in the liver pursuit sequences, where 1 and –1 represent the positive and negative maximum velocities. The green ROI is the results of human detection using the GHD, blue and yellow ROIs are the results of tracking using the TTT. Furthermore, a demonstration video of the tracking and pursuit sequence shown in Fig. 51 can also be viewed online at: https://youtu.be/4r19bvS9K5U.

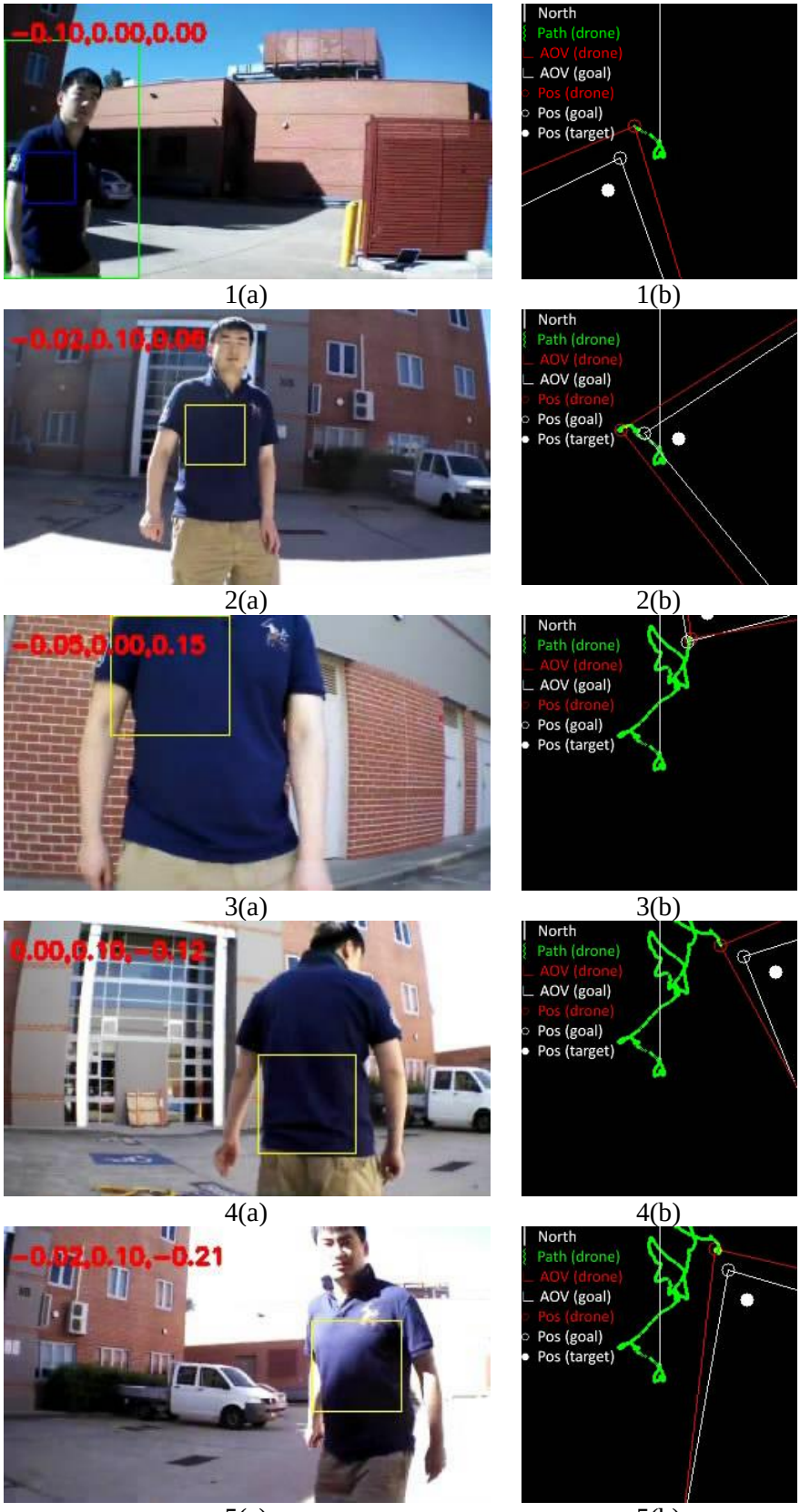

1(a) 1(b)

2(a) 2(b)

3(a) 3(b)

4(a) 4(b)

5(a) 5(b)

(a) Live pursuit sequence (b) Trajectory map

Figure 50 Target pursuit in standby mode – case 1

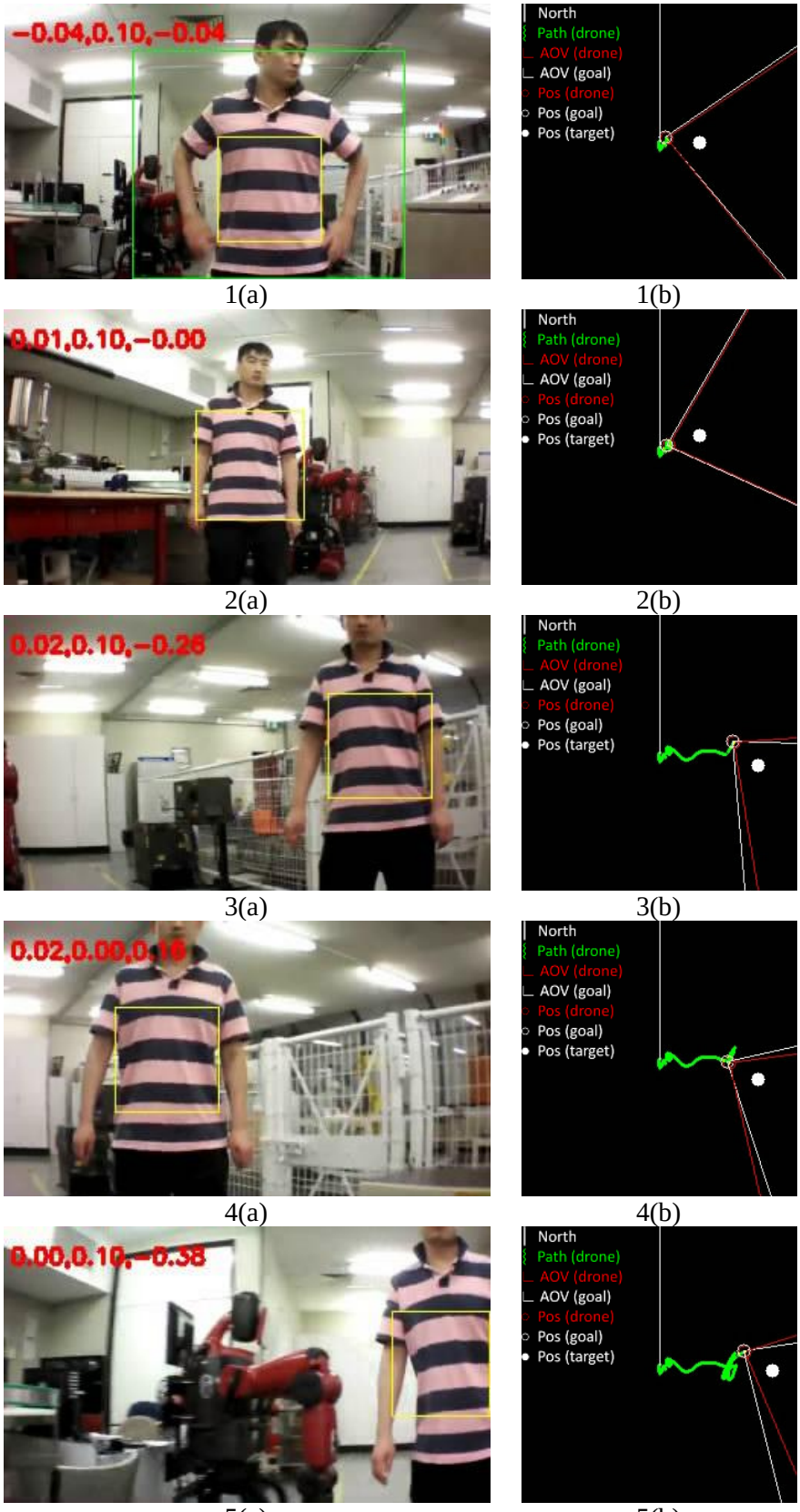

(c) Live pursuit sequence (d) Trajectory map

Figure 51 Target pursuit in standby mode – case 2

5.4.2 The Sentry Mode

In the sentry mode, the drone remains stationary and takes-off only when the required target is acquired. This allows the drone to be used as a monitoring device that can be placed at any convenient spots, as shown in Fig. 52. Since the tracking and motion control are exactly the same as in standby mode, only target acquisition is provided. In the figure, the placement of the drone is given in (a), two cases of target acquisition are presented in (b) and (c): in (b), target is not acquired since no human is detected, while in (c), target is acquired successfully as intended.

(a) Placement of the drone

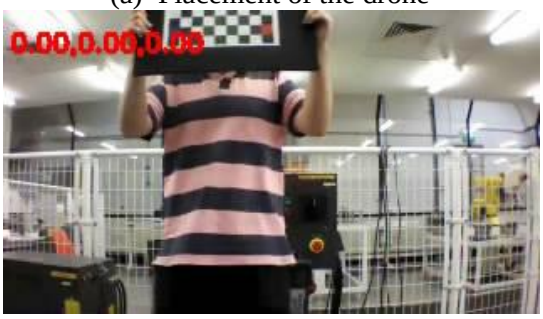

(b) Target is not acquired since no human is detected

(c) Target acquired successfully as intended

Figure 52 Target acquisition in sentry mode

5.4.3 The Search Mode

Lastly, in the search mode, the drone scans for the target while moving continuously in a fixed path. If the target is found, the drone immediately stops the patrol and engage into pursuit, on the other hand, if the target is lost (no detection within past 4 seconds), the drone moves to the nearest waypoint and continues with patrol. This is done via waypoints, the positions of the waypoints are pre-defined using the trajectory map.

In this research, a route is selected for demonstration purpose as shown in Fig. 53. In the figure, the live pursuit sequences are presented in (a), while the trajectory maps are provided in (b), the waypoints are represented by the magenta circles on the trajectory map, waypoint is counted as reached if the drone moves within the radius of the circle. Note: waypoints 5 to 7 are the same as waypoints 3 to 1, respectively. Target is acquired near waypoint 4, but lost near waypoint 5.

Based on the results of the standby, sentry and search modes, it can be seen that the autonomous tracking and pursuit system has been successfully implemented as the drone is capable of finding and following the intended target given only an input image. It is important to note that the tracking and pursuit are not limited to the clothing worn in the three modes provided earlier, to illustrate this, two more examples are provided in Fig. 54.

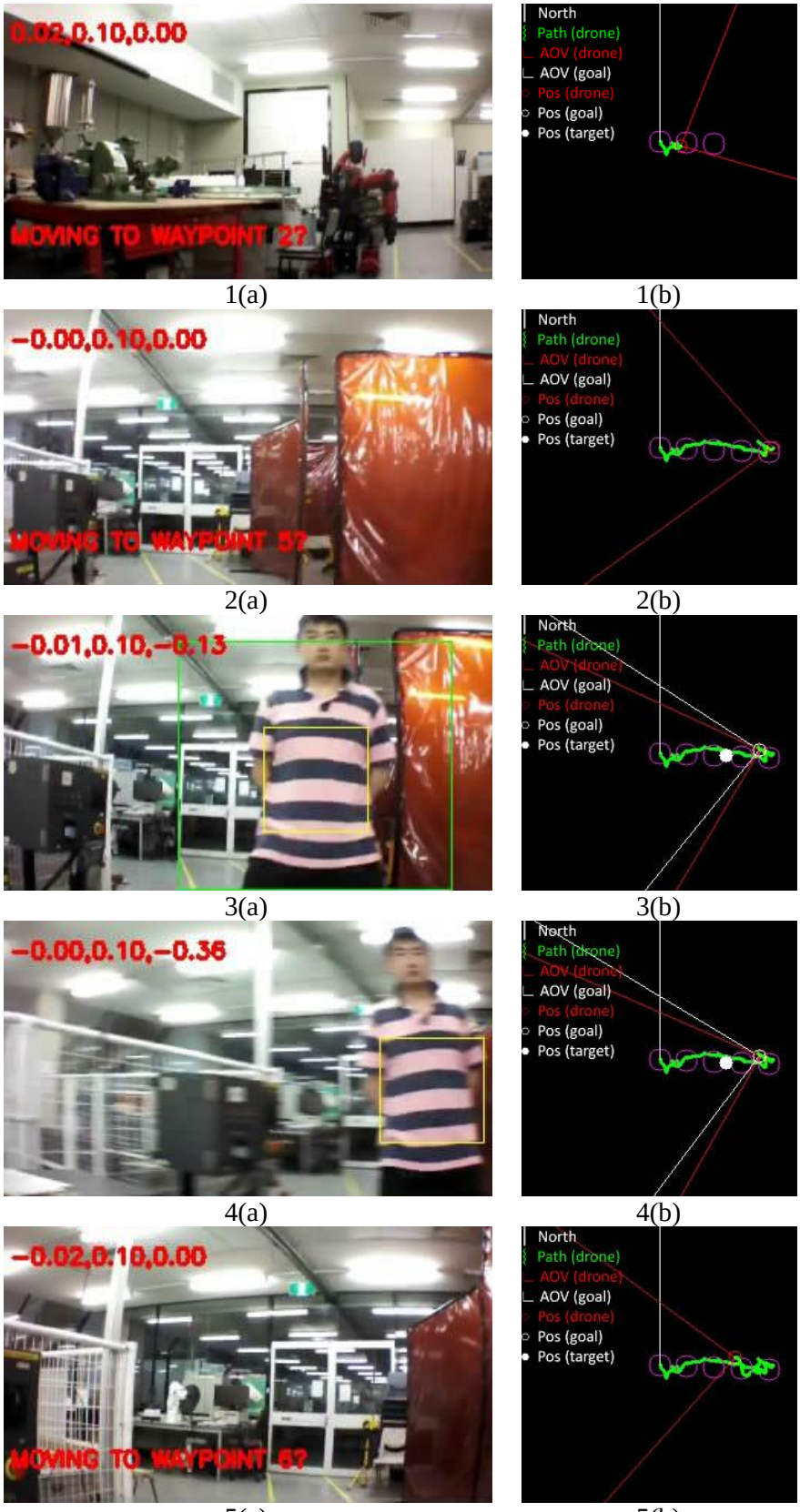

(a) Live pursuit sequence (b) Trajectory map

Figure 53 Target pursuit in search mode

1(a)

1(b)

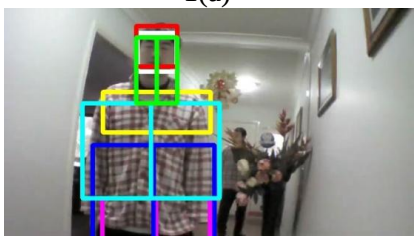

1(c)

1(d)

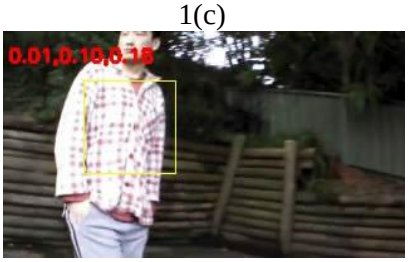

1(e)

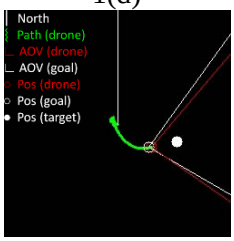

1(f)

2(a)

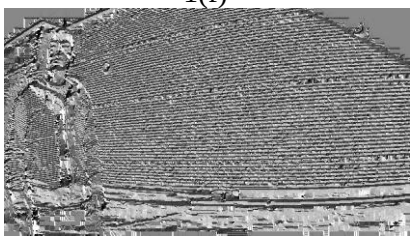

2(b)

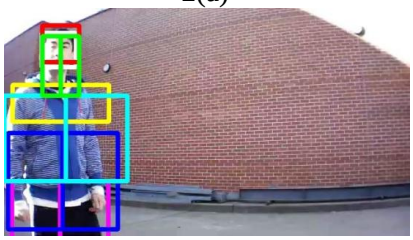

2(c)

2(d)

2(e)

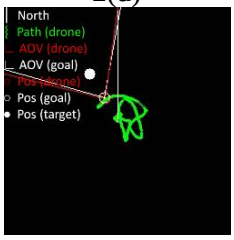

2(f)

(a) Original fetched image
(b) Gradient orientation map
(c) Estimated body regions
(d) Extracted template
(e) Live pursuit sequence
(f) Trajectory map

Figure 54 More target pursuit results

Chapter 6 Discussions and Conclusions

This chapter discusses the effectiveness of the methods proposed in this thesis and concludes the completed work. Section 6.1 examines the novelties related to colour based feature detection. Section 6.2 considers the novelties related to object detection and tracking, Section 6.3 reviews the target pursuit experiment and potential future work are provided in Section 6.4.

6.1 Colour Based Feature Detection

A novel colour enhancement method named CCE is introduced. The proposed CCE method is an efficient and simple filtering tool to boost the saliency level of the critical regions in the image by maximising the chroma while preserving the hue angle. As evidenced by the experimental results, it is much easier to identify colours with images pre-processed with CCE. It is worth mentioning that the drawback of CCE is the loss of texture detail, therefore it is not recommended for edge based detections.

A novel colour identification method named AMT is also proposed. The proposed method firstly analyses the image to determine important properties of the image. It is then followed by a colour space selection scheme in which the most suitable hue based colour space is selected based on properties obtained through image analysis. Finally, the image is filtered through the channels of the selected colour model to identify the required colour. As illustrated in the experimental results using benchmark images, this method is able to identify the colour even when the image is heavily affected by effects such as illumination and shadow. However, the colour space selection scheme employed by this approach is currently limited to hue based colour spaces.

Additionally, a novel colour model named HPB is created. The proposed HPB colour model is converted from the RGB colour model and it consists of three colour

components: hue, purity and brightness. HPB model can be represented in three different geometric shapes: sphere, hemisphere and cylinder. Compared to existing hue based colour models, HPB model allows enhanced colour detection from images, even with significantly different lighting conditions. However, the computation required to convert between the model and RGB is relatively more expensive than the traditional hue based models.

6.2 Object Detection and Tracking

A novel human detection method named GHD is introduced. The proposed GHD method works by detecting the face, head and shoulder separately, mainly using gradient maps. Compared to existing methods, the advantages of the GHD is that firstly rather than detecting the human and display the results into a rectangular ROI, the figure of the human body is detected, extracted and segmented into key parts with relatively high accuracy. Secondly, the GHD does not require any prior training about the image, as it does not rely on pre-training. However, as the proposed method is designed to extract the figure with the highest probability, currently it is only suited for single person detection.

A novel object tracking method named TTT is also proposed. The key strategies involved in the proposed TTT method are: combining intensity template matching with colour histogram model to increase tracking robustness, employing a three-tier system to store templates, applying update and tracking policies for template management. Using the benchmark videos and overlap performance evaluation, experimental results have shown that TTT produced the highest score among exiting methods. TTT is also relatively fast to support real time tracking as evidenced from the target pursuit experiment. The limitation of the TTT is perhaps the memory and computational requirements when dealing with multiple targets, as each target requires its own set of templates and these templates need to be compared against all existing ones, this means that the cost increases quadratically with increased number of targets.

6.3 Target Pursuit Using a UAV

A novel autopilot flight controller with manual override capability is introduced. The controller provides three autopilot modes: standby, sentry and search. Experimental results have shown that the autonomous tracking and pursuit system has been successfully implemented as the drone is capable of finding and following the intended target given only an input image. This is done by first implementing image fetching to automatically connect to WIFI, download the image and decode it. Then, human detection is performed to extract the template from the upper body of the person. The intended target is acquired using both human detection and template matching. Finally, target pursuit is achieved by tracking the template continuously while sending the motion commands to the drone. Only greyscale input is considered for human detection, while for template matching, both greyscale and RGB are considered for improved tracking accuracy and template management. A novel monocular vision based depth estimation method through recovering the focal length is also proposed, and by combining with the onboard sensors, the positions of the drone and the target can be mapped.

Despite satisfactory results from the experiment, there are several problems with the current system. Firstly, as the human detection and object tracking methods have consumed the vast majority of the available computational power, the colour based feature detection methods have not been implemented into the real-time tracking and pursuit system. Secondly, the drone used in this research occasionally experiences drift which causes it to wander out of the intended path, this is mostly caused by noise of the accelerometer on the drone. Thirdly, since the drone is not equipped with a GPS, sensor reading and integration errors can build up quickly, this cause the trajectory mapping to be less reliable as flight time goes on.

In summary, the majority of the existing related methods are developed using computer simulation with the assumption of ideal environmental factors, while the remaining few practical methods are mainly developed to track and follow simple objects that contain monochromatic colours with very little texture variances. Current research in this topic is lacking of practical vision based approaches. Therefore, the

work conducted in this research is intended to fill the gap by designing an autonomous system for vision based target pursuit using a UAV. Although vision based target pursuit is a complex problem, it can be concluded that the target pursuit experiment conducted in this research is successful. This can be evidenced by the live tracking and mapping of the intended targets with different clothing in both indoor and outdoor environments. Additionally, the various methods developed in this research could enhance the performance of practical vision based applications especially in detecting and tracking of objects.

6.4 Future Work

There are some interesting possibilities for future work with the various methods developed in this research.

As the proposed colour enhancement method (CCE) is designed to boost colour saliency at the cost of texture detail, a potential improvement of the method is to introduce a control parameter that influences the effect level of the enhancement.

Two possible improvements can be considered for the proposed colour identification method (AMT): training the colour space selection scheme using machine learning might produce better outcomes in certain scenarios, including more colour models into the selection pool to increase its overall performance.

Since the proposed colour model (HPB) can be represented in six different structures (three shapes: sphere, hemisphere and cylinder, each consists of two variations) and each structure has its own strength and weakness, a possible next step is to adaptively select the optimal colour structure that produces the best colour identification results based on the existing lighting condition.

Considered that the proposed human detection method (GHD) is designed to extract the figure with the highest probability in the image, multi-person detection is certainly a possibility for future work. Besides human detection, another potential

application for GHD is human recognition, as the GHD separates the human figure into head, upper body and lower body, face and clothing recognitions can be applied to identified the person.

For the proposed object tracking method (TTT), it will be intriguing to see if better results can be achieved by replacing the update and tracking policies with learning based selections. With increased computational power, tracking multiple objects is certainly another possible improvement.

Despite the limitations of the target pursuit experiment, there are several exciting ideas for future considerations. Firstly, face and person recognition could be implemented with the drone for improved tracking accuracy. Secondly, the drone could also map the surrounding areas during the pursuit, ideally with a depth sensor. Thirdly, multiple drones could work together for cooperative tasks such as tracking a group of people.

References

[1] A. Kashyap, and D. Ghose, "Pursuing a time varying and moving source signal using a sensor equipped UAV," Unmanned Aircraft Systems, Miami, USA, pp. 506–515, June 2017.

[2] R. Lima, and D. Ghost, "Target localization and pursuit by sensor-equipped UAVs using distance information," Unmanned Aircraft Systems, Miami, USA, pp. 383–392, June 2017.

[3] X. W. Fu, H. C. Feng, and X. G. Gao, "UAV mobile ground target pursuit algorithm," Intelligent and Robotic Systems, vol. 68, no. 3–4, pp. 359–371, December 2012.

[4] U. Zengin, and A. Dogan, "Cooperative target pursuit by multiple UAVs in an adversarial environment," Robotics and Autonomous Systems, vol. 59, no. 12, pp. 1049–1059, December 2011.

[5] P. Theodorakopoulos, and S. Lacroix, "UAV target tracking using an adversarial iterative prediction," Robotics and Automation, Kobe, Japan, pp. 2866–2871, May 2009.

[6] I. F. Mondragón, P. Campoy, M. A. O. Mendez, and C. Martinez, "3D object following based on visual information for unmanned aerial vehicles," Automatic Control and Industry Applications, Bogota, Colombia, October 2011.

[7] A. Basit, W. S. Qureshi, M. N. Dailey, and T. Krajník, "Joint localization of pursuit quadcopters and target using monocular cues," Intelligent and Robotic Systems, vol. 78, no. 3–4, pp. 613–630, June 2015.

[8] K. Haag, S. Dotenco, and F. Gallwitz, "Correlation filter based visual trackers for person pursuit using a low-cost quadrotor," Innovations for Community Services, Nuremberg, Germany, July 2015.

[9] J. E. G. Balderas, G. Flores, L. R. G. Carrillo, and R. Lozano, "Tracking a ground moving target with a quadrotor using switching control," Intelligent and Robotic Systems, vol. 70, no. 1–4, pp. 65–78, April 2013.

[10] C. Teuliere, L. Eck, and E. Marchand, "Chasing a moving target from a flying UAV," Intelligent Robotic and Systems, San Francisco, USA, pp. 4929–4934, September 2011.

[11] X. Zhang, Y. Li, P. Mumford, and C. Rizos, "Allan variance analysis on error characters of MEMS inertial sensors for an FPGA-based GPS/INS system," GPS/GNNS, Tokyo, Japan, pp. 127–133, November 2008.

[12] H. C. Webber, Image Processing and Transputers, Ios Pr Inc, 1992.

[13] B. Waske, and J. Benediktsson, “Pattern recognition and classification,” Encyclopedia of Remote Sensing, Springer, pp. 503–509, 2014.

[14] S. Kawada, S. Sakai, N. Akahane, K. Mizobuchi, and S. Sugawa, “A color-independent saturation, linear response, wide dynamic range CMOS image sensor with retinal rod- and cone-like color pixels,” VLSI Circuits, Kyoto, Japan, pp. 180–181, June 2009.

[15] R. Szeliski, Computer Vision: Algorithms and Applications, Springer, 2010.

[16] D. H. Ballard, and C. M. Brown, Computer Vision, Prentice Hall, 1982.

[17] S. R. E. Datondji, Y. Dupuis, P. Subirats, and P. Vasseur, “A survey of vision-based traffic monitoring of road intersections,” Intelligent Transportation Systems, vol. 17, no. 10, pp. 2681–2698, October 2016.

[18] H. Salmante, L. Khoudour, and Y. Ruichek, “A video-analysis-based railway-road safety system for detecting hazard situations at level crossings,” Intelligent Transportation Systems, vol. 16, no. 2, pp. 596–609, April 2015.

[19] M. J. Roberson, M. Bryson, A. Friedman, O. Pizarro, G. Troni, P. Ozog, and J. C. Henderson, “High-resolution underwater robotic vision-based mapping and three-dimensional reconstruction for archaeology,” Field Robotics, vol. 34, no. 4, pp. 625–643, June 2017.

[20] G. Ros, S. Ramos, M. Granados, A. Bakhtiary, D. Vazquez, and A. M. Lopez, “Vision-based offline-online perception paradigm for autonomous driving,” Applications of Computer Vision, Waikoloa, USA, pp. 231–238, January 2015.

[21] F. Schroff, D. Kalenichenko, and J. Philbin, “FaceNet: a unified embedding for face recognition and clustering,” Computer Vision and Pattern Recognition, pp. 815–823, 2015.

[22] S. S. Rautaray, and A. Agrawal, “Vision based hand gesture recognition for human computer interaction: a survey,” Artificial Intelligence Review, vol. 43, no. 1, pp. 1–54, January 2015.

[23] J. B. Shi, and C. Tomasi, “Good features to track,” Computer Vision and Pattern Recognition, Seattle, USA, pp. 593–600, June 1994.

[24] S. Jayaraman, S. Esakkirajan, and T. Veerakumar, Digital Image Processing, Tata McGraw Hill Education, 2009.

[25] P. Gaur, and S. Tiwari, “Recognition of 2D barcode images using edge detection and morphological operation,”, Computer Science and Mobile Computing, vol. 3, no. 4, pp. 1277–1282, April 2014.

[26] C. Yu, Y. H. Song, Q. Meng, Y. L. Zhang, and Y. Liu, “Text detection and recognition in natural scene with edge analysis,” Computer Vision, vol. 9, no. 4, pp. 603–613, August 2015.

[27] Q. Ding, J. H. Ji, F. Gao, and Y. T. Yang, “Machine-vision-based defect detection using circular Hough transform in laser welding,” Machinery, Materials and Computing Technology, pp. 730–733, 2016.

[28] K. J. Karande, and S. N. Talbar, Independent Component Analysis of Edge Information for Face Recognition, Springer, 2014.

[29] J. Merkow, Z. W. Tu, D. Kriegman, and A. Marsden, “Structural edge detection for cardiovascular modeling,” Medical Image Computing and Computer-Assisted Intervention, pp. 735–742, November 2015.

[30] T. Sugawara, H. Altmannshofer, and S. Kakegawa, “Applications of road edge information for advanced driver assistance systems and autonomous driving,” Advanced Microsystems for Automotive Applications, pp. 71–86, August 2017.

[31] L. G. Roberts, “Machine perception of three-dimensional solids,” Optical and Electro-Optical Information Processing, MIT Press, pp. 159–197, May 1965.

[32] J. M. S. Prewitt, “Object enhancement and extraction,” Picture Processing and Psychopictorics, New York Academic Press, pp. 75–149, 1970.

[33] I. Sobel, “Camera models and machine perception,” PhD Thesis, Stanford University, May 1970.

[34] D. Marr, and E. Hildreth, “Theory of edge detection,” Biological Sciences, vol. 207, no. 1167, pp. 187–217, February 1980.

[35] J. Canny, “A computational approach to edge detection,” Pattern Analysis and Machine Intelligence, vol. 8, no. 6, pp. 679–698, November 1986.

[36] M. P. Tran, “3D image analysis with variational methods and wavelets - applications to medical image processing,” PhD Thesis, University of Orléans, September 2012.

[37] N. K. Myshkin, H. Kong, A. Y. Grigoriev, and E. S. Yoon, “The use of color in wear debris analysis,” Wear, vol. 251, no. 1–12, pp. 1218–1226, October 2001.

[38] R. Trias-Sanz, G. Stamon , and J. Louchet, “Using colour, texture, and hierarchial segmentation for high-resolution remote sensing,” Photogrammetry and Remote Sensing, vol. 63, no. 2, pp. 156–168, March 2008.

[39] K. H. Seo, J. H. Shin, W. Kim, and J. J. Lee, “Real-time object tracking and segmentation using adaptive color snake model,” Control, Automation, and Systems, vol. 4, no. 2, pp. 236–246, April 2006.

[40] S. L. Phung, A. Bouzerdoum, and D. Chai, “Skin segmentation using color pixel classification: analysis and comparison,” Pattern Analysis and Machine Intelligence, vol. 27, no. 1, pp. 148–154, January 2005.

[41] M. N. Wu, C. C. Lin, and C. C. Chang, “Brain tumor detection using color-based k-means clustering segmentation,” Intelligent Information Hiding and Multimedia Signal Processing, Kaohsiung, Taiwan, pp. 245–250, November 2007.

[42] A. B. Hillel, R. Lerner, D. Levi, and G. Raz, “Recent progress in road and lane detection: a survey,” Machine Vision and Applications, vol. 25, no. 3, pp. 727–745, April 2014.

[43] G. Alenya, B. Dellen, and C. Torras, “3D modelling of leaves from color and ToF data for robotized plant measuring,” Robotics and Automation, Shanghai, China, pp. 3408–3414, May 2011.

[44] D. P. Tian, “A review on image feature extraction and representation techniques,” Multimedia and Ubiquitous Engineering, vol. 8, no. 4, pp. 385–396, July 2013.

[45] P. Soille, and P. Vogt, “Morphological segmentation of binary patterns,” Pattern Recognition Letters, vol. 30, no. 4, pp. 456–459, March 2009.

[46] N. Otsu, “A threshold selection method from gray-level histograms,” System, Man, and Cybernetics, vol. 9, no. 1, pp. 62–66, January 1979.

[47] S. P. Lloyd, “Least squares quantization in PCM,” Information Theory, vol. 28, no. 2, pp. 129–137, March 1982.

[48] K. Fukunaga, and L. D. Hostetler, “The estimation of the gradient of a density function, with applications in pattern recognition,” Information Theory, vol. 21, no. 1, pp. 32–40, January 1975.

[49] A. Fathi, and G. Mori, “Action recognition by learning mid-level motion,” Computer Vision and Pattern Recognition, Anchorage, USA, June 2008.

[50] S. Khalid, U. Akram, and S. Razzaq, “Behaviour recognition using multivariate m-mediod based modelling of motion trajectories,” Multimedia Systems, vol. 21, no. 5, pp. 485–505, September 2014.

[51] I. Bogun, A. Angelova, and N. Jaitly, “Object recognition from short videos for robotic perception,” arXiv: 1509.01602, September 2015.

[52] Y. Pekelny, and C. Gotsman, “Articulated object reconstruction and markerless motion capture from depth video,” Eurographics, vol. 27, no. 2, pp. 399–408, 2008.

[53] A. Sobral, and A. Vacavant, “A comprehensive review of background subtraction algorithms evaluated with synthetic and real videos,” Computer Vision and Image Understanding, vol. 122, pp. 4–21, May 2014.

[54] D. Fortun, P. Bouthemy, and C. Kervrann, “Optical flow modeling and computation: a survey,” Computer Vision and Image Understanding, vol. 134, pp. 1–21, May 2015.

[55] C. Stauffer, and W. E. L. Grimson, “Adaptive background mixture models for real-time tracking,” Computer Vision and Pattern Recognition, Ft. Collins, USA, pp. 246–252, June 1999.

[56] P. KaewTraKulPong, and R. Bowden, “An improved adaptive background mixture model for real-time tracking with shadow detection,” Advanced Video Based Surveillance Systems, London, UK, pp. 1–5, September 2001.

[57] R. Mann, and M. S. Langer, “Optical snow and the aperture problem,” Pattern Recognition, Quebec City, Canada, pp. 264–267, August 2002.

[58] B. D. Lucas, and T. Kanade, “An iterative image registration technique with an application to stereo vision,” Artificial Intelligence, Vancouver, Canada, pp.674–679, August 1981.

[59] P. A. Kumar, and B. Anuradha, “Estimating reflectivity of DWR images by analysing different colour spaces through distance measures,” Advances in Computational Sciences and Technology, vol. 10, no. 8, pp. 2191–2200, 2017.

[60] N. A. Ibraheem, M. M. Hasan, R. Z. Khan, and P. K. Mishra, “Understanding color models: a review,” Science and Technology, vol. 2, no. 3, pp. 265–275, 2012.

[61] P. Sebastian, Y. V. Voon, and R. Comley, “Colour space effect on tracking in video surveillance,” Electrical Engineering and Informatics, vol. 2, no. 4, pp. 298–312, 2010.

[62] H. D. Cheng, X. H. Jiang, Y. Sun, J. L. Wang, “Color image segmentation: advances and prospects,” Pattern Recognition, vol. 34, no. 12, pp. 2259–2281, 2001.

[63] P. Sebastian, Y. V. Voon, and R. Comley, “The effect of colour space on tracking robustness,” Industrial Electronics and Applications, Singapore, pp. 2512–2516, June 2008.

[64] N. M. Kwok, Q. P. Ha, and G. Fang, “Effect of color space on color image segmentation,” Image and Signal Processing, Tianjin, China, October 2009.

[65] K. N. Plataniotis, and A. N. Konstantinos, Color Image Processing and Applications, Springer, 2000.

[66] A. Ford, and A. Roberts, Colour Space Conversions, Westminster University, London, August 1998.

[67] N. Y. Hammerla, S. Halloran, and T. Ploetz, “Deep, convolutional, and recurrent models for human activity recognition using wearables,” arXiv: 1604.08880, April 2016.

[68] B. Zhou, A. Lapedriza, J. Xiao, A. Torralba, and A. Oliva, “Learning deep features for scene recognition using places database,” Advances in Neural Information Processing Systems, pp. 487–495, 2014.

[69] A. Esteva, B. Kuprel, R. A. Novoa, J. Ko, S. M. Swetter, H. M. Blau, and S. Thrun, “Dermatologist-level classification of skin cancer with deep neural networks,” Nature, vol. 542, pp. 115–118, February 2017.

[70] A. L. Buczak, and E. Guven, “A survey of data mining and machine learning methods for cyber security intrusion detection,” Communications Surveys and Tutorials, vol. 18, no. 2, 2016.

[71] R. D. Findling, and R. Mayrhofer, “Towards face unlock: on the difficulty of reliably detecting faces on mobile phones,” Advances in Mobile Computing and Multimedia, Bali, Indonesia, pp. 275–280, December 2012.

[72] S. Landset, T. M. Khoshgoftaar, A. N. Richter, and T. Hasanin, “A survey of open source tools for machine learning with big data in the Hadoop ecosystem,” Big Data, vol. 2, no. 24, December 2015.

[73] A. L. Samuel, “Some studies in machine learning using the game of checkers,” Research and Development, vol. 3, no. 3, pp. 210–229, July 1959.

[74] C. Cortes, and V. Vapnik, “Support-vector networks,” Machine Learning, vol. 20, no. 3, pp. 273–297, September 1995.

[75] F. Rosenblatt, “The perceptron: a probabilistic model for information storage and organization in the brain,” Psychological Review, vol. 65, no. 6, pp. 386–408, November 1958.

[76] Y. LeCun, P. Haffner, L. Bottou, and Y. Bengio, “Object recognition with gradient-based learning,” Shape, Contour and Grouping in Computing Vision, Springer, pp. 319–345, 1999.

[77] M. Paul, S. M. Haque, and S. Chakraborty, “Human detection in surveillance videos and its applications – a review,” Advances in Signal Processing, vol. 2013, no. 176, November 2013.

[78] A. Bialkowski, S. Denman, S. Sridharan, and C. Fookes, “A database for person re-identification in multi-camera surveillance networks,” Digital Image Computing Techniques and Applications, Fremantle, Australia, December 2012.

[79] F. Su, G. Fang, and N. M. Kwok, “Adaptive colour feature identification in image for object tracking,” Mathematical Problems in Engineering, vol. 2012, November 2012.

[80] Y. L. Hou, and G. K. H. Pang, “People counting and human detection in a challenging situation,” Systems, Man and Cybernetics, vol. 41, no. 1, pp. 24–33, Jan 2011.

[81] N. Dalal, and B. Triggs, “Histograms of oriented gradients for human detection,” Computer Vision and Pattern Recognition, San Diego, USA, pp.886–893, June 2005.

[82] M. Andriluka, S. Roth, and B. Schiele, “Pictorial structures revisited: people detection and articulated pose estimation,” Computer Vision and Pattern Recognition, Miami, USA, pp.1014–1021, June 2009.

[83] N. Dalal, “Finding People in Images and Videos,” PhD Thesis, Grenoble Institute of Technology, July 2006.

[84] W. R. Schwartz, A. Kembhavi, D. Harwood, and L. S. Davis, “Human detection using partial least squares analysis,” Computer Vision, Kyoto, Japan, pp. 24–31, September 2009.

[85] H. World, “Partial least squares,” Encyclopedia of Statistical Sciences, Wiley, vol. 6, pp. 581–591, 1985.

[86] M. Li, Z. X. Zhang, K. Q. Huang, and T. N. Tan, “Rapid and robust human detection and tracking based on omega-shape features,” Image Processing, Cairo, Egypt, pp. 2545–2548, November 2009.

[87] P. Viola, and M. Jones, “Rapid object detection using a boosted cascade of simple features,” Computer Vision and Pattern Recognition, Kauai, USA, pp. 511–518, December 2001.

[88] B. Ammar, N. Rokbani, and A. M. Alimi, “Learning system for standing human detection,” Computer Science and Automation Engineering, Shanghai, China, pp. 300–304, June 2011.

[89] D. G. Lowe, “Distinctive image features from scale-invariant interest points,” Computer Vision, vol. 60, no. 2, pp. 91–110, November 2004.

[90] J. Redmon, S. Divvala, R. Girshick, and A. Farhadi, “You Only Look Once: Unified, Real-Time Object Detection,” Computer Vision and Pattern Recognition, Las Vegas, USA, pp. 779–788, Jun 2016.

[91] F. Su, and G. Fang, “Moving object tracking using an adaptive colour filter,” Control Automation Robotics & Vision, Guangzhou, China, pp. 1048–1052, December 2012.

[92] M. Keck, L. Galup, and C. Stauffer, “Real-time tracking of low-resolution vehicles for wide-area persistent surveillance,” Applications of Computer Vision, Tampa, USA, pp. 441–448, January 2013.

[93] D. Moratuwage, B. N. Vo, and D. W. Wang, “Collaborative multi-vehicle SLAM with moving object tracking,” Robotics and Automation, Karlsruhe, Germany, pp. 5702–5708, May 2013.

[94] I. Smal, K. Draegestein, N. Galjart, W. Niessen, and E. Meijering, “Particle filtering for multiple object tracking in dynamic fluorescence microscopy images: Application to microtubule growth analysis,” Medical Imaging, vol. 27, no. 6, pp. 789–804, June 2008.

[95] F. Šuligoj, B. Šekoranja, M. Švaco, and B. Jerbić, “Object tracking with a multiagent robot system and a stereo vision camera,” Procedia Engineering, vol. 69, pp. 968–973, 2014.

[96] O. P. Popoola, and K. J. Wang, “Video-based abnormal human behavior recognition—A review,” Systems, Man, and Cybernetics, Part C (Applications and Reviews), vol. 42, no. 6, pp. 865–878, November 2012.

[97] Z. Kalal, K. Mikolajczyk, and J. Matas, “Tracking-learning-detection,” Pattern Analysis and Machine Intelligence, vol. 34, no. 7, pp. 1409–1422, July 2012.

[98] H. Grabner, M. Grabner, and H. Bischof, “Real-time tracking via on-line boosting,” British Machine Vision Conference, vol. 1, pp. 47–56, 2006.

[99] B. Y. Liu, J. Z. Huang, L. Yang, and C. Kulikowski, “Robust visual tracking using local sparse appearance model and k-selection,” Pattern Analysis and Machine Intelligence, vol. 35, no. 12, pp. 2968–2981, December 2013.

[100] D. Comaniciu, V. Ramesh, and P. Meer, “Kernel-based object tracking,” Pattern Analysis and Machine Intelligence, vol. 25, no. 5, pp. 564–577, May 2003.

[101] A. Adam, E. Rivlin, and I. Shimshoni, “Robust fragments-based tracking using the integral histogram,” Computer vision and Pattern Recognition, New York, USA, pp. 798–805, June 2006.

[102] S. F. He, Q. X. Yang, R. W. H. Lau, J. Wang, and M. H. Yang, “Visual tracking via locality sensitive histograms,” Computer Vision and Pattern Recognition, pp. 2427–2434, 2013.

[103] W. R. Dufrene, “AI techniques in uninhabited aerial vehicle flight,” Aerospace and Electronic Systems Magazine, vol.19, no.8, pp.8–12, August 2004.

[104] A. V. Gheorghe, “Unmanned aerial systems integration to national airspace system,” Infrastructure Systems and Services, Malahide, Ireland, pp.1–5, November 2008.

[105] H. Eisenbeiss, “A mini unmanned aerial vehicle (UAV): system overview and image acquisition,” Processing and Visualization Using High Resolution Imagery, Phitsanulok, Thailand, vol. 36, no. 5, pp.1–7, November 2004.

[106] G. R. Bradski, “Computer vision face tracking for use in a perceptual user interface,” Intel Technology Journal, vol. 2, pp.214–219, January 1998.

[107] R. E. Kalman, “A new approach to linear filtering and prediction problems,” Basic Engineering, vol. 82, no. 1, pp.35–45, March 1960.

[108] P. D. Moral, “Nonlinear filtering: interacting particle resolution,” Markov Processes and Related Fields, vol. 2, no. 4, pp.555–580, October 1996.

[109] P. Pounds, R. Mahony, and P. Corke, “Modelling and control of a quad-rotor robot,” Australasian Conference on Robotics and Automation, Auckland, New Zealand, pp.1–10, December 2006.

[110] J. C. Raimundes, and A. F. Villaverde, “Adaptive tracking control for a quad-rotor,” Nonlinear Dynamics, Saint Petersburg, Russia, June 2008.

[111] F. Su, and G. Fang, “Chroma based colour enhancement for improved colour segmentation,” Sensing Technology, Auckland, New Zealand, pp. 162–167, December 2015.

[112] F. Su, and G. Fang, “Colour identification using an adaptive colour model,” Automation, Robotics and Applications, Queenstown, New Zealand, pp. 466–471, February 2015.

[113] F. Su, G. Fang, and J. J. Zou, “A novel colour model for colour detection,” Modern Optics, vol. 64, no. 8, pp. 819–829, 2017.

[114] N. M. Kwok, G. Fang, and Q. P. Ha, “Intensity-based gain adaptive unsharp masking for image contrast enhancement,” Image and Signal Processing, Chongqin, China, pp. 529–533, October 2012.

[115] A. W. M. Smeulders, D. M. Chu, R. Cucchiara, S. Calderara, A. Dehghan, and M. Shah, “Visual tracking: an experimental survey,” Pattern Analysis and Machine Intelligence, vol. 36, no. 7, pp. 1442–1468, July 2014.

[116] F. Su, and G. Fang, “Human detection using gradient maps and golden ratio,” Automation and Robotics in Construction, vol. 31, 2014.

[117] F. Su, G. Fang, and J. J. Zou, “Human detection using a combination of face, head and shoulder detectors,” IEEE Region 10 (TENCON), Singapore, pp. 842–845, November 2016.

[118] F. Su, G. Fang, and J. J. Zou, “Robust real-time object tracking using tiered templates,” World Congress on Intelligent Control and Automation, Changsha, China, July 2018 (accepted).

[119] M. Spira, “On the golden ratio,” Mathematical Education, Seoul, Korea, pp. 1–16, July 2012.

[120] R. Lienhart, A. Kuranov, and V. Pisarevsky, “Empirical analysis of detection cascades of boosted classifiers for rapid object detection,” Pattern Recognition, vol. 2781, pp. 297–304, May 2002.

[121] J. P. Lewis, “Fast normalized cross-correlation,” Vision Interface, vol. 10, pp. 120–123, 1995.

[122] M. J. Swain, and D. H. Ballard, “Indexing via color histograms,” Active Perception and Robot Vision, pp. 261–273, Springer, Berlin, Heidelberg, 1992.

[123] W. Bouachir, and G. A. Bilodeau, “Structure-aware keypoint tracking for partial occlusion handling,” Applications of Computer Vision, Steamboat Springs, USA, pp. 877–884, March 2014.

[124] B. Babenko, M. H. Yang, and S. Belongie, “Robust object tracking with online multiple instance learning,” Pattern Analysis and Machine Intelligence, vol. 33, no. 8, pp. 1619–1632, August 2011.

[125] Y. Wu, J. W. Lim, and M. H. Yang, “Object tracking benchmark,” Pattern Analysis and Machine Intelligence, vol. 37, no. 9, pp. 1834–1848, September 2015.

[126] M. Everingham, L. V. Gool, C. K. I. Williams, J. Winn, and A. Zisserman, “The pascal visual object classes (VOC) challenge,” Computer Vision, vol. 88, no. 2, pp. 303–338, June 2010.

[127] J. Smit, R. Kleihorst, A. Abbo, J. Meuleman, and G. V. Willigenburg, “Real time depth mapping performed on an autonomous stereo vision module,” Integrated Systems and Circuits, Veldhoven, Netherlands, pp. 306–310, November 2004.

[128] N. Lazaros, G. C. Sirakoulis, and A. Gasteratos, “Review of stereo vision algorithms: from software to hardware,” Optomechatronics, vol. 2, no. 4, pp. 435–462, November 2008.

[129] Z. Zhang, “A flexible new technique for camera calibration,” Pattern Analysis and Machine Intelligence, vol. 22, no. 11, pp. 1330–1334, November 2000.

[130] Q. Z. Wang, and X. Y Cheng, “The simple camera calibration approach based on a triangle and depth estimation from monocular vision,” Intelligent Robots and Systems, St. Louis, USA, pp. 316–320, October 2009.